

**Defect induced room temperature ferromagnetism
in non magnetic semiconducting oxides**

By

HOMNATH LUITEL

(Enrollment No: PHYS04201404011)

VARIABLE ENERGY CYCLOTRON CENTRE

Kolkata-700064, India

A thesis submitted to the

Board of Studies in Physical Sciences

In partial fulfillment of requirements

for the Degree of

DOCTOR OF PHILOSOPHY

of

HOMI BHABHA NATIONAL INSTITUTE



October, 2018

Homi Bhabha National Institute¹

Recommendations of the Viva Voce Committee

As members of the Viva Voce Committee, we certify that we have read the dissertation prepared by Homnath Luitel entitled Defect induced room temperature ferromagnetism in non magnetic semiconducting oxides and recommend that it may be accepted as fulfilling the thesis requirement for the award of Degree of Doctor of Philosophy.

Chairman - Prof. Vaishali Naik

Vaishali Naik

Date: 15/3/2019

Guide / Convener - Prof. Dirtha Sanyal

Dirtha Sanyal

Date: 15/03/2019

Co-guide - <Name> (if any)

Date:

Examiner - Prof. Kalobaran Maiti

Kalobaran Maiti

Date: 26/03/2019

Member 1- Prof. Pallab Banerji

P. Banerji

Date: 15-03-2019

Member 2- Prof. Pintu Sen

Pintu Sen

Date: 15-03-2019

Final approval and acceptance of this thesis is contingent upon the candidate's submission of the final copies of the thesis to HBNI.

I hereby certify that I have read this thesis prepared under my direction and recommend that it may be accepted as fulfilling the thesis requirement.

Date: 15/03/2019

Place: KOLKATA

Dirtha Sanyal

<Signature>

Guide

¹ This page is to be included only for final submission after successful completion of viva voce.

STATEMENT BY AUTHOR

This dissertation has been submitted in partial fulfillment of requirements for an advanced degree at Homi Bhabha National Institute (HBNI) and is deposited in the Library to be made available to borrowers under rules of the HBNI.

Brief quotations from this dissertation are allowable without special permission, provided that accurate acknowledgement of source is made. Requests for permission for extended quotation from or reproduction of this manuscript in whole or in part may be granted by the Competent Authority of HBNI when in his or her judgment the proposed use of the material is in the interests of scholarship. In all other instances, however, permission must be obtained from the author.

Homnath Luitel.
Homnath Luitel

DECLARATION

I, hereby declare that the investigation presented in the thesis has been carried out by me. The work is original and has not been submitted earlier as a whole or in part for a degree / diploma at this or any other Institution / University.

Homnath Luitel.
Homnath Luitel

List of Publications arising from the thesis

Journal

1. *Positron annihilation lifetime characterization of oxygen ion irradiated rutile TiO₂.*
H. Luitel, A. Sarkar, M. Chakrabarti, S. Chattopadhyay, K. Asokan and D. Sanyal, *Nuclear Instruments and Methods B*, **2016**, 379, 215-218.
2. *Ab-initio calculation of magnetic properties in B, Al, C, Si, N, P and As doped rutile TiO₂.*
H. Luitel and D. Sanyal, *Int. J. Mod. Phys. B*, **2017**, 31, 1750227.
3. *Defect generation and recovery in polycrystalline ZnO during annealing below 300°C as studied by in situ positron annihilation spectroscopy.*
H. Luitel, D. Sanyal, N. Gogurla, A. Sarkar, *J. Mat. Sci.*, **2017**, 52, 7615.
4. *Ferromagnetism in P and As doped SnO₂: First-principle study.*
H. Luitel, S. Roy, D. Sanyal, *Computational Condensed Matter*, **2017**, 14, 36-39.
5. *Positron annihilation spectroscopic characterization of defects in wide band gap oxide Semiconductors.*
A. Sarkar, **H. Luitel**, N. Gogurla and D. Sanyal, *Mat. Res. Exp.*, **2017**, 4, 035909.
6. *Ab-initio calculation and experimental observation of room temperature ferromagnetism in 50 keV nitrogen implanted rutile TiO₂.*
H. Luitel, M. Chakrabarti, A. Sarkar, S. Dechoudury, D. Bhowmick, V. Naik and D. Sanyal, *Mat. Res. Exp.*, **2018**, 5, 026104.

7. *Experimental and first principle study of room temperature ferromagnetism in 1.2 MeV C⁴⁺ implanted rutile TiO₂.*
H. Luitel, P. Chettri, A. Tiwari and D. Sanyal, *Mat. Res. Bulletin*, **2019**, 110, 13-17.
8. *Ferromagnetism in p-block elements doped ZnO: An ab-initio approach.*
H. Luitel and D. Sanyal, *Computational Condensed Matter*, **2019**, 19, e00376.
9. Experimental and first principle study of room temperature ferromagnetism in boron doped rutile TiO₂, **H. Luitel et al.**, (to be communicated).

Conference/Symposium

1. Defect induced ferromagnetism in non-magnetic semiconducting oxides
H. Luitel and D Sanyal, Oral presentation in *Materials Physics 2018, London, UK (2018)*.
2. Defect induced room temperature ferromagnetism in semiconducting oxides.
H. Luitel and D Sanyal, Oral presentation in *HBNI's RSM-2018, IGCAR, Tamil Nadu, India (2018) (Best Research Contribution Award)*.
3. Room temperature ferromagnetism in p-block elements doped ZnO.
H. Luitel and D. Sanyal, Oral presentation in *CMDAYS-17, Tezpur University, Assam, India (2017)*.
4. Ferromagnetism in P and As doped SnO₂.
H. Luitel, S. Roy and D. Sanyal, Poster presentation in *DAE-SSSPs 2017, BARC, India (2017)*.
5. Room temperature ferromagnetism in nitrogen doped rutile TiO₂.
H. Luitel and D. Sanyal, Poster presentation in *IBMAC-2016, New Delhi, India (2016)*.

6. Room temperature ferromagnetism in doped TiO_2 – A density functional theoretical study.

H. Luitel and D. Sanyal, Poster presentation in *ICFM- 2016, IIT-Kharagpur, India (2016)*.

7. Positron annihilation lifetime characterization of oxygen ion irradiated rutile TiO_2 .

H. Luitel, A. Sarkar, M. Chakrabarti, S. Chattopadhyay, K. Asokan and D. Sanyal, Poster presentation in *REI-18, Jaipur, India (2015)*.

Other Publications

1. *Origin of ferromagnetism in Cu doped rutile TiO_2 - An ab-initio approach.*

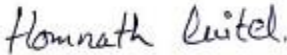
S. Roy, **H. Luitel** and D. Sanyal, *Computational Condensed Matter*, **13** (2017) 127-130.

2. First principle analysis for magnetic properties of noble metal-doped rutile TiO_2 .

S. Roy, **H. Luitel** and D. Sanyal, *Computational Condensed Matter*, **18** (2019) e00349.

3. *Defect induced room temperature ferromagnetism in methylammonium lead iodide perovskite.*

S. Sil, **H. Luitel**, M. Chakrabarty, P. P. Ray, J. Dhar, B. Bandyopadhyay and D. Sanyal, (2018) [arXiv:1809.07957](https://arxiv.org/abs/1809.07957) [cond-mat.mtrl-sci].


Homnath Luitel

Dedicated

to

My Parents

(Mrs. Bishnumaya Luitel & Mr. Mahananda Luitel)

and

My Cute Nieces

(Rashmi, Anvi and Kashvi)

ACKNOWLEDGEMENTS

First of all, I would like to express my deep and sincere gratitude to my PhD supervisor, Dr. Dirtha Sanyal for his continuous support, motivation and guidance throughout my PhD research tenure. He was always there to improve my understanding of the subject and also suggesting way out of the problems. His inspiration, understanding, faith and encouragement have kept me going throughout the tenure. I would be eternally indebted for his motivation, timely advice, insightful discussions and suggestions which made me capable to handle all problems and became a better human in life.

I am also thankful to all our collaborators (Dr. A. Sarkar, Dr. M. Chakrabarti, Dr. S. Chattopadhyay, Dr. K. Asokan, Dr. S. Dechoudhury, Dr. D. Bhowmick, Dr. V. Naik, Dr. N. Gogurla, Dr. A. Tiwari, Mr. P. Chettri & Mrs. S. Roy) for their support during research work and helpful discussion. I want to acknowledge IUAC, beam facility for providing oxygen ion beam and all RIBFG personals specially, Mr. L. Kumar for helping me with irradiation experiments at VECC, RIB facility.

I want to thank Dr. Jan-e Alam (Dean Physical Science, VECC) for his constant support, whenever required. I also want to thank all my teachers who taught me in course work and helped me to understand basic physics in lucid way. In addition, I want to thank my teachers from Sikkim University (Dr. A. Bhattacharyya & Dr. Ajay Tripathy) and also my colleges and school teachers, who still encourage and give blessing to me to do well in life.

I am thankful to HBNI for providing research fellowship and also its student travel support to attend CMMP-2018 conference held at London, UK. I want to express my thanks to all members of my doctoral committee for their valuable comments and

suggestions. Special thanks to Prof. Pallab Banerji, who has to take the trouble to come VECC for several times from IIT Kharagpur in spite of his busy schedule.

I am lucky to get a friend like Ajit Kumar, who stood by my side during the ups and downs and with whom I enjoyed my life in different and cheerful ways. I am also fortunate to have some seniors who were more like brothers and good friends, Anukul dada, Ashif dada and Sushant dada who not only gave me love and care but they were also part of all my joy and sorrow.

Special thank goes to all my batch mates and very good friends (Samrangy, Safikul, Nachiketa, Ranabir, Dipak, Shabnam and Ashik), junior colleagues (Santanu, Sudipta, Shreyasi, Mitali, Pallavi, Sumit, Sanchari, Soumen and many others), wonderful and helpful seniors (Pingal dada, Partha dada, Arghya dada and many others) for making my time wonderful at VECC. Many other persons (Santu dada, Arindam dada, Noor dada, Ayan dada) who made my life joyful and playful be it playing TT in the evening or interaction at cafeteria during weekends, it was a wonderful experience to be here at VECC. Special thanks to Dr. Amit Jana for fruitful discussions in the lab about basic physics and making me aware of many scientific programs running in India. I am also thankful to Kanak dada, Anjan dada, Abhishek dada and Dipanta dada for their helping attitude and the entire canteen staffs who perform their duties without fail, so that we can get food on time.

Lastly, I want to thank all my family members, relatives and well wishers, without whose support I would not have completed my PhD journey.


Homnath Luitel

Synopsis

Room temperature ferromagnetism in semiconductors is among one of the most fascinating topics of research in the present era. For fundamental scientists, it brings a new concept of ‘d⁰ ferromagnetism’ in a material [1, 2]. From the technological point of view, magnetic semiconductors are considered as promising candidates for spintronics application [3]. The efficient transport of spin polarized electrons is a challenge in spintronics due to the large impedance mismatch between ferromagnet-semiconductor junctions. Additional magnetic properties in semiconductors along with the semiconducting properties at room temperature will ensure the transport of spin polarized electrons efficiently and it can be used in the making new spintronics devices [4].

Search for ferromagnetic semiconductor gained pace after a report on *Science* (2000), where Dietl *et al.*, [5] theoretically predicted that the values of Curie temperature is well above room temperature in 5 at. % Mn doped ZnO and GaN. Soon, the experimental report appeared in *Nature Materials* in the year 2003; where Sharma *et al.*, [6] observed room temperature ferromagnetism in 2 at. % Mn doped ZnO. Since then, several experimental observations were recorded for room temperature ferromagnetism in various transition elements doped semiconductors. But, a different concept came into existence with the discovery of ferromagnetism in thin films of HfO₂ by Venkatesan *et al.*, [3] in 2004 and nano-crystalline oxides semiconductors by Sundaresan *et al.*, [7] in 2006. The source of magnetism was proposed to be the atomic vacancies formed in the nanocrystalline oxide systems, which leads to magnetic semiconductors without any magnetic ion doped in the

system. In the year 2007, room temperature ferromagnetism was found in nanocrystalline ZnO. The source of magnetism has been traced to the presence of the atomic vacancies in ZnO sample [8]. Since then, several reports suggested that ferromagnetism can be induced in different wide-band gap semiconductors by incorporating defects (either non magnetic impurities or the atomic vacancies) in the crystals [9-11].

In the present work, extensive theoretical calculations have been carried out using the framework of density functional theory. The magnetic property of various semiconducting oxides (Viz., TiO₂, ZnO and SnO₂) has been studied by introducing non- magnetic defects into the system. Various p-block elements have been doped at O-site and magnetic moment has been calculated after the structure optimization. The formations of defects are very common in crystal. The effect of atomic vacancies has been considered explicitly along with the doping of non-magnetic cases in some system. Experimental investigations have been carried out based on the theoretical predictions. Doping of various ions is done by Ion beam irradiations which also create atomic vacancies in the sample. The defects formation in the irradiated sample has been characterized by positron annihilation spectroscopy (PAS) and photoluminescence (PL) spectroscopy. The magnetic characterizations have been carried out using SQUID magnetometer.

This thesis has been divided into six chapters. Chapter 1 is introduction to the subject which includes literature survey relevant to the development of the field, motivation and objective of the present work. Computational methodologies and experimental techniques used in the study have been discussed in chapter 2. The next three chapters are dedicated for the primary research work done in the thesis. In

chapter 3, research works related to room temperature ferromagnetism in rutile-TiO₂ have been reported in four different sections. A detailed literature survey has been discussed in introduction section. It is followed by computational methodology, experimental details, results, discussion and conclusion. The theoretical calculations under density functional theory predict that a significant amount of magnetic moment gets generated in the TiO₂ matrix by doping different p-block elements. The primary source of magnetism is the p-orbital electrons of dopant atom when placed at the oxygen site. However, when doped at Ti-site, these elements do not produce any magnetic moment in the system. The spin-spin interactions study reveals that only B, C, N and P atom doped systems get ferromagnetic coupling between the net-spins of two dopant atoms present at O-site. The creation of both V_{Ti} and V_O produce a significant amount of magnetic moment in the system. The magnetic moment generated by the creation of vacancies gets added up with that produced from the external dopant in the system. The theoretical predictions are verified with the experimental results. Highly energetic 96 MeV oxygen ions beam have been irradiated on TiO₂ sample to create sufficient atomic-vacancies. The PAS investigation suggests a large number of Ti-vacancies have been generated in the irradiated sample. A strong ferromagnetism has been experimentally observed for TiO₂ sample containing Ti-vacancy and also for C-doped, N-doped and B-doped rutile TiO₂ samples.

In chapter 4, *Ab-initio* calculations under density functional theory predict that a significant amount of magnetic moment gets generated into the ZnO by doping various p-block elements. The primary sources of magnetism are the p-orbital electrons of dopant atom. Small contribution also comes from the neighboring O-atoms present around the dopant. The spin-spin interaction study reveals that B, C, N,

Si, P, Ge and As atom doped system have lower ground state free energy for ferromagnetic ordered system over anti-ferromagnetic system. The theoretical predictions are found in harmony with experimental observations for boron ions irradiated/implanted ZnO system.

The formation of defects has been studied explicitly in ZnO samples at various temperature by employing both in-situ and ex-situ positron annihilation technique. Annealing effect of high purity granular ZnO up to 286 °C has been studied by in situ Doppler broadening of electron positron annihilated γ -ray line shape measurement. Increase of *S*-parameter has been observed during annealing at 182 °C and 286 °C which saturates in a time scale of ~ 90 minutes. The increase of *S*-parameter during 182 °C annealing is related with removal of carbon and loosely bound hydroxyl groups from ZnO and thereby increasing open volume defects. During 286 °C annealing, such open volumes agglomerate and migrate to grain surface regions causing further increase of open volumes at the positron annihilation site. Ex-situ photoluminescence (PL) measurement have been carried out with samples annealed at 182 °C and 286 °C. Room temperature PL results are consistent with positron annihilation spectroscopic findings. Additionally, 10 K PL spectrum shows large increase of 3.311 eV emission in 286 °C annealed sample. This particular emission is related with typical crystal defects in ZnO which is a matter of discussion till date. The present study provides understanding on the interplay of defects in relatively low temperature annealed ZnO. It is important from theoretical perspective as well as for improving the performance of ZnO as an application in photocatalytic and gas sensing agent (gas sensor). It has also been observed that due to annealing temperature difference of 125 °C (from 325 °C to 450 °C), huge change occurs in low temperature

photoluminescence (PL) of ZnO. Significant reduction of free to bound (FB) transition ~ 3.315 eV is observed by increasing the annealing temperature. It has been conjectured that ~ 3.315 eV PL in ZnO is related to particular decoration (unknown) of both Zn and O vacancies.

In chapter 5, magnetic properties of SnO₂ has been theoretically studied by systematically doping various p-block elements (viz., B, C, N, Al, Si, P, S, Ga, Ge, As) at oxygen site. Density functional theory has been applied to calculate the spin polarized density of states and magnetic moment in all the systems. A significant amount of magnetic moment has been found in B, N, P and As doped SnO₂ systems. The p-orbital electrons in the valence shell of dopants are primary source of the induced magnetism. Theoretically calculated value of induced magnetic moment for both phosphorus as well as arsenic doped at oxygen site in SnO₂ system is $\sim 1\mu_B$ per dopant. Spin-spin interactions study for P and As doped SnO₂ at short distance clearly show long range correlation between the spins leading to strong ferromagnetic coupling. In all other cases (i.e., for X = B, C, N, Al, Si, S, Ga, Ge), the absence of ferromagnetic coupling can be the result of weak spin-spin coupling or domination of anti-ferromagnetic coupling in Sn₂₄X₂O₄₆ system.

The last chapter presents the summary and conclusion of the whole work; it also provides the future outlook and scope of further study in the subject. In the last section, the bibliography used in the whole thesis has been listed.

References

1. J. M. D. Coey, *Solid State Sciences* 7 (2005) 660-667.
2. M. Venkatesan *et al.*, *Nature Commun.* 430 (2004) 630.
3. K. Ando *et al.*, *Science* 312 (2006) 1883-1885.
4. T. Dietl *et al.*, *Nature Mater.* 9 (2010) 965-974.
5. T. Dietl, *Science* 287 (2000) 1019-1022.
6. P. Sharma *et al.*, *Nature Mater.* 2 (2003) 673-677.
7. A. Sundaresan *et al.*, *Phys. Rev. B* 74 (2006) 16106(R).
8. D. Sanyal *et al.*, *Phys. Lett. A* 371 (2007) 482-485.
9. H. Pan *et al.*, *Phys. Rev. Lett.* 99 (2007) 127201.
10. D. Sanyal *et al.*, *J. Phys. D: Appl. Phys* 47 (2014) 025001.
11. N. Kumar *et al.*, *Chem. Phys. Lett.* 477 (2009) 360.

List of Figures

- 1.1 Curie temperature in 5 atomic percent Mn doped semiconductors.
- 2.1. Schematic layout of RIB facility at VECC.
- 2.2. Schematic diagram of positron from a source entering the sample and different mechanism occurring in the sample.
- 2.3. Schematic diagram of positron annihilation life time spectroscopy (PALS).
- 2.4. Schematic diagram of experimental set up for coincidence Doppler broadening of the positron annihilation γ -radiation (CDB) measurements.
- 2.5. Schematic diagram of peak to noise ration improvement upon using different experimental technique.
- 2.6. Schematic diagram of different regions of energy distribution for 511 keV photon that comes after the positron annihilation inside the sample.
- 2.7. Two Josephson junction in parallel with currents I_a and I_b flowing through it.
- 3.1. Carbon atom doped in short position (1, 2) and in long position (1, 3) in the 72 atom super cell of TiO_2 .
- 3.2. Induced magnetic moment of $(\text{Ti}_{12}\text{XO}_{23})_2$ ($X = \text{B, C, N, Al, Si, P}$ and As) system and TiO_2 system with single V_{Ti} and V_{O} .
- 3.3. Comparison of total density of states for pristine TiO_2 and different p-block elements ($\text{B, C, N, Al, Si, P}$ and As) doped TiO_2 system.

- 3.4. The energy difference between ferromagnetic and anti-ferromagnetic state for different p block element doped (at oxygen site) TiO_2 system.
- 3.5. Energy loss and defect profile for 96 MeV oxygen on TiO_2 sample as simulated by SRIM/TRIM software.
- 3.6. Spin polarized density of states for TiO_2 with V_{Ti} ($\text{Ti}_{23}\text{O}_{48}$)
- 3.7. Spin polarized density of states for TiO_2 pristine.
- 3.8. Spin polarized density of states for TiO_2 with V_{O} ($\text{Ti}_{24}\text{O}_{47}$).
- 3.9. Magnetization *vs* applied field curve obtained from SQUID for 96 MeV oxygen irradiated TiO_2 sample.
- 3.10. Positron annihilation lifetime spectra for oxygen irradiated rutile TiO_2 .
- 3.11. Ratio curve constructed from the CDB spectrum for un-irradiated and irradiated TiO_2 with respect to the CDB spectra of 99.9999 % pure Al single crystal.
- 3.12. Ratio curve constructed from the coincidence Doppler broadening spectrum for irradiated TiO_2 with respect to the same for pristine sample.
- 3.13. Magnetization density (spin polarized) of TiO_2 with V_{Ti} (highly localized magnetization is noticed around Ti vacancy due to the nearest oxygen atoms).
- 3.14. Induced magnetic moment for carbon doped TiO_2 system with different configuration.
- 3.15. Spin polarized density of carbon doped TiO_2 at interstitial site.
- 3.16. Spin polarized density of carbon doped TiO_2 at oxygen site.

- 3.17. Magnetization density (spin polarized) distribution in TiO_2 with Co. a) with one C-atom doped at o-site with atomic bonds present in figure, b) with two C atoms doped at O-sites and no atomic bonds in figure.
- 3.18. SRIM simulation for C^{4+} irradiated TiO_2 (a) energy loss profile, (b) vacancy formation profile and (c) distribution of carbon ions with target depth. S_n and S_e represent nuclear energy loss and electronic energy loss respectively.
- 3.19. Magnetization vs field plot for 1.2 MeV carbon implanted rutile TiO_2 .
- 3.20. The induced magnetic moment for nitrogen doped TiO_2 system with various configurations.
- 3.21. (a) Local magnetic density in TiO_2 with N_{inst} , (b) local magnetic density in TiO_2 with N_{O} . The blue color spherical balls represent Ti atoms and yellow color spherical balls represent O atoms.
- 3.22. Spin polarized density of states for TiO_2 with N_{O} .
- 3.23. Spin polarized density of states for TiO_2 with N_{inst} .
- 3.24. SRIM simulation for N^{4+} irradiated TiO_2 (a) The energy loss profile, (b) defect generation profile and (c) nitrogen ions distribution with target depth.
- 3.25. Room temperature magnetic hysteresis loop of N-irradiated TiO_2 .
- 3.26. Partial and total density of states in boron doped system TiO_2 .
- 3.27. Local magnetic density (spin polarised) distribution for boron doped TiO_2 .

- 3.28. SRIM simulation for B^+ irradiated TiO_2 (a) The energy loss profile, (b) defect generation profile and (c) boron ions distribution with target depth.
- 3.29. Magnetization vs magnetic field plot for B- doped TiO_2 .
- 4.1. Schematic diagram of the set up for *in-situ* temperature (above 300 K) dependent Doppler broadening spectroscopy.
- 4.2. Induced magnetic moment for $Zn_{54} X_2 O_{52}$ ($X = B, C, N, Al, Si, N, P, Ge, Ga$ and As) system and ZnO system with single V_{Zn} and V_O .
- 4.3. Energy difference between ferromagnetic and antiferromagnetic states for various p-block elements doped ZnO system.
- 4.4. Spin polarized total density of states for various p-block elements doped ZnO.
- 4.5. Partial and total density of states distribution a) pristine ZnO and b) boron doped ZnO system.
- 4.6. Local magnetic density distribution for boron doped ZnO.
- 4.7. SRIM simulations for B^+ irradiated ZnO (a) The energy loss profile, (b) defect generation profile and (c) boron ions distribution with target depth.
- 4.8. Magnetization vs magnetic field plot for 10 keV B^+ ion beam implanted ZnO.
- 4.9. Variation of *S*-parameter with heating time during in-situ DB spectrum measurement of polycrystalline ZnO.

- 4.10. Area normalized ratio-curves (constructed from CDB spectrum) for differently annealed ZnO with respect to the ZnO single crystal.
- 4.11. PL spectra of the 182 °C and 286 °C annealed ZnO. Inset shows same spectra with NBE peak normalized to 1.
- 4.12. Sub-band gap PL emissions from the defect energy levels for (a) 182 °C and (b) 286 °C annealed ZnO samples. Both the spectra have been fitted with several Gaussian peaks.
- 4.13. 10 K PL spectra of both the ZnO samples. Left inset shows the expanded region of 3.32 eV to 3.45 eV. The right inset shows the difference of NBE PL intensities between 286 °C and 182 °C annealed samples. The difference is highest around 3.311 eV.
- 4.14. Ratio curves of the annealed ZnO with respect to that of the single crystalline ZnO.
- 4.15. Near band edge PL spectrum at 15 K for the 325 °C and 450 °C annealed ZnO. The inset shows the corresponding deep level emissions.
- 5.1. Super-cell of pristine SnO₂ with 2×2×3 unit cell, the blue color spheres are the Sn atoms and yellow color spheres are O atoms. The (a, b) and (a, c) positions are chosen for short distance doping and long distance doping respectively.
- 5.2. Induced magnetic moment in p-block elements doped Sn₂₄X₂O₄₆ (X = B, C, N, Al, Si, P, S, Ga, Ge, As) system SnO₂ system with single V_{Sn} and V_O.
- 5.3. Difference of ground state energy between ferromagnetic and anti-ferromagnetic system for B, N, P and As doped SnO₂. 'S' denotes short position and 'L' denotes long position doping.

- 5.4. Comparison of total density of states for p-block elements doped SnO₂.
- 5.5. Spin polarized density of states for a) P doped SnO₂, b) As doped SnO₂.
- 5.6. Local magnetic density distribution in SnO₂ system with a) two P atoms doped at short position and b) two As atoms doped at short position.

List of Tables

- 3.1. Total energy, defect formation energy (E_{df}) and induced magnetic moment for different elements doped at oxygen site (X_O) of rutile TiO_2 .
- 3.2. Different positron lifetime parameters for unirradiated and oxygen irradiated TiO_2 samples.
- 3.3. The defect formation energy, Induced magnetic moment, Fermi energy and Fermi energy shift for carbon doped at oxygen site with different configurations in TiO_2 .
- 3.4. Defect formation energy (E_{df}), Fermi energy and induced magnetic moment for different nitrogen-doped TiO_2 system.
- 4.1. Total energy, optimized doping distance, defect formation energy (E_{df}) and induced magnetic moment for different elements doped at oxygen site (X_O) of ZnO .
- 5.1. Optimized doping distance, induced magnetic moment, Fermi energy shift and defect formation energy for two B, N, P and As doped at short and long position in SnO_2 .

CONTENTS

	Page No.
Synopsis	i
List of Figures	vi
List of Tables	xi
1. Chapter 1: Introduction	1
2. Chapter 2: Methods and Experimental Techniques	13
2.1 Introduction	13
2.2 Density Functional Theory (DFT)	13
2.3 Ion beam irradiation technique	16
2.4 Positron Annihilation Spectroscopy (PAS)	18
2.4.1 Positron Annihilation Lifetime Spectroscopy (PALS)	20
2.4.2 Coincidence Doppler Broadening of positron annihilation γ -radiation (CDB)	22
2.5 Photoluminescence Spectroscopy (PL)	25
2.6 Superconducting Quantum Interference Devices (SQUIDs)	26
3. Chapter 3: Defect induced Ferromagnetism in TiO₂	28
3.1 Introduction	28
3.2 Computational methodology	29
3.3 Experimental details	31
3.4 Ferromagnetism in p-block elements doped TiO ₂	32
3.5 Room temperature ferromagnetism in oxygen irradiated TiO ₂	38
3.6 Room temperature ferromagnetism in carbon doped TiO ₂	47

3.7 Room temperature ferromagnetism in nitrogen doped TiO ₂	54
3.8 Room temperature ferromagnetism in boron doped TiO ₂	61
3.9 Conclusion	65
4. Chapter 4: Defect induced ferromagnetism in ZnO	66
4.1 Introduction	66
4.2 Computational methodology	67
4.3 Experimental details	68
4.4 Ferromagnetism in p-block elements doped ZnO	71
4.5 Room temperature ferromagnetism boron doped ZnO	76
4.6 Defect generation study in ZnO	81
4.6.1 Defects generation and recovery in polly-crystalline ZnO	81
4.6.2 Defect characterization in ZnO annealed at higher temperature	90
4.7 Conclusion	93
5. Chapter 5: Defect induced ferromagnetism in SnO₂	94
5.1 Introduction	94
5.2 Computational methodology	95
5.3 Ferromagnetism in p-block elements doped SnO ₂	97
5.4 Conclusion	104
6. Chapter 6: Conclusion and future outlook	105
6.1 Conclusion	105
6.2 Future prospect	109
Bibliography	110

Chapter-1

Introduction

In the periodic table the different elements can be classified by their electrical properties as metals, insulators and semiconductors etc. Few metals like Fe, Co, Ni etc. are ferromagnetic at room temperature. However, there is no single material which shows ferromagnetic property, at room temperature, along with its semiconducting properties. Studies of such material (room temperature ferromagnetic along with semiconducting properties) are very important from technological point also from the view point of basic science. In the basic science, the traditional ferromagnetic materials have a common point; the source of magnetism is the unpaired electrons present in the d-orbital of the atoms in the materials. Interestingly the ferromagnetic property, recently, found in some of the semiconducting materials are very difficult to explain, since the elements either have no d-orbital electrons or fully occupied electrons in d/f orbital. This type of recently observed magnetism is called d^0 ferromagnetism [1].

The technological aspect revolves around the idea of exploiting the traditional semiconducting property combined with the ferromagnetic characteristics and spin polarization [2, 3]. Some of the potential applications of magnetic semiconductor include non-volatile memory for computers [2], spintronics devices [4, 5], magneto-optics devices [6], quantum computing [7] etc. In traditional electronics, we have utilized the fact that electrons and ions carry the electric charge in making devices like transistors, diodes, triodes etc. Now, it is a well known fact that apart from electric

charge, electrons also poses a spin, much like the earth spin left or right. But, also it is also a fact that, spin is a quantum variable in nature which means, it can exist in unusual superposition of up and down. People are trying to come up with the ways to understand how one can control the spin property in different types of matter. In the present day, one can get the spintronics devices in read out of hard drive in laptops and computers, as a way to read very small pieces of magnetic information that are stored on our hard drive, in a very efficient way [8]. It is extremely sensitive and accurate, so that the resistance of the current that passes through this head changes with pressure or magnetic field around. But, these systems are based on the metallic system. It is very important opportunity to exploit quantum physics of a quantum variable. So, the information can be stored in two states up or down with binary logic 0 or 1 (i.e. information is there or not there). But building technology based on quantum variable means that the information can be stored as the superposition of states [7]. Present day research focuses largely on semiconductor-spintronics which includes generation of spins in materials at room temperature (i.e. development of room temperature magnetic semiconductors) and to manipulate the spins of a particle using electric field or magnetic field.

The concept of room temperature ferromagnetic semiconductor came into light during the year 2000, when Dietl *et al.*, reported a possibility of room temperature ferromagnetism by doping transition metal ions in some of the semiconductors [9]. The Curie temperature (T_C) of transition metals (Mn, Ni, Co etc.) doped semiconductors was reported to be above room temperature for some cases as shown in **Figure 1.1**. The T_C exceeding room temperature for semiconductors such as GaN and ZnO containing 5% Mn and a high hole concentration ($3.5 \times 10^{20} \text{ cm}^{-3}$); initiated

intense research to realize a room temperature dilute magnetic semiconductor (DMS) based on wide band gap semiconductors.

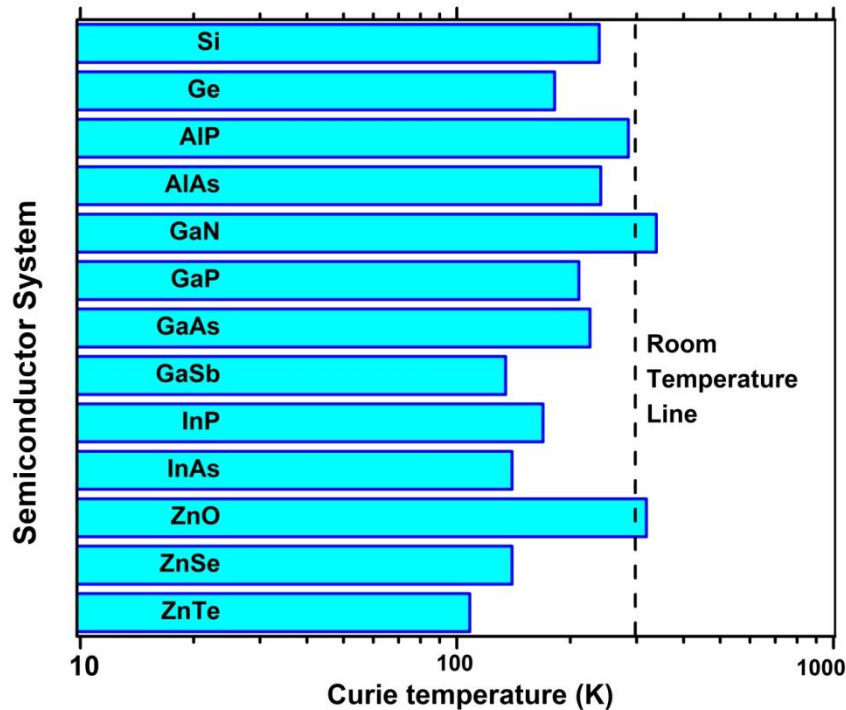


Figure 1.1 Curie temperature in 5 atomic percent Mn doped semiconductors [9].

The earlier studies related to DMS could not predict the ferromagnetism at room temperature. It was experimentally observed that ferromagnetic transition occurs at 1.8 K, in $\text{Cd}_{0.976}\text{Mn}_{0.024}\text{Te}/\text{Cd}_{0.066}\text{Mg}_{0.27}\text{Zn}_{0.07}\text{Te}:\text{N}$ sample with a single modulation doped, 8 nm quantum well [10]. The ferromagnetic transition is proposed to be driven by long range Rudermann-Kittel-Kasuya-Yosida (RKKY) interactions between the spins of Mn atoms Mediated by 2×10^{11} holes per cm^2 [10]. The experimental evidence of room temperature ferromagnetism has been found in Mn doped ZnO, which is well supported by the ab-initio calculations. The ferromagnetism is observed in Mn-doped by pulse laser deposition technique in chemically prepared ZnO sample [11]. The magnetic moment per Mn atoms have been reported to be $0.14 \mu_B$ per Mn atom which

is little less as compared to that calculated from *ab-initio* calculations $\sim 5\mu_B$ [11]. The authors' claims that the lower value of magnetic moment is because the magnetic moment calculated theoretically is for regularly distributed Mn atoms in the ZnO super cell, but in practice the position of Mn atoms change and leads to local anti-ferromagnetic couplings in some cases [11]. Initially, the search of ferromagnetic semiconductors has been focused on generating ferromagnetism in different semiconductors by doping various transition metals [12-16]. Ueda *et al.*, reported ferromagnetic magnetic properties in transition metal doped ZnO (n-type $Zn_{1-x}M_xO$, where, $X= 0.05 - 0.25$; $M= Co, Mn, Cr, Ni$) [12]. Thin films of ZnO has been formed on sapphire substrate using a pulse laser deposition technique some of the Co-doped samples showed higher curie temperature than room temperature (above 280 K), also they showed maximum solubility limit [12]. They observed maximum magnetization for sample with highest doping concentration (i.e. $X=0.15$). Blasco *et al.*, prepared $Zn_{0.96}M_{0.04}O$ ($M= Fe, Co$ and Mn) samples with different synthetic routes and all single phase samples to have paramagnetic semiconductors without any spontaneous magnetization in whole temperature range, also the Ferromagnetism has been observed only in the samples with secondary phases [13]. However, Hu *et al.*, predicted anti-ferromagnetic behavior of Co-doped ZnO system using first principle study [14]. Iusan *et al.*, reported a detailed theoretical calculation for Mn-doped ZnO system, where it was clear that the introduction of acceptor defects like Zn vacancy and N-substitution at O-site along with Mn-doping make the system ferromagnetic [15]. Otherwise, the ZnO system with only Mn-doping makes it anti-ferromagnetic one [15]. They further estimated the curie temperature of Mn-doped ZnO system with defects to be 45 K but it was increased up to 135K with different defect configurations

[15]. Despite of all these efforts, the challenge of getting ferromagnetic property at room temperature was still there [16]. Soon, many experimental evidence confirmed the presence of ferromagnetism in different transition metal ion doped semiconductors at room temperature [17-19]. Punnoose *et al.*, reported paramagnetic behavior in chemically synthesized Fe-doped SnO sample and ferromagnetism in identically synthesized Fe-doped SnO₂ sample [17]. They found that the ferromagnetism increases with increase in Fe doping and Curie temperature was found to be upto 850K for 1 % Fe doping in SnO₂ [17]. Ramachandran *et al.*, showed that the pure ZnO doped with Mn atoms gives anti-ferromagnetic system, whereas, Mn doped samples with oxygen vacancies gives rise to ferromagnetic system [18]. Thus they concluded that a stable ferromagnetism can be generated in ZnO sample with sufficient Mn dopants concentration and oxygen vacancies [18].

Similarly, many other research groups predicted possibility of ferromagnetism in various samples [20-28]. Room temperature ferromagnetism in oxide systems such as ZnO, TiO₂, SnO₂, ZrO₂, CaO, CdO MgO etc. draws a considerable research attention of the researchers throughout the globe [29-32]. The oxides which are popularly studied are ZnO, MgO, CuO, TiO₂, HfO₂, SnO₂ etc. Some of these oxides are discussed in detailed in the following sections.

In MgO system, the report on room temperature, highly spin polarized tunnel injector on MgO [33] draws a huge attention of researchers working on spintronics materials. Mao *et al.*, reported studied crystal orientation dependence of ferromagnetism in single crystal MgO irradiated with 64 keV Fe ions, where the irradiated crystal shows ferromagnetic behavior, both at 5 K and 300 K [34]. It was inferred that the Curie field in the hysteresis curve greatly depends on the

orientation of single crystal, where the (111) orientation shows maximum value [34]. A detailed first principal study on magnetic properties of transition metal (V, Cr, Mn, Fe, Co, Ni) doped MgO reveals that only the Cr-doped system has a stable ferromagnetic behavior with estimated Curie temperature of 182 K [35]. Wu *et al.*, carried out detailed first principal calculations on magnetic properties of transition metal (Mn, Fe, Co and Ni) doped MgO sheet, where, stable ferromagnetic behavior has observed from the 3d-orbital electrons of the transition elements doped in the MgO lattice [36]. Nagar *et al.*, observed ferromagnetism at room temperature in V-doped MgO nano particles, prepared by two step wet chemical process [37]. They varied the concentration of V-doping (0.5, 0.7, 0.9, 1, 1.1 and 1.5) in the MgO sample and found a drastic change in the value of saturation magnetization. The sample with 1% Vanadium showed maximum magnetization in MgO sample, whereas it is less with higher and lower V-concentration [37]. The anomaly of magnetic properties is not clear as the theoretical studies and experimental results are different in MgO system. However, other research groups came out with the idea of defect mediated ferromagnetism in MgO system. Wang *et al.*, reported positron annihilation studies of defects in MgO nanocrystals and its effect on ferromagnetism in the system [38]. The ferromagnetism has observed in MgO nanocrystals at room temperature and the source of magnetism was conjectured to be the interstitial defects, as the positron annihilation spectroscopy reveals that a large number of defects like atomic vacancies, vacancy clusters and defects in the grain boundaries are present in the nanocrystalline sample [38]. Ferromagnetism in undoped MgO samples was also reported by several groups, such as in the thin films of MgO prepared by sputtering followed by vacuum annealing [39] and thin films prepared by RF magnetic sputtering at 350 K [40]. The

MgO thin film prepared under oxygen partial pressure showed highest saturation magnetization while the films prepared under nitrogen partial pressure showed suppressed the magnetization in the sample [40]. Gu *et al.*, reported a possibility of ferromagnetism in N-doped MgO, where, there is finite local magnetic moment for the dopant with long range correlation between the two N atoms in the MgO lattice [41]. However, first principal studies carried out by Pesci *et al.*, suggest that it is difficult to achieve room temperature ferromagnetism in N-doped MgO [42]. Sharma *et al.*, discussed the ferromagnetic property of C and Mn co-doped MgO system, where the co-doped system shows strong long range ferromagnetic interaction [43]. Kuang *et al.*, reported that the C-doped at interstitial site in the MgO lattice can not only generate a localized magnetic moment in the system, but it can also retain the ferromagnetism in the system [44]. There are several other reports of ferromagnetic behavior of MgO such as enhancement of magnetic moment in Al-doped system with the introduction of oxygen vacancy [45], ferromagnetism in pristine MgO system due to intrinsic atomic (cationic) vacancies [46-53].

In CuO system, Yang *et al.*, reported ferromagnetism with Curie temperature 80 K, where Mn has been doped at different concentration and the saturation magnetization increased with increasing dopant concentration [54]. Punnoose *et al.*, reported ferromagnetic properties of CuO nanoparticles prepared by sol gel technique [55]. Filippetti *et al.*, predicted ferromagnetism in Mn doped CuO using first principal studies [56]. The double exchange interaction enables the ferromagnetic coupling both short and long ranges between the spins of Mn dopants [56]. Soon experimental verification came in light, where Mn doped polycrystalline CuO has been prepared by using standard solid state reaction with Mn doping varied upto 5 % [57]. The

ferromagnetism has been observed in the CuO sample with Mn concentration below 1.25 % and also the XPS result reveals the Mn^{2+} state of dopant [57]. Moreover, Zhao *et al.*, claimed ferromagnetism in Mn-doped CuO thin films fabricated on a thermally oxidized silicon substrate [58]. Both experimental and theoretical studies reveal presence of Mn^{2+} ions give rise to magnetism in the system and the super-exchange interactions of Mn-O-Cu-O-Mn coupling and Mn-O-Mn coupling contributes to ferromagnetic and anti-ferromagnetic coupling respectively [58]. However, Renganathan *et al.*, claimed that the presence of defects and oxygen vacancies contributes ferromagnetism in undoped and Mn-doped monoclinic CuO nanoflakes, synthesized by wet chemical method [59]. Manna *et al.*, reported room temperature ferromagnetism in pure and Fe-doped CuO nanorods, synthesized by template free solution methods, where, pristine CuO nanorods show weak ferromagnetism which gets enhances with the introduction of Fe within CuO lattice [60]. Ferromagnetism has been also observed in pure CuO powders prepared by sol gel method [61], CuO nonowires grown by thermal oxidation [62] and CuO nonosheets prepared by hydrothermal synthesis [63], which supports the argument that defect and vacancies induces ferromagnetism in CuO samples.

In case of CdO system, Rajkumar *et al.*, reported the possibility of ferromagnetism in Mn doped CdO nano-particles synthesized by sol-gel technique at room temperature [64]. Zhang *et al.*, theoretically calculated the amount of magnetization in nitrogen atom doped CdO at different position [65]. Similarly, Ogale *et al.*, reported ferromagnetic behavior of Co-doped SnO_2 sample at higher temperature ($T_C = 650$ K), with magnetic moment of $\sim 7.5 \mu_B$ per dopant [66]. Espinosa *et al.*, studied ferromagnetic property in SnO_2 based multilayer consisting of

SiO_2 , Si, Al, Mn or MnO_x , where only Mn-doped system was found to be successful in inducing ferromagnetism at room temperature, other cases show paramagnetic behavior [67]. Zhang *et al.*, observed ferromagnetism at room temperature in Ni-doped SnO_2 thin films prepared by sol-gel method [68]. The saturation magnetization decreases with increase in Ni concentration due to anti-ferromagnetic super-exchange interactions among the dopants present in the nearest neighborhoods [68].

Matsumoto *et al.*, reported room temperature ferromagnetism in TiO_2 thin films doped with Co with various concentrations, where, a net magnetic moment of $0.32 \mu_B$ per dopant was reported [69]. Chambers *et al.*, also reported about $1.26 \mu_B$ magnetic moment per dopant in epitaxial Co-doped anatase TiO_2 by pulse laser deposition technique, grown on SrTiO_3 substrate at room temperature [70]. Bryan *et al.*, observed about $1.9 \mu_B$ magnetic moment in Co-doped anatase TiO_2 nanocrystals, where Co atoms are in Co^{2+} state produce stable ferromagnetism even at room temperature [71]. Duhalde *et al.*, reported room temperature ferromagnetism in Cu-doped TiO_2 thin films grown by pulse laser deposition and the magnetic moment per dopant was calculated to be $1.5 \mu_B$ [72]. Moreover, the *ab-initio* calculations suggest that oxygen vacancies near the dopant are crucial for generating magnetic moment in the Cu-doped TiO_2 system [72]. Hong *et al.*, observed room temperature ferromagnetism in V-doped anatase TiO_2 thin films, grown on the LaAlO_3 substrates by laser ablation techniques [73]. They also reported room temperature ferromagnetism in transition metals (V, Cr, Fe, Co, Ni) doped TiO_2 thin films deposited on LaAlO_3 substrates by ablation laser technique, but the maximum saturation magnetic moment is observed for V-doped sample [74].

However, the contribution of magnetic property in the transition metal ion doped system has been observed from the dopants itself. As a result, the origin of ferromagnetic behaviors in these oxides was debatable. Venkatesan *et al.*, [75], reported ferromagnetism in the thin films of HfO₂ without any doping. Later, it has been observed by many groups that the induced magnetism can be associated with the defects into the system [76-78]. A stable ferromagnetism has been reported in nanocrystalline semi-conducting oxides [76]. The source of magnetism was proposed to be the atomic vacancies in the samples. Also, stable room temperature ferromagnetism was experimentally observed in the nano-crystalline ZnO samples. The positron annihilation spectroscopy (PAS) reveals the presence of atomic vacancies in the sample, mostly Zn vacancies and combination of O-vacancies. The sample containing vacancy shows magnetic behavior [78]. Soon researchers identified the possibility of room temperature ferromagnetism in different wide band-gap semiconductors by doping non magnetic elements [79-87]. The source of magnetic moment in these classes of semiconductors is the p-orbital electrons. Moreover, it has been observed that room temperature ferromagnetism in various oxides (viz., TiO₂, SnO₂, MgO, ZnO etc.) can be generated simply by creating atomic vacancies in the system [88-93]. The detailed literature review on the ferromagnetic property of oxides under study i.e., TiO₂, ZnO and SnO₂ with non magnetic defects has been presented in the introduction section of chapter 3, chapter 4 and chapter 5 respectively.

The present work aimed to investigate the magnetic property of various semiconducting oxides (viz. TiO₂, ZnO and SnO₂) by introducing non-magnetic defects into the system. Various p-block elements have been doped at O-site and magnetic moment has been calculated for all the system after structure optimization.

The details study for TiO₂, ZnO and SnO₂ system have been reported in chapter 3, chapter 4 and chapter 5 respectively. The formations of defects are very common in crystal, such vacancies also contribute to the net magnetic moment in some cases as discussed above. Hence, the effect of atomic vacancies has been studied explicitly in case of C-doped TiO₂ and N-doped TiO₂. Various ion beams (B, C, N, O) of different energies has been irradiated on the samples. The defects formation in the irradiated sample has been characterized by PAS wherever possible. The magnetic characterization is carried out using SQUID magnetometer.

In case of TiO₂, it is clear that both cation vacancies [90] and anion vacancies [88] give rise to ferromagnetic property. Similarly, for SnO₂ system the cation vacancies are responsible for magnetization [93]. But in case of ZnO system, the only known experimental fact is that the atomic vacancies give rise to magnetism [78], but experimental evidence of the nature of atomic vacancies, which induces the magnetism, is not available. Apart from this, defects in zinc oxide material bears wide range of scientific interest [94-103]. Such as, the generation, migration or recovery of defects in ZnO is studied for the purposeful material design to meet technological requirements. On the theoretical side, correctly predicting the defective state of ZnO is still a challenge for the model calculations [80, 104, 105]. A large number of studies concerned with changes induced in ZnO system due to high temperature annealing [95-96], relatively fewer works exist on similar changes below 300 °C [98]. Specially, the samples annealed below 300 °C are defect rich and offer wide scope for tuning material properties. Such ZnO systems contain zinc vacancy (V_{Zn}) type defects in the form of clusters [96], complexes [106] or pairs [105-107]. A section in chapter 4 of this thesis, we have tried to understand the types of defect formation in ZnO system at

higher temperature as well as in low temperature as the atomic defects have significant role in inducing ferromagnetism in ZnO [78]. Positron annihilation spectroscopy techniques in-situ 'S-parameter' measurement below 300 °C along with the ratio curve analysis for off-line coincidence Doppler broadening (CDB) spectrum of samples; annealed at different temperature have been carried out to understand the complex nature of defect formation in ZnO system. The change in defective nature of granular ZnO systems annihilated at various temperatures has also been assessed by measuring ex-situ photoluminescence (PL) measurements at cryogenic temperatures.

This thesis has been divided in six chapters. Chapter 1 is the introduction to the thesis which gives the insight of the subject starting from the scope of study and development of field followed by the objective of the study. The working principle and details of experimental and theoretical methodology used in this study are presented in chapter 2. Chapter 3, chapter 4 and Chapter 5 are the results and discussion part of the thesis. Three different oxide systems namely TiO₂, ZnO and SnO₂ have been taken to study the room temperature ferromagnetic property in non-magnetic oxides. The study related to each oxide is presented in chapter 3, chapter 4 and chapter 5. Finally, chapter 6 summarizes the thesis and the scope for future study has been briefly discussed.

Chapter-2

Methods and Experimental Techniques

2.1 Introduction

In this chapter, both the theoretical methods and experimental techniques used in the thesis have been described. The *ab-initio* calculations are performed using Density Functional Theory (DFT) and the results are analyzed to predict the magnetic properties of the materials. According to the DFT prediction, the experiments are planned, sample preparation have been carried out and their characterizations have been done using different techniques (viz., PAS, PL, SQUID etc.) as described below.

2.2 Density Functional Theory (DFT)

Density functional theory commonly known as DFT is one of the most widely used and accepted theory both in condensed matter physics and material science. It is also the most successful method to solve many body problems to predict electrical, magnetic and optical properties in matter. It is governed by two simple theorems known as Hohenberg-Kohn theorems [108] which can be written as follows.

- i. The ground state energy is a unique functional of electron density. i.e. $E = F[n(r)]$; $n(r)$ is the electron density. Also there exists a unique electron density corresponding to each ground state.
- ii. The electron density that minimizes the energy of the overall functional is the true ground state density corresponding to the full solution of the Schrodinger wave equation.

i.e. $E_0 = \min [E(n(r))]$; E_0 is the ground state energy.

Since, the DFT uses density as a variable, it depends only on three coordinates and the degree of freedom gets reduced to 3. Unlike the case of wave function (e.g. Hartree-Fock method), where for n particles system, the degree of freedom becomes 3n. DFT offers an excellent tool to bring many-body equation into a single one-body like problem using the famous Kohn-Sham equation [109]. The Kohn-Sham equation for a body containing n-electrons is given in equation (1).

$$\left[\frac{\hbar}{2m} \nabla^2 + V_C(r) + V_{ee}(r) + V_{XC}(r) \right] \psi_i(r_i) = \varepsilon(r) \psi_i(r_i) ; i= 1, 2, \dots, n \dots (1)$$

Where, the first term in equation (1) represents kinetic energy of electrons, $V_c(r)$ is the coulomb potential due to the nucleus without electron-electron interactions, V_{ee} is the potential from electron-electron interaction and V_{XC} is the exchange interaction potentials arising from the interaction from ions and other nucleus present in nearby surrounding. Thus, the total energy can be written as

$$E[n] = T[n] + \int [d^3r.n(r)\{V_C(r) + V_{ee}(r)\}] + E_{XC}[n] \dots (2)$$

Where, E_{XC} is the exchange interaction energy to be estimated using different approximations. The most widely used approximations are Local Spin Density Approximation (LDA/LSDA) and Generalized Gradient Approximation (GGA). In LDA the potential depends upon local electron density as given by equation 3, whereas in GGA the potentials depend upon the gradient of electron density along with the local electron density given by equation 4.

$$E_{XC}^{LDA}(n) = \int d^3r V(r) \dots (3); \text{ Where, } V(r) = -\left(\frac{3}{\pi}\right)^{\frac{1}{3}} n^{\frac{1}{3}}(r)$$

$$E_{XC}^{GGA}(n) = E_{XC}^{LDA}(n) + \int \nabla n(r) d^3r \dots (4)$$

In practical applications, the contribution of inner core electrons is replaced by pseudo-potential. Pseudo-potential as the name suggests, is not an exact potential contribution for the atom under consideration but the value of potential for core electrons with nearest noble gas configuration. While solving the K-S equation, the basis set is divided into core region and outer region. The wave functions of core electrons are localized and rapidly varying near nucleolus, but the valence electrons have a plan wave behavior away from nucleolus. Also, the wave functions of core electrons do not change in chemical bonds, only the valence electrons play significant role in the chemical bonds formation. Thus, the inner cores are replaced by pseudo-potential and the plane wave part is solved by applying proper precautions. So, to begin with the computation in DFT, a density is assumed and effective potential is calculated by calculating individual potential contribution, the K-S equation is solved and the wave function is found out for the system. Using the wave function, the density is re-calculated, if it matches with initial guess under the tolerance limit-self-consistency is achieved, total ground state energy can be calculated. But, if the initial and final densities do not match, new density is constructed and used as initial density guess, this process continues till the self-consistency is reached. There are number of packages (like VASP, ABINIT, Quantum EXPRESSIO, WIN2K, CASTEP etc.) that use the concept of density functional theory and pseudo-potentials to solve K-S equations. In the present work, the theoretical simulations using density functional theory have been calculated using VASP (Vienna Ab-initio Simulation Package) build in MedeA software.

2.3 Ion beam irradiation technique

Energetic ions beam of desired energy can be obtained with the help of accelerators. These ions beams are irradiated on materials to prepare different class of materials. Depending upon the energy of ion beam, various phenomena can occur inside the materials. For keV range ion beam, mostly surface sputtering and atomic vacancies can be formed while, for higher energetic particles, most common phenomenon is doping/implantation of projectile in the sample along with generation of atomic vacancies in the sample. In the present case, the ion beam of various energies is used for doping of various atoms as well as generation of vacancy defects in sample. The ions beam with energy range of 10 keV to 1.2 MeV has been obtained using RIB facility at VECC, Kolkata [110-111]. The part of schematic diagram of the RIB facility, up to which the beam is taken, has been shown in **Figure 2.1**.

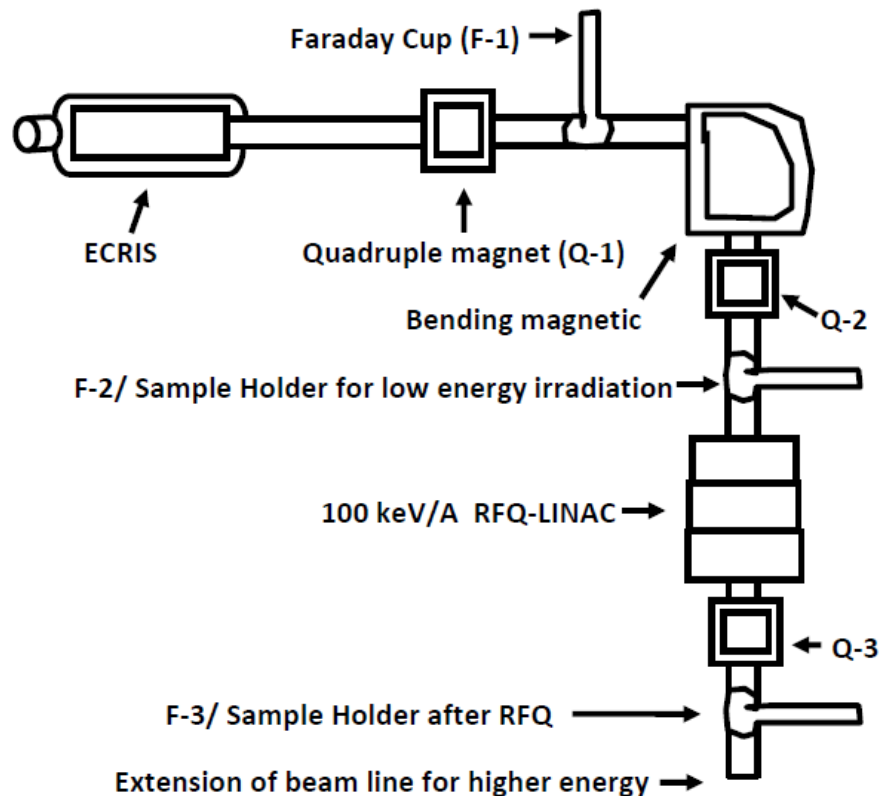


Figure 2.1 Schematic layout of RIB facility at VECC.

First of all, ions source is generated at Electron Cyclotron Resonance Ion Source (ECRIS), where gas or pellets are inserted to produce desired ions. The ions formed in the ECRIS are accelerated using strong extraction voltage (kV), that moves out with the kinetic energy equivalent to extraction voltage times the electronic charge of ions. The ions beam is focused using quadruple magnet at the Faraday Cup (F_1) placed in the beam line. The F_1 measures the total beam current of all the ions that comes out of the ECR source. Bending magnet present after the ECRIS only allows the desired ions following the mass selection (mass number/charge of ion) method. Depending upon the charge state of the ions and the extraction voltage, desired ions with desired energy can be obtained after the bending magnet. After the bending magnetic again there is one quadruple magnet that focuses the selected ion beam in faraday cup (F_2). The faraday cup measures the selected ions beam current. The faraday cup can be removed and the sample holder can be placed in the beam line. In the present work, 10 keV B⁺ and 50 keV N⁴⁺ beam has been irradiated in the sample after the bending magnetic and before the radio frequency quadruple LINAC (RFQ). However, the 1.2 MeV C⁴⁺ ion beam has been irradiated after the RFQ. After passing through the RFQ, the energy of ions beam becomes 100 keV/A. Hence, for carbon ions with mass number (A=12), the energy of carbon ions after RFQ becomes 1.2 MeV. The ion beam that comes out of the RFQ is again focused at the faraday cup (F_3) using a quadruple magnet present in the beam line. The beam current if the ions falling at the sample has been measured using the faraday cup and the sample holder is placed in the beam line by removing the Faraday cup. The beam current of the ions has been fixed about 1-10 μ A at the sample. The ions fluence (number of ions falling in the sample per cm²) has been monitored using the current integrator, which

measures the number of electron passing through it. The charge deposited at the sample due to irradiation of charged ions gets neutralized by passing current through the current integrator, where current integrator is grounded. In order to minimize the loss of sputtered ions and electrons, cylindrical suppressors are used with negative suppression voltage. Highly energetic, 96 MeV oxygen ions beam has been obtained using 15D pelletron facility at Inter University Accelerator Centre (IUAC), New Delhi, India.

2.4 Positron Annihilation Spectroscopy (PAS)

Positron annihilation spectroscopy is non-destructive and one of the most reliable techniques to identify and characterize defects in solids. It has many advantages in condensed matter physics. No special sample preparation is required and it is inexpensive and commercially available technique. The information is carried out by the annihilation of positron inside the matter and causes no damage in the sample. The positrons can be obtained from the natural radioactive source (like ^{22}Na , ^{64}Cu , ^{58}Co etc.) or can also be produced in the lab using accelerators.

When an energetic positron is inserted inside the condensed matter system, it first slows down to thermal energy (thermalisation) and loses its energy. The time taken for the thermalisation process inside matter is few pico-seconds. The mean implantation range varies from 10 to 1000 μm . This depth ensures that positrons carry out the information for the bulk of the sample. Finally, after reaching the thermal equilibrium, the positron annihilates with nearby electron and dominantly giving rise to two 511 keV gamma in 180 degrees apart as shown in the **Figure 2.2**.

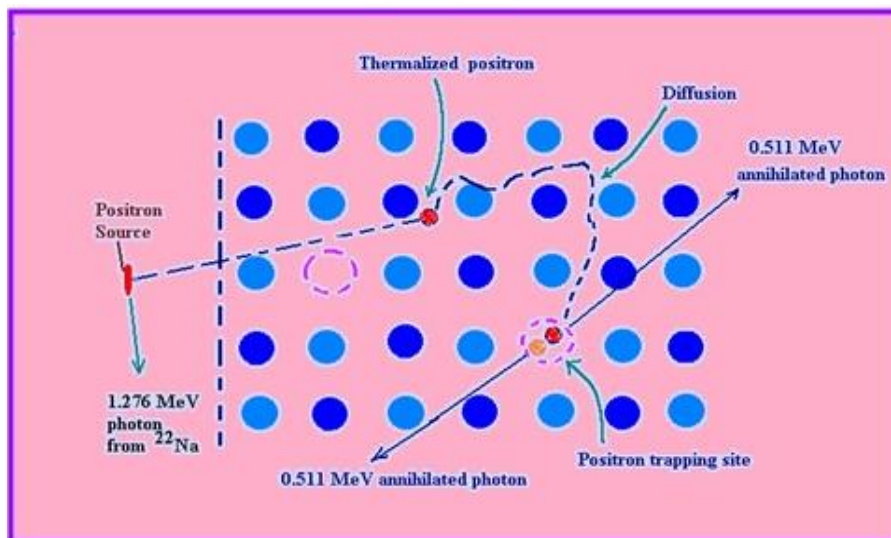


Figure 2.2 Schematic diagram of positron from a source entering the sample and different mechanism occurring in the sample.

The positron inside the materials can capture electrons from the surrounding electrons and a bound state can be formed. As the size of the positronium is twice the size of hydrogen atom, the positronium will only formed for open volume defects whose size is at least two times larger than the size of hydrogen atom. The positronium formed can be either in singlet state (parapositronium) or in triplet state (orthopositronium). The energy splitting between these two states is only 8.4×10^{-4} eV. Parapositronium self annihilates into two photons (511 keV gamma 180° apart) in about 125 pico-seconds. This lifetime is same as the free positron lifetime in bulk of the sample. Orthopositronium decays via three gamma emission mode in vacuum. Life time of orthopositronium decay is around 142 ns, which is three orders of magnitude high as compare to that of parapositronium. Whenever the orthopositronium atom exists in a material, a competing mechanism called pick-off annihilation (positron of orthopositronium suffers $2\text{-}\gamma$ annihilation in collision with a foreign electron having opposite spin) is always present, which reduces the lifetime of

orthopositronium to few nanoseconds inside the condensed matter system. There are three main positron annihilation techniques namely, Positron Annihilation Lifetime Spectroscopy (PALS), Coincidence Doppler Broadening of positron annihilation γ -radiation (CDB) and angular correlation spectroscopy techniques. Here we shall go through one by one for first two techniques, which are used in the thesis work.

2. 4.1 Positron Annihilation Lifetime Spectroscopy (PALS)

The 10 μCi ^{22}Na is the most commonly used positron source for lifetime spectroscopy. The positron source is prepared on a thin material (nickel, mylor, kepton etc.) and it is sandwiched between two identical sample pallets as shown in **Figure 2.3**. The ^{22}Na source emits positron and after ~ 3 ps emits a gamma ray with energy 1.276 MeV. The positron goes inside the sample and annihilates two 511 keV photon as described earlier. The detection of initial 1.276 MeV gamma acts as a start pulse and detection of 511 keV gamma ray serves as a stop signal. The time interval between the detection of 1.76 MeV and 511 keV photons is the life time of positron inside the sample. Thus, makes the experimental system to act as a clock that monitors the life time of positron.

The 2γ - annihilation cross-section is derived by Dirac for the non-relativistic limit. The annihilation probability of positrons per unit time or annihilation rate (λ) is thus given by $\lambda = \frac{1}{\tau} = \pi r_0^2 c n_e$; Where, r_0 is the classical electron radius, τ is the positron lifetime, c is the velocity of light in vacuum and n_e is the electron density at the site of positron. So, knowing the life time of the positron inside the sample, one can get the information of electron density distribution inside the materials. The whole lifetime spectrum is de-convoluted in three lifetime components (τ_1 , τ_2 and τ_3). τ_1 is

assigned to free annihilation of positrons from the bulk of the sample, τ_2 is assigned for atomic vacancies or small vacancy clusters and τ_3 is the lifetime corresponding to open volume defects or the lifetime corresponding to the formation of positronium in the sample. A schematic experimental set up of PALS is shown in **Figure 2.3**. The positron sample-source sandwich is placed in between two BaF_2 detectors (timing resolution of 220 ps) coupled with the photomultiplier tubes. The photon quanta is detected by the BaF_2 crystal and converted into weak electrical signal, which is pickup by photomultiplier tube and gives out a strong pulse that gets recorded in multi channel analyzer (MCA).

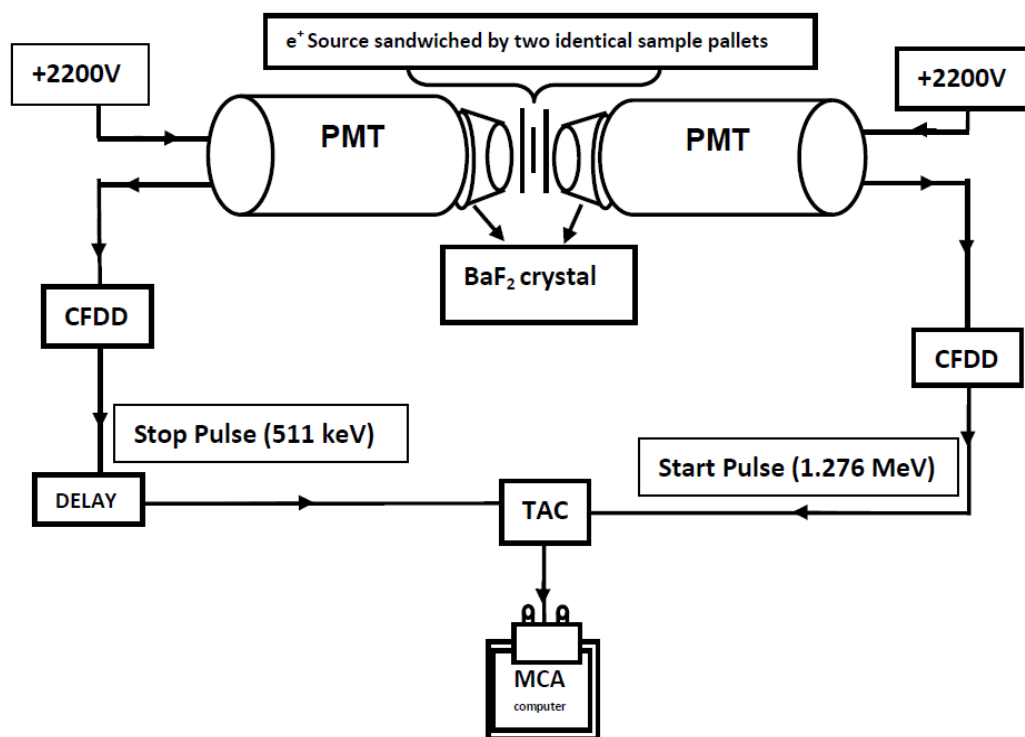


Figure 2.3 Schematic diagram of positron annihilation life time spectroscopy (PALS).

2.4.2 Coincidence Doppler broadening of positron annihilation γ -radiation (CDB)

As soon as the positron interacts with electron inside matter, the motion of thermalised positron is almost zero. The motion of electron-positron pair causes a Doppler shift in 511 keV gamma photons. The amount of Doppler shift (ΔE) is given by equation (5).

$$\Delta E = \frac{p_L c}{2}; p_L = p \cos \theta \dots \dots \dots (5)$$

Where, the kinetic energy of electrons (E) is $p^2/2m_0$, m_0 is the rest mass of electron, p is the momentum of electron to which positron gets annihilated inside materials, ($180^\circ - \theta$) is the angle between the two 511 keV gamma ray photons. Measuring the Doppler shift in energy of annihilating photons, one can get the information of the momentum of electrons. Thus CDB measurements reflect the momentum distribution of electrons in the matter. The Experimental set up for CDB measurements is shown in **Figure 2.4**.

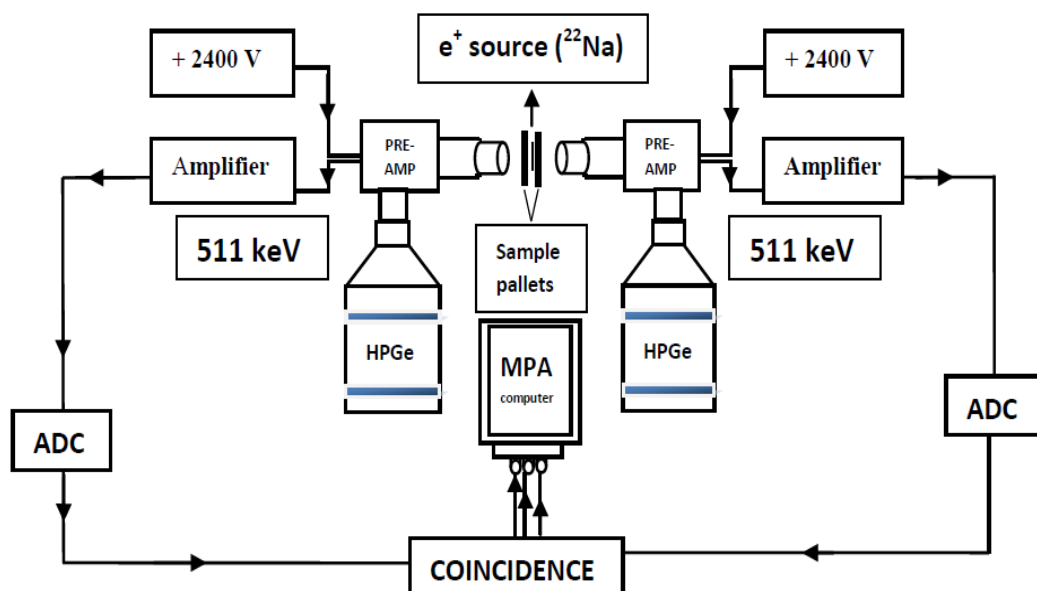


Figure 2.4 Schematic diagram of experimental set up for coincidence Doppler broadening of the positron annihilation γ -radiation (CDB) measurements.

The sample source sandwich is placed between two HPGe detectors. The resolution of HPGe detector (efficiency 13%) used in our case is 1.10 keV for 514 keV γ -ray line from ^{85}Sr source. The signal from HPGe detector (Preamplifier build inside HPGe detector) goes to amplifier and to the Analog to Digital Converter (ADC) and then to the Multi-channel analyzer (MPA). The coincident γ -quantum serves to reduce the background arising mainly from the 1.27-MeV γ -quanta of the β^+ -decay in the source. In this way the background can be suppressed by at least two orders of magnitude as shown in **Figure 2.5**. The signal to noise ratio for the two 511 keV gamma signal from two detector coincidence mode is 14000:1. The coincidence mode allows us to take $\pm \Delta E$ selection of Doppler shift as it has two 511 keV gamma in an opposite direction. Using $\pm \Delta E$ selection of Doppler shift, the signal to noise ratio further improves to 100000:1.

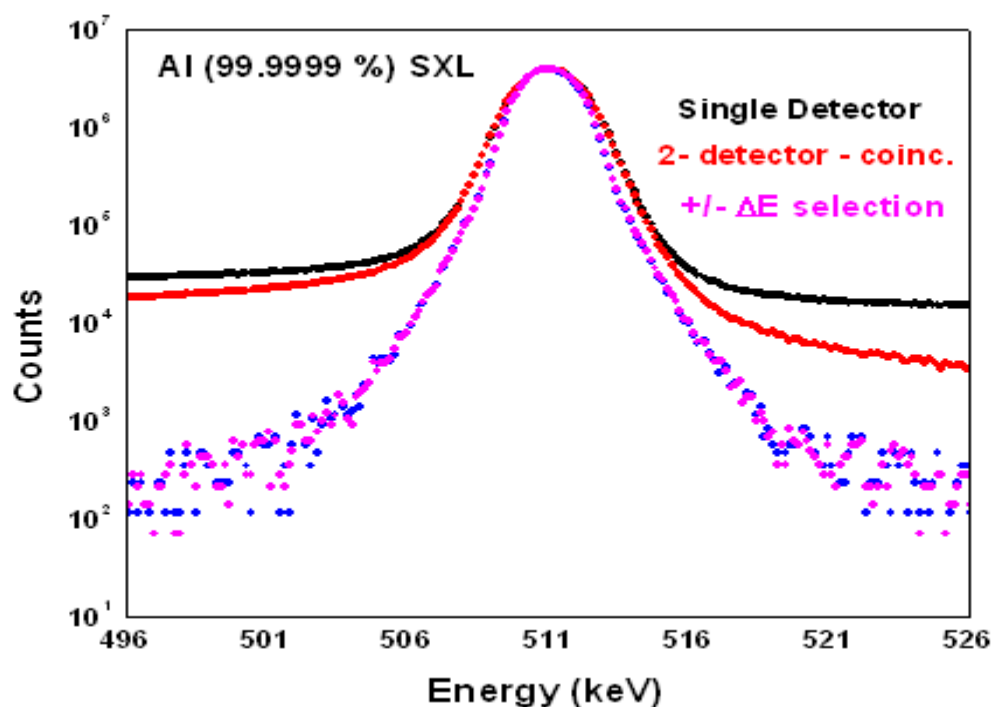


Figure 2.5 Schematic diagram of peak to noise ratio improvement upon using different experimental technique.

The quantitative evaluation of coincidence Doppler-broadening spectrum can be carried out with specific line shape parameters which are called ‘S’ i.e., shape and ‘W’ i.e., wings parameter. The S parameter is defined as the ratio of the area of central low-momentum part of the spectrum and the area below the whole curve as

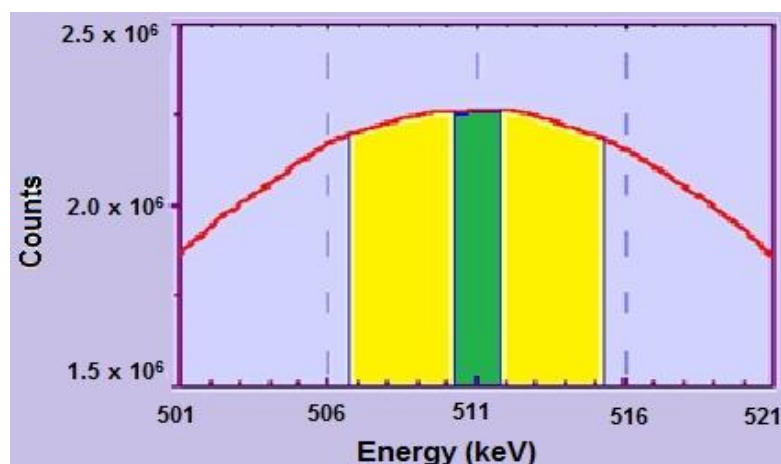
$$S = \{counts(511 \pm 0.85)keV\} / \{counts(511 \pm 4.25)keV\} \dots \dots \dots (6)$$


Figure 2.6 Schematic diagram of different regions of energy distribution curve of 511 keV photon that comes after the positron annihilation inside the sample.

Equation (6) is used to calculate the value of S-parameter. It is the ratio of area between green color region to yellow color region as shown in **Figure 2.6**. As the defect concentration increases in the sample, the positron get annihilates with nearly free electrons in the outer cell as their wave function is spatially extended. The core shells electrons are localized inside and do not span inside the open volume. The increase of S-parameter directly indicates an increase of open defects inside the sample. The W parameter is taken in a high-momentum region far from the center. The W parameter is more sensitive to the chemical surrounding of the annihilation site than the S parameter, because the core electrons having a high momentum are

contributing mainly in the region of large energy deviations from the annihilation energy of 511 keV.

2.5 Photoluminescence Spectroscopy (PL)

A Photoluminescence technique involves the measurement of energy distribution of emitted photon after the optical excitation. Technically two different kinds of luminance have been observed in matters, fluorescence (the emission time scale is in nano-sec) and phosphorescence (emission time scale lasts up to hours or even days). In fluorescence the exciton decays from excited states and reaches a lower vibrational energy state. Generally, the radiation thus emitted has less frequency than that of initial absorption. But phosphorescence occurs when two excited states of different spins have same energy. The selection rule forbids this transition but electron gets transfer between excited states kinetically (by non radiation transitions such as collisions). Then the electrons arrive in the ground state by losing its vibrational energy in terms of radiation in a slow rate. The analysis of energy distribution from PL spectrum gives information of defect species, defect concentration, possible stimulated emission etc. The defects will form some localized defects levels in the band gap which participate in the radiative transitions. PL energy associated with these levels is used to identify various defect species. Also the intensity of PL spectra provides relative information concentration. Photoluminescence spectroscopy is a powerful and non destructive technique which makes it more suitable for materials characterization. In the present work, Photoluminescence (PL) spectroscopy has been carried out at Indian Institute of Technology Kharagpur (IIT Kgp) using 325 nm He-Cd laser as excitation source and a TRIAX 320 monochromator fitted with cooled Hamamatsu R928 photomultiplier detector.

2.6 Superconducting QUantum Interference Devices (SQUIDS)

The superconducting quantum interference device (SQUID) consists of two superconductors separated by thin insulating layers to form two parallel Josephson junctions. The interference between two junctions caused by the difference in the phase of the arrival of the currents through two different paths is read out. In the **Figure 2.7**, two junction 'a' and 'b' connected in parallel and the ends P and Q are connected to electrical instruments which measure any current flow. The external current J_{total} will be the sum of the currents through the two junctions. Let J_a and J_b are the currents through the junction a and b respectively and let δ_a and δ_b are the phase of current between a and b. Now the phase difference between any routes must be same in any route for interference to occur. The phase difference between the P and Q through the route is δ_a plus the line integral of the vector potential along the upper route.

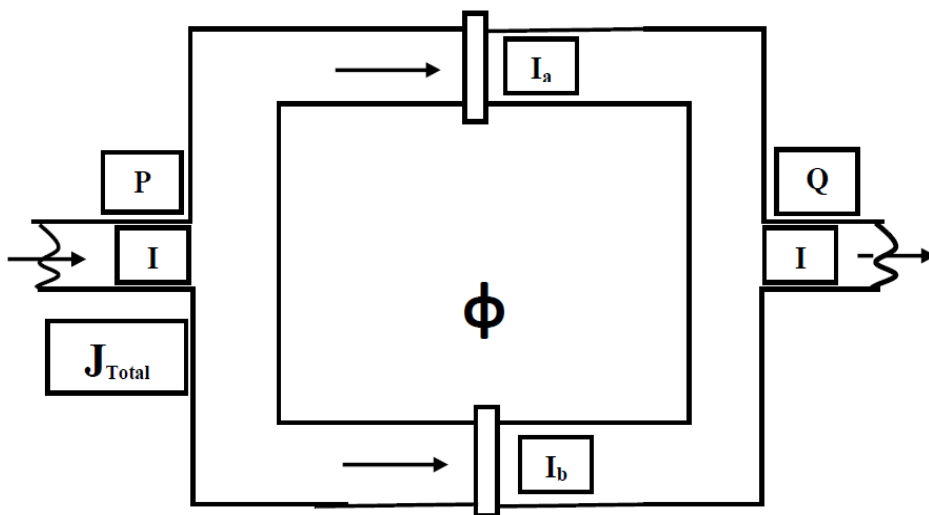


Figure 2.7 Two Josephson junction in parallel with currents I_a and I_b flowing through it.

$$\text{Since, } \hbar \nabla \theta = qA \Rightarrow \nabla \theta = \frac{q}{\hbar} A \Rightarrow \theta = \delta_0 + \frac{q}{\hbar} \int_{\text{upper}} A \cdot dl \dots \dots (7)$$

Thus, the phase difference between the P and Q through the route a is given by

$$\Delta phase_{p \rightarrow Q} = \delta_a + \frac{2e}{\hbar} \int_{upper} A \cdot ds \dots (8)$$

Similarly, the phase difference between the P and Q through the route b is given by

$$\Delta phase_{p \rightarrow Q} = \delta_b + \frac{2e}{\hbar} \int_{lower} A \cdot ds \dots (9)$$

Thus, the phase difference between the points P and Q is the total phase difference i.e.,

$$\delta_a - \delta_b = \frac{2e}{\hbar} \oint A \cdot ds \dots (10)$$

The closed line integral of 'A' is the magnetic flux ' ϕ ' through the loop.

$$\delta_a - \delta_b = \frac{2e}{\hbar} \phi \dots (11)$$

Hence, for any flux through this closed loop between two Josephson junction can be measured by measuring the phase difference between the Josephson junctions. The device may be configured as a magnetometer to detect incredibly small magnetic field small enough to measure the magnetic fields in living organisms. SQUID have been used to measure the magnetic fields in mouse brains to test whether there might be enough magnetism to attribute their navigational ability to an internal compass. The large sensitivity of the SQUID devices is associated with measuring changes in magnetic field associated with one flux quantum. One of the discoveries associated with Josephson junctions was that the flux is quantized in units of $h/2e$. If a constant biasing current is maintained in the SQUID device, the measured voltage oscillates with the changes in phase at the two junctions, which depends upon the change in the magnetic flux. Counting the oscillations allows us to evaluate the flux change which has occurred.

Chapter-3

Defect induced ferromagnetism in TiO₂

3.1 Introduction

As discussed in chapter one, TiO₂ is one of the promising candidates for spintronics application. It is a wide band gap semiconductor with a band gap of 3.2 eV [112]. Due to this large band gap, TiO₂ is used as UV absorber and with the incorporation of defects/impurities its band gap can be tuned for other wavelength absorption [113-114]. Also, the non-toxic and environmental friendly nature of TiO₂ makes it a very popular material [115]. Rutile TiO₂ in pristine form show diamagnetic nature. But, in the recent decade, researchers have discovered ferromagnetism in TiO₂. It has been identified that the defects can play a unique role in inducing ferromagnetism on non-magnetic semiconductors [81, 88, 90]. Peng *et al.*, theoretically showed that an isolated Ti vacancy in TiO₂ induces a magnetic moment of $\sim 3 \mu_B$. While, isolated di-vacancy of titanium induces a moment of $\sim 2 \mu_B$ [116]. Yang *et al.*, [117] reported a magnetic moment of $2.0 \mu_B$ in anatase TiO₂ upon substitution of oxygen by carbon atom. They also reported a significant magnetic moment in both anatase and rutile phases of TiO₂ by replacing oxygen atoms by nitrogen. Bai *et al.*, [118] studied ferromagnetic property of nitrogen doped at oxygen site (N_O) in anatase TiO₂ and reported a magnetic moment of $1.0 \mu_B$ per N dopant. They have calculated the magnetic moment for five different distances in anatase TiO₂ and concluded that doping of nitrogen impurity leads to anti-ferromagnetic coupling of spins as the formation energy for opposite spin alignment is less than that of

parallel spin alignment. Despite of all these studies, there is no clear understanding of magnetic properties of p-block elements doped TiO₂. In TiO₂ intrinsic defects like oxygen vacancies, metal vacancies, metal interstitials, formation of Ti³⁺, formation of O⁻ etc. are present [119]. To have a complete understanding it is necessary to study the effects of atomic vacancies along with the doping of different atoms.

In the present chapter, the magnetic property of various p-block elements doped TiO₂ as well as the effect of atomic vacancies in TiO₂ system has been discussed. Both the oxygen and titanium sites have been chosen for doping. The effect of oxygen vacancies have also been considered explicitly for carbon and nitrogen doping for complete understanding of the process. Energetic ion beam have been irradiated for creating defects (vacancy and implantation/doping) in the sample. The vacancy defects characterizations have been carried out using PAS techniques and the magnetic measurements have been carried out using SQUID magnetometer.

3.2 Computational Methodology

Vienna *ab-initio* simulation (VASP) code [120-123], along with the MedeA software package have been employed for the theoretical calculation based on the density functional theory (DFT). A Tetragonal unit cell of rutile TiO₂ having space group P4₂/mnm with optimized lattice constants of $a = b = 4.59 \text{ \AA}$ and $c = 2.96 \text{ \AA}$ has been used for calculations. The super cell size for all the calculations has been taken to be 2×2×3 unit cells (i.e., with 72 atoms in a super cell of rutile TiO₂). The generalized gradient approximation (GGA) with Perdew-Burke-Ernzerhof (PBE) exchange and correlation [124] method has been used throughout the calculations to study all the system. Periodic boundary conditions have been introduced along all the basis vectors.

In the pristine TiO_2 supercell, two Ti atoms and two O atoms have been substituted systematically with various p-block elements (i.e., $\text{Ti}_{24}\text{X}_2\text{O}_{46}$; $\text{X} = \text{B}, \text{C}, \text{N}, \text{Al}, \text{Si}, \text{P}, \text{Ga}, \text{Ge}, \text{As}$). Carbon and nitrogen doped TiO_2 system have been studied explicitly to see the effect of oxygen vacancies in the system with different configurations (i.e., $\text{Ti}_{24-m}\text{X}_{m+n}\text{O}_{48-n}$, n and m are integers). The oxygen vacancies (V_O) are introduced at different configuration in the carbon doped TiO_2 system (like carbon atom doped at O-site (C_O), carbon atom doped at Ti-site (C_Ti), carbon atom doped at interstitial site (C_i)). Similarly, nitrogen doped TiO_2 system with various configurations {i.e., TiO_2 with nitrogen doped at O site (N_O), nitrogen doped at Ti site (N_Ti), nitrogen doped at interstitial site (N_inst), TiO_2 with both oxygen and titanium vacancy ($\text{V}_\text{O} + \text{V}_\text{Ti}$), nitrogen doped at O site with Ti vacancy ($\text{N}_\text{O} + \text{V}_\text{Ti}$), nitrogen doped at Ti-site with O vacancy ($\text{N}_\text{Ti} + \text{V}_\text{O}$) and nitrogen doped at O site as well as Ti Site ($\text{N}_\text{O} + \text{N}_\text{Ti}$)} are taken for calculations for complete understanding of the process. Each structure has been geometrically relaxed until the maximum value of the unbalanced inter-atomic force component (Hellman-Feynman force) is less than $0.02\text{eV}/\text{\AA}$. The spin polarized density of states has been calculated for each optimized structure in the frame work of density functional theory. The induced magnetic moment for each system has been calculated. The Brillouin zone (BZ) of the super cells has been divided by $3\times 3\times 3$ Monkhorst-Pack (MP) k-points [125]. In all calculations, 400 eV mesh cut-off energy has been taken into account to expand the plane wave basis set, and 10^{-5} eV tolerance has been fixed as stopping criteria of the self-consistent loop to reach the electronic ground state. The spin-spin interactions study has been done by doping two dopants at two different positions, one in the same unit cell and other at the adjacent unit cell. The ground state free energy of both ferromagnetic state and anti-ferromagnetic state

has been calculated and compared to know the stability of ordered state in all the $\text{Ti}_{24}\text{X}_2\text{O}_{46}$ cases. The ferromagnetic ordering has been achieved by aligning all the spins in one direction and G-type anti-ferromagnetic ground states have been considered to study the anti-parallel ordering. Local magnetic density (LMD) distribution has been calculated for spin polarized configuration. The simulations of energy loss and penetration depth for different ions irradiation has been carried out using SRIM software [126].

3.3 Experimental details

Rutile- TiO_2 (Alfa Aesar, Johnson Mathey, Germany) polycrystalline powder 99.998% pure has been pelletized in the form of thick pallets (~0.5 mm - 0.7 mm) with high palletizing pressure (~220 MPa). The pallets were then annealed at high temperature (450 °C - 700 °C at different sittings) for 5 hours before irradiation. Irradiation experiment involving 96 MeV of 16 O^{8+} ions from IUAC 15 UD pelletron was carried out in the Materials Science Beamline of IUAC. The irradiation fluence is 6×10^{13} ions/cm². The beam has been scanned uniformly on 1 cm × 1 cm area of the sample. For another set of samples, 1.2 MeV C^{4+} , 50 keV N^{4+} and 10 keV B^+ ion beam produced from electron cyclotron resonance (ECR- 6.4 GHz) ion source of the radioactive ion beam facility, VECC, Kolkata has been irradiated uniformly over the surface of polycrystalline pallet at a fluence of 1×10^{16} ions/cm². The irradiation process is carried out with a beam current of the order of few micro-Amperes. The vacancies defects formed due to irradiation of 96 MeV O^{8+} ions have been characterized using PAS (LT/CDB) techniques as described in chapter 1. The Doppler broadened lineshape of the electron-positron annihilation 511 keV γ - ray has been

measured using HPGe detector. The 12 % efficiency HPGe detector (Type, PGC 1216sp of DSG, Germany) have an energy resolution of 1.15 keV at 514 keV of ^{85}Sr . A $10\ \mu\text{Ci}\ ^{22}\text{NaCl}$ source encapsulated in a $1.5\ \mu\text{m}$ thin nickel foil has been used as a positron source. The magnetic measurements have been carried out using Quantum Design make SQUIDs magnetometer.

3.4 Ferromagnetism in p-block elements doped TiO_2

Different p-block elements e.g., B, Al, C, Si, N, P, and As have been subsequently substituted in rutile TiO_2 both at the oxygen site and Titanium site. The elements have been doped at two different positions at the oxygen site in TiO_2 , maintaining the distance between the two substitutional atom (X_{O}) different, one is short position (1, 2) and the other is long position (1, 3) as shown in **Figure 3.1**.

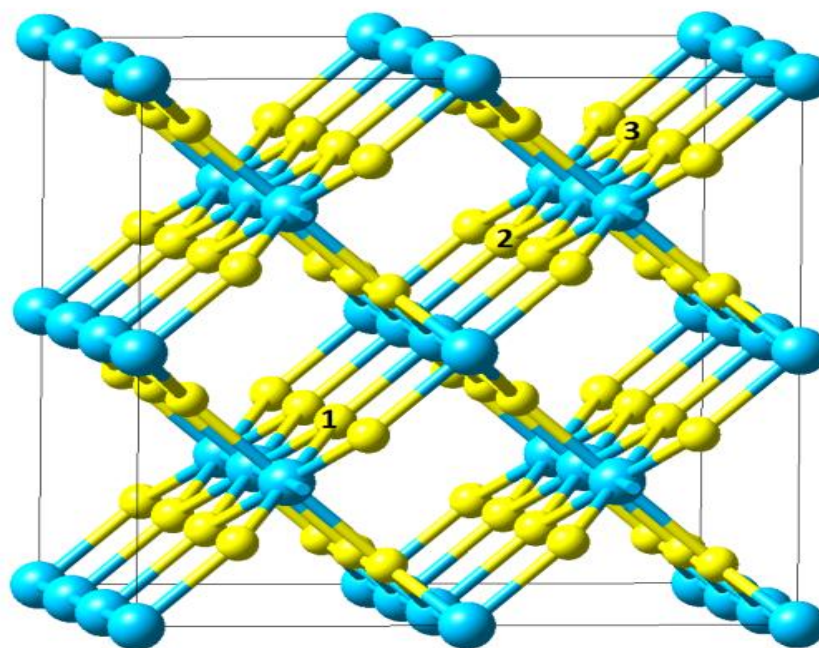


Figure 3.1 Carbon atom doped in short position (1, 2) and in long position (1, 3) in the 72 atom super cell of TiO_2 .

Substitution of any one of the p-block elements in the Ti site of rutile TiO₂ results zero magnetic moment. The induced magnetic moment (μ_B) of (Ti₁₂O₂₃X)₂ system with X = B, Al, C, Si, N, P, As; also for atomic vacancies V_{Ti} and V_O has been plotted in **Figure 3.2**. Table 3.1 represents all the structure optimized parameter e.g., the optimized distance between the two doping site, total energy, induced magnetic moment and the defect formation energy E_{df} . The defect formation energy for doping of different ‘X’ (X= p block elements) in rutile TiO₂ has been calculated using equation (12) [80-127].

$$E_{df}(X) = E(\text{Ti}_{12}\text{O}_{23}\text{X})_2 - E(\text{Ti}_{12}\text{O}_{24})_2 - 2E(\text{X}) + 2E(\text{O}) \dots\dots\dots (12)$$

where, $E_{df}(X)$ is the defect formation energy corresponding to doping of X (X= B, Al, C, Si, N, P, As), $E(\text{Ti}_{12}\text{O}_{23}\text{X})_2$ and $E(\text{Ti}_{12}\text{O}_{24})_2$ are the total energy for X_O doped TiO₂ and pristine TiO₂ respectively; also $E(X)$ and $E(O)$ are the total energy corresponding to single doped atom and oxygen atom respectively.

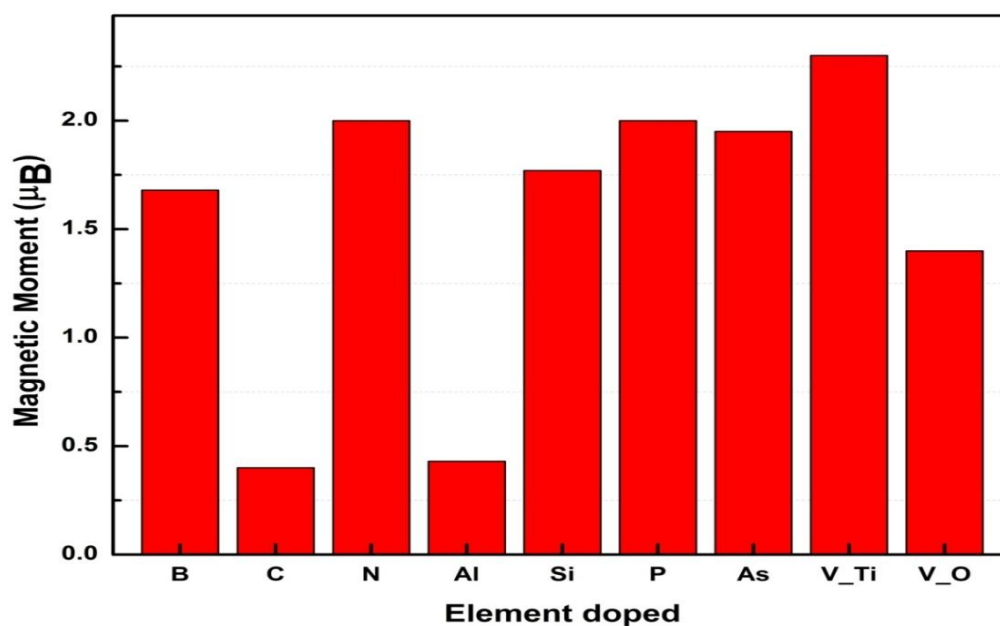


Figure 3.2 Induced magnetic moment of (Ti₁₂XO₂₃)₂ (X = B, C, N, Al, Si, P and As) system and TiO₂ system with single V_{Ti} and V_O.

Table 3.1 Total energy, defect formation energy (E_{df}) and induced magnetic moment for different elements doped at oxygen site (X_O) of rutile TiO_2 .

Name of the Element Doped	Distance between two doped atoms (in Å)	Effective magnetic moment (μ_B)	Total energy after doping * FM, # AFM.	Defect Formation Energy (E_{df}) *FM, # AFM.	ΔE = (E_{AFM} - E_{FM}) (meV)	Stable State (AFM/FM)
Boron	7.24	1.677	-634.551*	9.222*	-1	FM
			-634.550 #	9.223 #		
Aluminum	8.35	0.43	-629.078*	14.747 *	0	Both
			-629.078 #	14.747 #		
Carbon	4.84	0.4	-635.311*	8.635 *	-88	FM
			-635.223 #	8.723 #		
	7.24	0.007	-635.311 *	8.64 *	-148	FM
			-635.163 #	8.78 #		
Silicon	8.32	1.77	-631.376 *	12.583 *	-3	FM
			-631.373 #	12.586 #		
Nitrogen	7.14	2.0	-640.617 *	3.367 *	-1	FM
			-640.616 #	3.368 #		
	3.53	1.95	-640.612*	3.372*	27	AFM
			-640.639 #	3.344 #		
Phosphorus	7.32	2.0	-628.790 *	15.215 *	-1	FM
			-628.789 #	15.216 #		
	4.77	1.74	-629.256 *	14.749 *	72	AFM
			-629.328 #	14.677 #		
Arsenic	7.33	1.95	-625.717 *	18.243 *	2	AFM
			-625.719 #	18.241 #		

From Table 3.1 it is clear that due to doping of different p-block element in the same oxygen site of TiO_2 the distance between the two doping site does not remain constant rather there is significant amount of structural deformation which is due to the size of the doped element. The optimized long distance between the two $B_O - B_O$ is 7.24 Å, whereas it is 8.35 Å for $Al_O - Al_O$. Similar results have been observed in case of short distance doping. In case of Boron doped at oxygen site (B_O) and Aluminum doped at oxygen site (Al_O) magnetic moment arises due to the unpaired

electron (3d orbital electron) of Titanium. In the periodic table Al (valence electronic configurations of $3s^23p^1$) is just below B (valence electronic configurations of $2s^22p^1$) but the magnetic moment induced for B_O is $1.68 \mu_B$ while for Al_O is $0.48\mu_B$. Similar result has been observed [80] in case of ZnO with B_O and Al_O , which has been explained with the help of electronegativity of the dopants. In case of C_O (doping of carbon at oxygen site) the induced magnetic moment is $0.4 \mu_B$. Here the 2p electrons of carbon atoms are responsible for inducing magnetic moment in rutile TiO_2 . Doping of silicon atom at oxygen site induces magnetic moment of $1.77 \mu_B$, which is again due to the 3d electron of titanium atom. The much higher value of magnetic moment in case of Si_O may be due to quite large atomic sizes of the Si, similar to ZnO case [80]. The doping of group 15 elements of periodic elements e.g., N, P, As, also induces a significant magnetic moment in TiO_2 . Here the magnetic moment comes from the *p*-orbital electron of the doped element. In all the three cases the magnetic moment is $\sim 2 \mu_B$. Also, it has been seen that in TiO_2 both oxygen vacancy (V_O) and titanium vacancy (V_{Ti}) can induce magnetic moment in rutile TiO_2 . The creation of single V_{Ti} and single V_O generates a moment of $\sim 2.3 \mu_B$ and $\sim 1.4 \mu_B$ respectively. To investigate the interaction between the magnetic moments, the calculations with two magnetization configurations, i.e., ferromagnetic (FM) and anti-ferromagnetic (AFM) states for all p-block element doped TiO_2 systems has been done. Two different distances between the two defect sites ($X_O - X_O$) have been chosen for the above purpose.

The atomic positions in both FM and AFM cases have been fully optimized and the total energy has been computed. The optimized long and short distances along with other parameter has been listed in Table 3.1. It is interesting to note that the induced

magnetic moments also depend on the distances between the two defect sites in the TiO_2 . For long distances, the magnetic moment induced by B_O , Al_O , C_O , Si_O , N_O , P_O and As_O are $1.68 \mu_\text{B}$, $0.43 \mu_\text{B}$, $0.007 \mu_\text{B}$, $1.77 \mu_\text{B}$, $2 \mu_\text{B}$, $2 \mu_\text{B}$ and $1.95 \mu_\text{B}$ respectively. It can be seen from the Table 3.1 that the defect formation energy for spin parallel state and spin anti-parallel state for all the above system unless C_O is within +2 and -3 meV. This indicates that spin-spin interaction has very little effect on this defect length. The spin polarized total density of states (DOS) for all p-block element doped TiO_2 system have been compared in **Figure 3.3**.

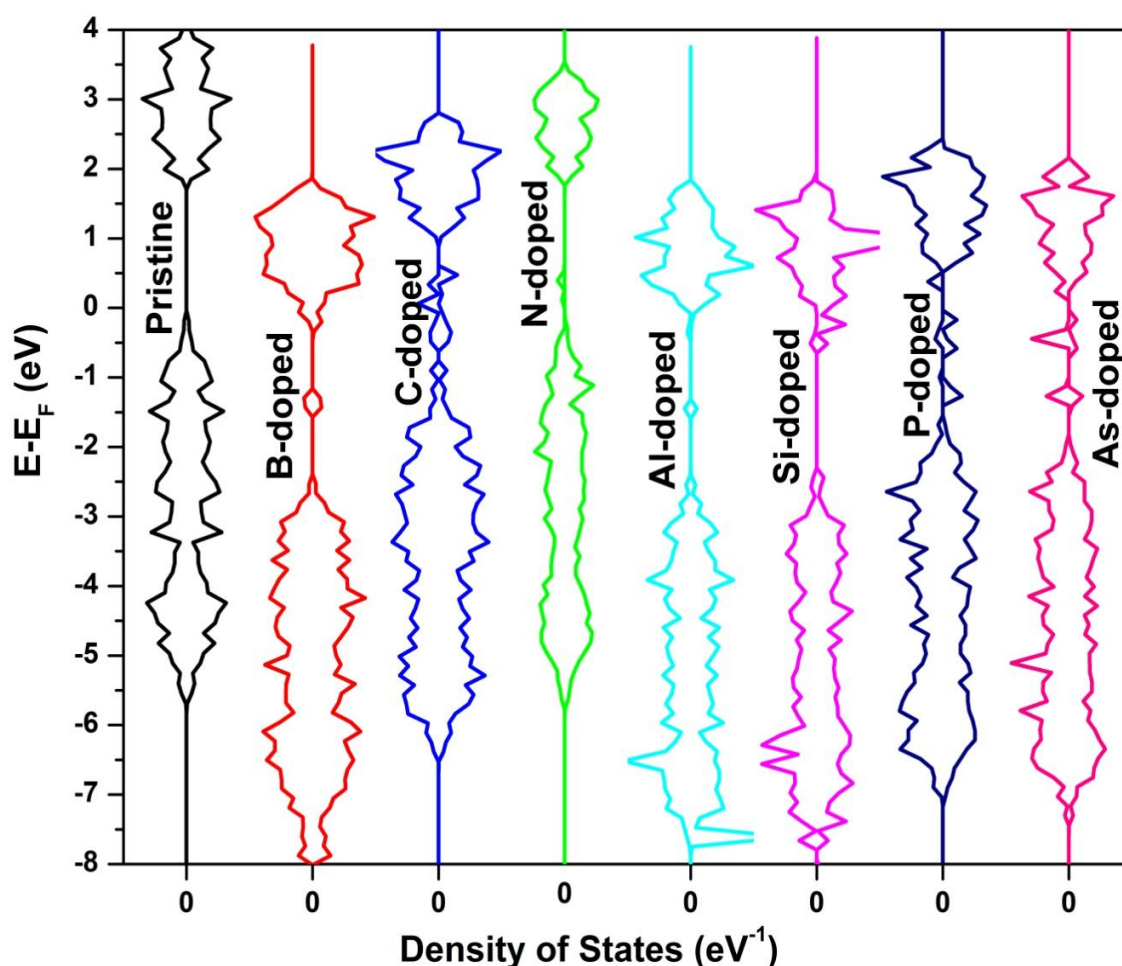


Figure 3.3 Comparison of total density of states for pristine TiO_2 and different p-block elements (B, C, N, Al, Si, P and As) doped TiO_2 system.

The total DOS is symmetric for pristine TiO_2 system, which indicates an equal number of up spin electronic states and down spin electronic states. As a result, TiO_2 system is perfectly diamagnetic and shows no magnetic moment in its pristine form. However, it is clear from **Figure 3.3** that the doping of p-block element brings asymmetry in total DOS of TiO_2 , which results in the generation of an effective magnetic moment in the system. Similarly, in the short distances ($\sim 5\text{\AA}$), only C_O , N_O and P_O induces magnetic moment. No significant magnetic moment has been generated in other substitution. But in this length regime a strong spin-spin interaction has been observed. Anti-parallel spin state is favored in case of N_O and P_O while in case of C_O the ground state free energy of ferromagnetic (spin parallel) state is about 88 meV less than the corresponding anti-ferromagnetic state.

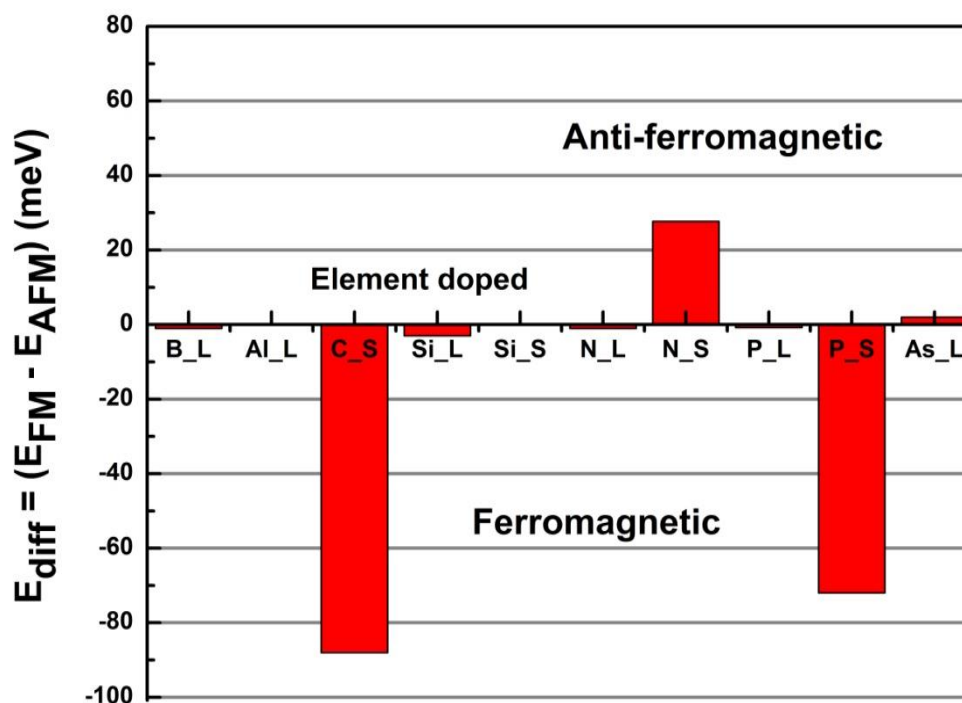


Figure 3.4 The energy difference between ferromagnetic and anti-ferromagnetic state for different p block element doped (at oxygen site) TiO_2 system.

The present *ab-initio* calculation reveals that doping of carbon atom at oxygen site gives a stable ferromagnetic state, which is in agreement with the results obtained by earlier theoretical calculations [86]. **Figure 3.4** shows the energy difference between ferromagnetic state and anti-ferromagnetic state for all p-block element doped TiO₂. It is clear from the **Figure 3.4** that doping of boron, carbon and nitrogen in TiO₂ favors ferromagnetic coupling. Explicit studies for the effect of doping of boron, carbon and nitrogen in TiO₂ have been presented in the following sections.

3.5 Room temperature ferromagnetism in oxygen irradiated TiO₂

The energy loss profile for the 96 MeV oxygen ion beam in TiO₂ has been simulated in SRIM software [126] as shown in **Figure 3.5**. The maximum penetration depth of oxygen ions is found to be $\sim 65 \mu\text{m}$ (as shown in inset of **Figure 3.5**). The maximum nuclear energy loss of the O ion is $27 \text{ eV}/\text{\AA}$. So, only scattered point defects of both oxygen vacancies (V_{O}) and Ti vacancies (V_{Ti}) are expected. A part of such generated defects will form pairs/complexes in the material; however, such events cannot be estimated by SRIM. The implantation depth, (x) of positron from the radioactive source ^{22}Na is given by $P(x) = \eta \exp(-\eta x)$. $1/\eta$ is the characteristic penetration depth of a positron with specific energy (E). One can calculate $1/\eta$ which is approximately $(E_{\text{max}})^{1.4}/16\rho$ in μm , if E is expressed in MeV and ρ is the density of the material in g/cm^3 . E_{max} is the maximum energy of the emitted positrons, e.g., for ^{22}Na , E_{max} is $\sim 0.54 \text{ MeV}$. In TiO₂ with density $4.26 \text{ g}/\text{cm}^3$, $1/\eta$ comes out to be $\sim 58 \mu\text{m}$. Thus in the present irradiated TiO₂ sample, almost all the positrons have been annihilated in the radiation damaged region.

It is interesting that after irradiation the colour of the sample remain same (white) and the surface resistance increases from $1 \times 10^7 \Omega \text{ cm}^{-2}$ to $2 \times 10^7 \Omega \text{ cm}^{-2}$. Using density functional theoretical calculations, the band structure in the titanium vacancy (**Figure 3.6**) induced TiO_2 has been shown to be p-type material, as the Fermi level shifts towards the valence band compared to the band structure of pristine system as shown in **Figure 3.7**. Similarly, the oxygen vacancy causes an upward shift of the Fermi level (**Figure 3.8**) and is considered to be effectively n-type material. This is due to the contribution of unbound 3d electrons of Ti atoms near the oxygen vacancy site. In the present case, sheet resistance increases due to irradiation, which favors formation of more V_{Ti} s due to irradiation in TiO_2 . **Figure 3.9** shows the M vs H curve, at room temperature, for the oxygen irradiated rutile TiO_2 . It clearly indicates the ferromagnetic nature with a saturation magnetization of 0.132 emu g^{-1} and coercive field of 226 Oe. It is clear that due to irradiation of 96 MeV oxygen ion beam, a huge number of vacancy type defects have been generated in the TiO_2 samples, which makes the sample ferromagnetic even at room temperature, this is again in agreement with our earlier observation [88].

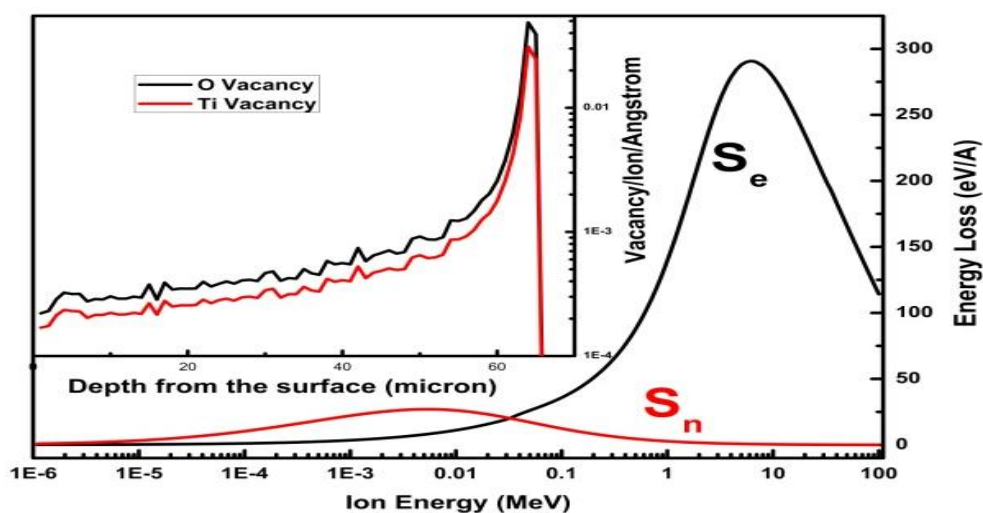


Figure 3.5 Energy loss and defect profile for 96 MeV oxygen on TiO_2 sample as simulated by SRIM/TRIM software.

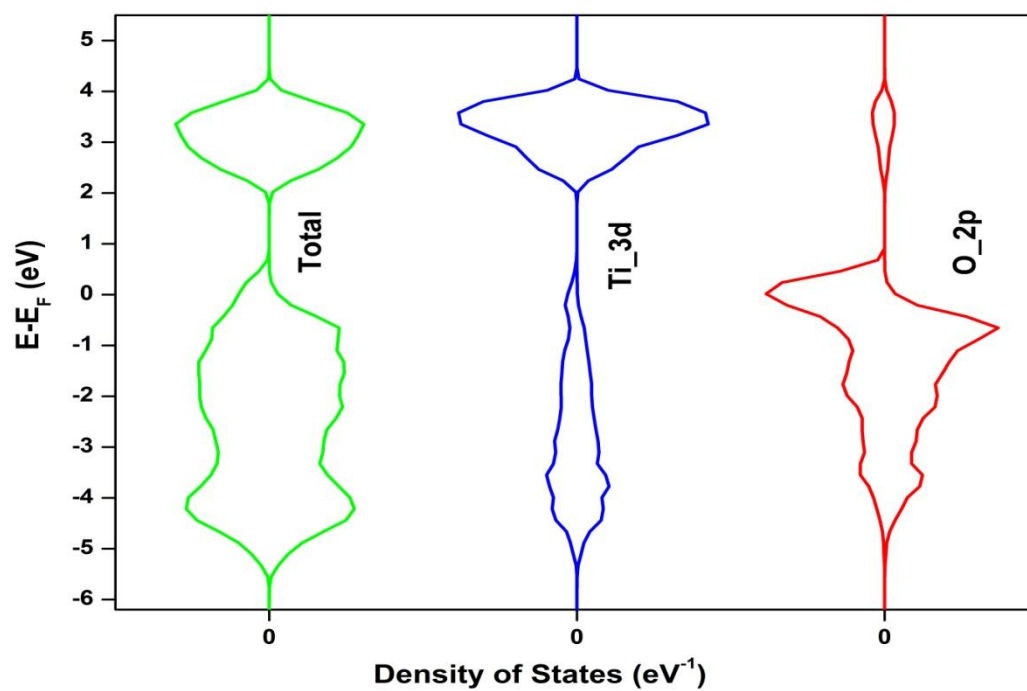


Figure 3.6 Spin polarized density of states for TiO_2 with V_{Ti} ($\text{Ti}_{23}\text{O}_{48}$).

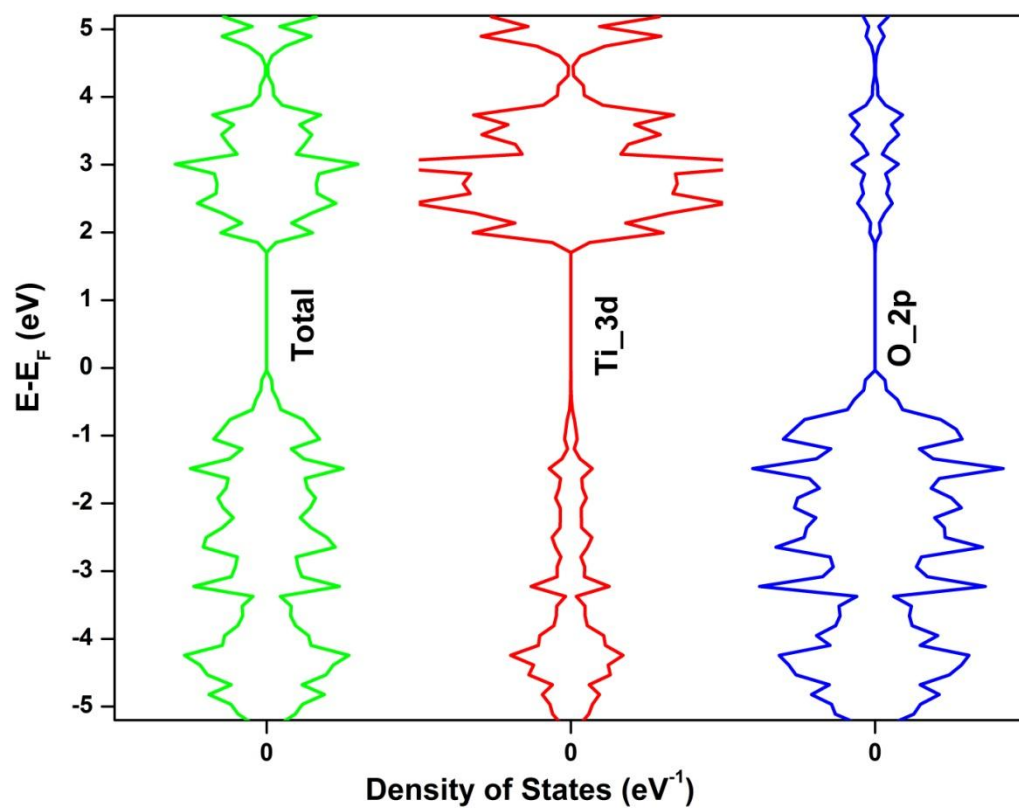


Figure 3.7 Spin polarized density of states for TiO_2 pristine.

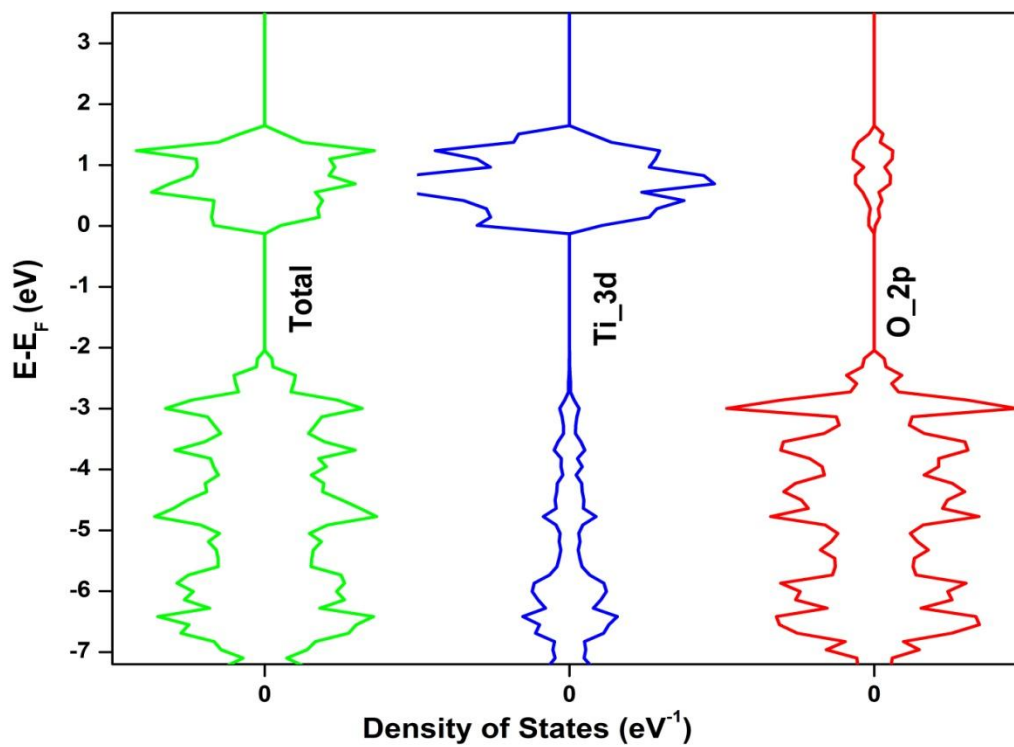


Figure 3.8 Spin polarized density of states for TiO_2 with V_O ($\text{Ti}_{24}\text{O}_{47}$).

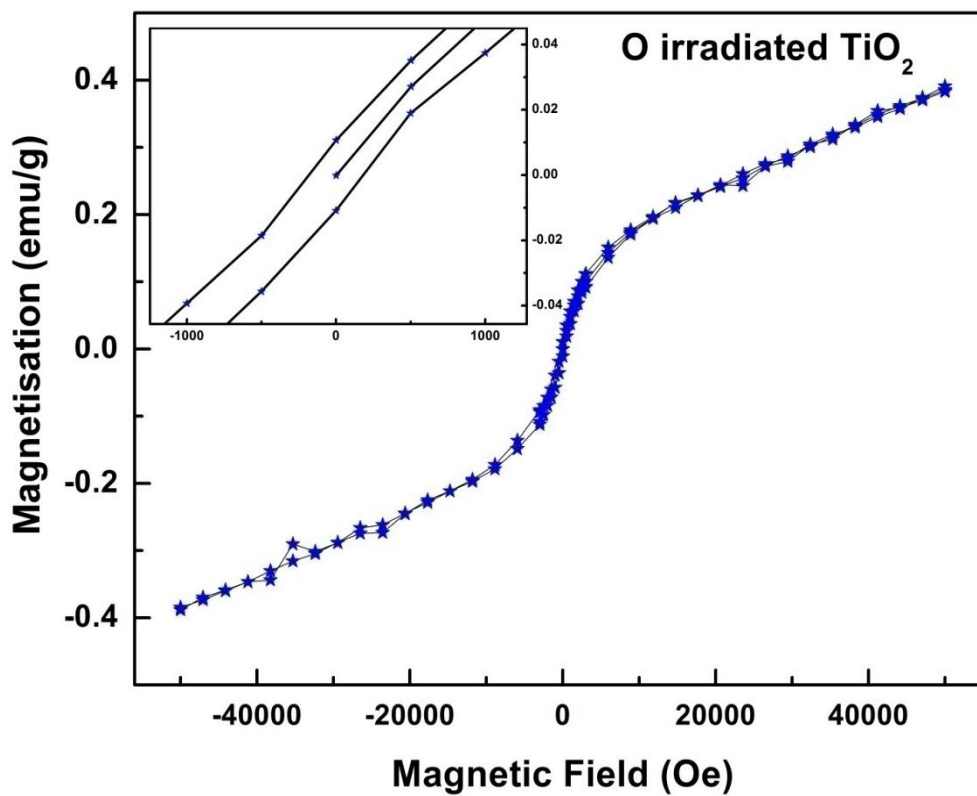


Figure 3.9 Magnetization vs applied field curve obtained from SQUID for 96 MeV oxygen irradiated TiO_2 sample.

To identify the defects which are generated by the irradiation of energetic ion beam, positron annihilation spectroscopy has been employed. The positron annihilation lifetime spectrum for the oxygen irradiated polycrystalline TiO_2 samples has been recorded as shown in **Figure 3.10**. Similar lifetime measurements have been performed for pristine and un-irradiated polycrystalline TiO_2 samples. The measured positron annihilation lifetime spectrum for all the samples has been evaluated by a computer programme PATFIT 88 [127] with proper source corrections. For both the spectra, best fit (variance of fit < 1 per channel) has been obtained with three component fitting. The short lifetime component has been assigned to the free annihilation of positrons in the bulk of the sample, while the intermediate lifetime component is due to the annihilation of positron in the defect site (mainly Ti vacancies). The long lifetime component (τ_3) originates from the formation of positronium at the sample surface or at the large voids inside the sample. All the lifetime components have been listed in Table 3.2.

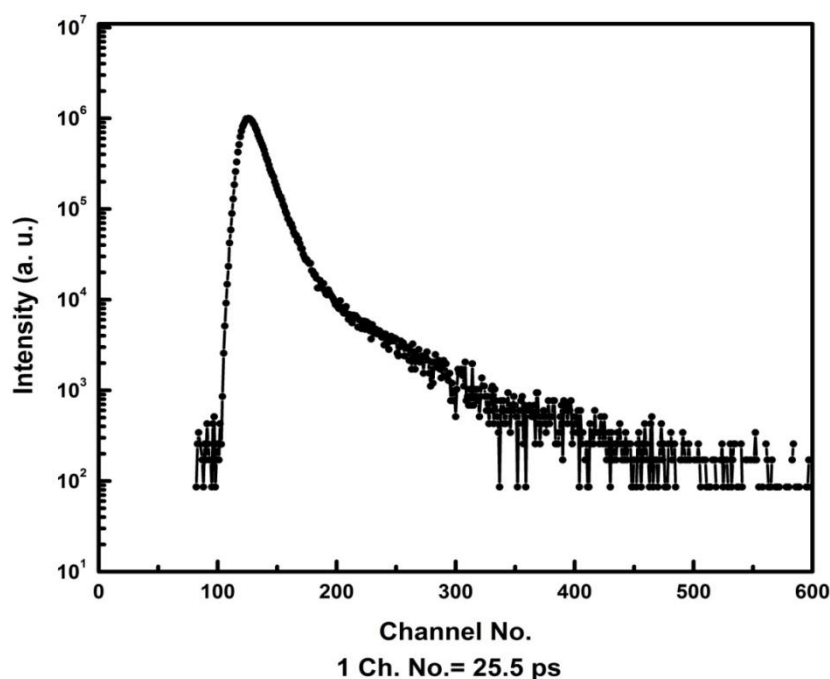


Figure 3.10 Positron annihilation lifetime spectra for oxygen irradiated rutile TiO_2 .

Table 3.2 Different positron lifetime parameters for un-irradiated and oxygen irradiated TiO₂ samples.

Sample	τ_1 (ps)	I ₁ (%)	τ_2 (ps)	I ₂ (%)	τ_3 (ps)	I ₃ (%)
TiO ₂ (SXL) Un-irradiated	183 ± 3	96 ± 0.1	--	--	1300 ± 9	4 ± 0.1
TiO ₂ polycrystalline Unirradiated	182 ± 3	63 ± 3	386 ± 9	35 ± 3	1791 ± 90	2 ± 0.1
TiO ₂ polycrystalline Oxygen Irradiated	176 ± 8	44 ± 3	366 ± 9	53 ± 3	1854 ± 55	3 ± 0.1

For single crystal sample, the intensity of τ_1 is 96 % and τ_2 is 0%. The value of τ_1 for the un-irradiated sample is 182 ps, which is very close to the bulk lifetime of positron, 178 ps for TiO₂ [129-130]. The theoretically estimated positron lifetime in TiO₂ is also in close agreement with the present data [131]. The intermediate positron lifetime (~ 366 ps) is due to the annihilation of positrons in V_{Ti} or V_{Ti}-V_O vacancy clusters. The intensity of the intermediate positron lifetime component (I₂) increases from 35 % to 53 % due to irradiation of 96 MeV oxygen ions, which clearly suggest the formation of Ti vacancy type defect in the TiO₂. For further confirmation, coincidence Doppler broadening of positron annihilation lifetime spectroscopy has been employed. **Figure 3.11** shows the ratio between the area normalized coincidence Doppler broadening spectra of un-irradiated and 96 MeV oxygen irradiated TiO₂ sample with the reference area normalized CDB spectra of 99.9999 % pure Al single crystal. It is clear from **Figure 3.11** that in the irradiated TiO₂ sample, positrons are less annihilating with the core electrons of Ti. The lesser number of annihilating photons in the region above $p_L \sim 10 \times 10^{-3} m_0c$ to $p_L \sim 18 \times 10^{-3} m_0c$ indicates that a significant fraction of positron annihilation in the open volume defects in the form of

oxygen and Ti-vacancies. One can identify two prominent dip like features at $p_L \sim 11 \times 10^{-3} m_0c$ and $p_L \sim 16 \times 10^{-3} m_0c$ which indicates that there are more Ti-vacancies. **Figure 3.12** represents the ratio between the area normalized coincidence Doppler broadening spectra of 96 MeV oxygen irradiated TiO_2 with that of un-irradiated TiO_2 . The ratio curve indicate a broad dip in the momentum range 5×10^{-3} to $22 \times 10^{-3} m_0c$ with two dips; one at $11 \times 10^{-3} m_0c$ and the other is at $16 \times 10^{-3} m_0c$. Using the relation $\varepsilon = p_L^2 / 2m_0$ the energy of the electron (with which positrons are annihilating) coming out to be ~ 31 eV and ~ 65 eV. This clearly suggests that positrons are less annihilating with the 3p (32.6 eV) and 3s (58.7 eV) electrons of Ti. Thus from the above measurement it is re-confirmed that a large number of titanium vacancy (V_{Ti}) has been generated due to 96 MeV oxygen ion irradiation.

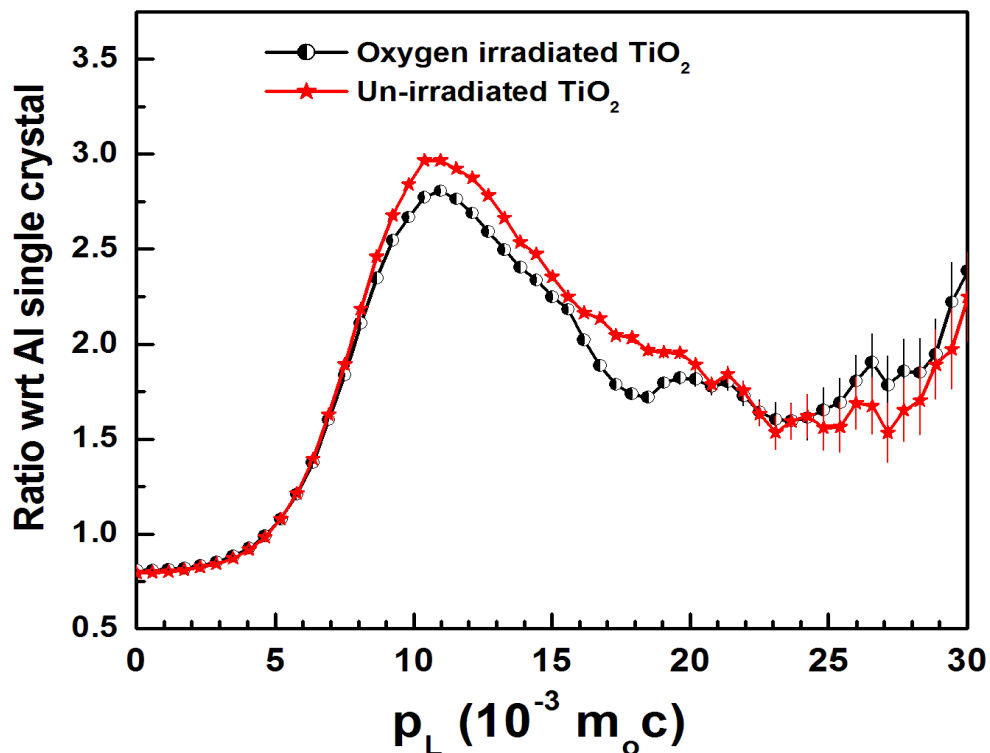


Figure 3.11 Ratio curve constructed from the CDB spectrum for un-irradiated and irradiated TiO_2 with respect to the CDB spectra of 99.9999 % pure Al single crystal.

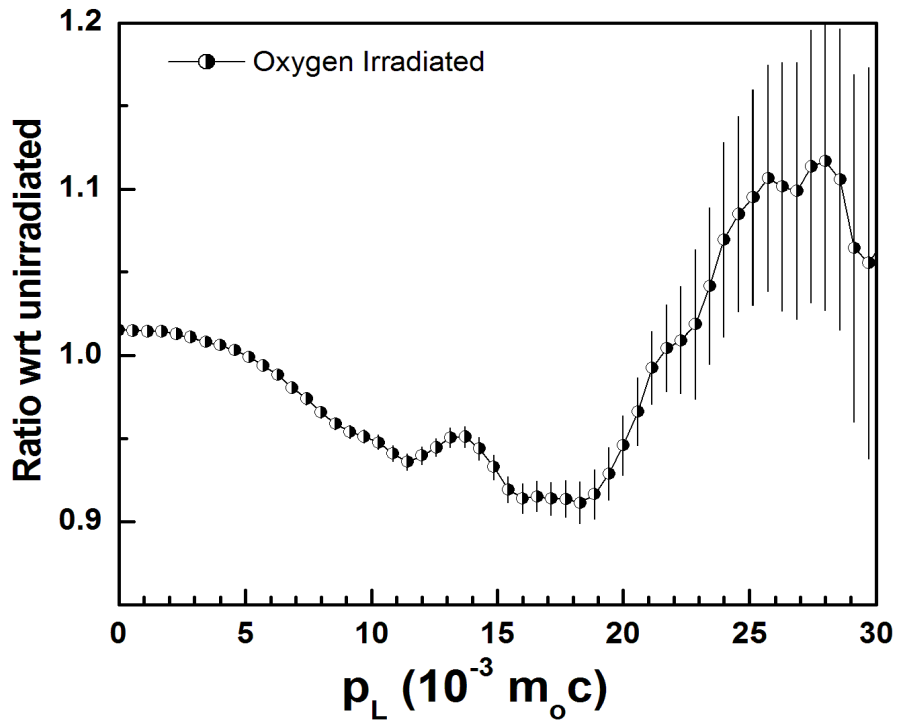


Figure 3.12 Ratio curve constructed from the coincidence Doppler broadening spectrum for irradiated TiO_2 with respect to the same for pristine sample.

The defect induced room temperature ferromagnetism in rutile TiO_2 has been theoretically understood by using *ab-initio* density functional theory. It has been already discussed in previous section (i.e., section 3.4.1) that both oxygen vacancy (V_{O}) as well as titanium vacancy (V_{Ti}) induces magnetic ordering in TiO_2 . The defect formation energy is large (~ 20.5 eV) for V_{Ti} compared to V_{O} (~ 8.5 eV), and the induced magnetic moment are $\sim 2.2 \mu_{\text{B}}$ and $1.4 \mu_{\text{B}}$ respectively. In TiO_2 the formation possibility of V_{O} is larger than the V_{Ti} , but in the present case 96 MeV oxygen ions have been used to create a significant amount of V_{Ti} in TiO_2 . The spin polarized density of states of TiO_2 with V_{Ti} , pristine TiO_2 and TiO_2 with V_{O} has been shown in **Figure 3.6**, **Figure 3.7** and **Figure 3.8** respectively. It can be seen that unlike pristine system, the spin polarized density of states is asymmetric for both V_{Ti} and V_{O} system. The asymmetry in total DOS in case of V_{Ti} comes from the contribution of 2p-orbital

electrons oxygen in the system. As a result, 2p-orbital electrons of neighboring oxygen atoms are mainly responsible for magnetization. Also, 3d-electrons of the neighboring Ti atoms contribute a small fraction. Whereas, in case of V_O the 3d-orbital electrons of nearby Ti atoms are responsible for induced magnetic moment in the TiO_2 system. **Figure 3.13** shows the spin polarized localized magnetic density around Ti vacancy (mainly due to oxygen 2p electron) as simulated by density functional theory. The local magnetic density simulations depicts that the magnetization is localized around the oxygen atoms surrounding V_{Ti} in the rutile TiO_2 system.

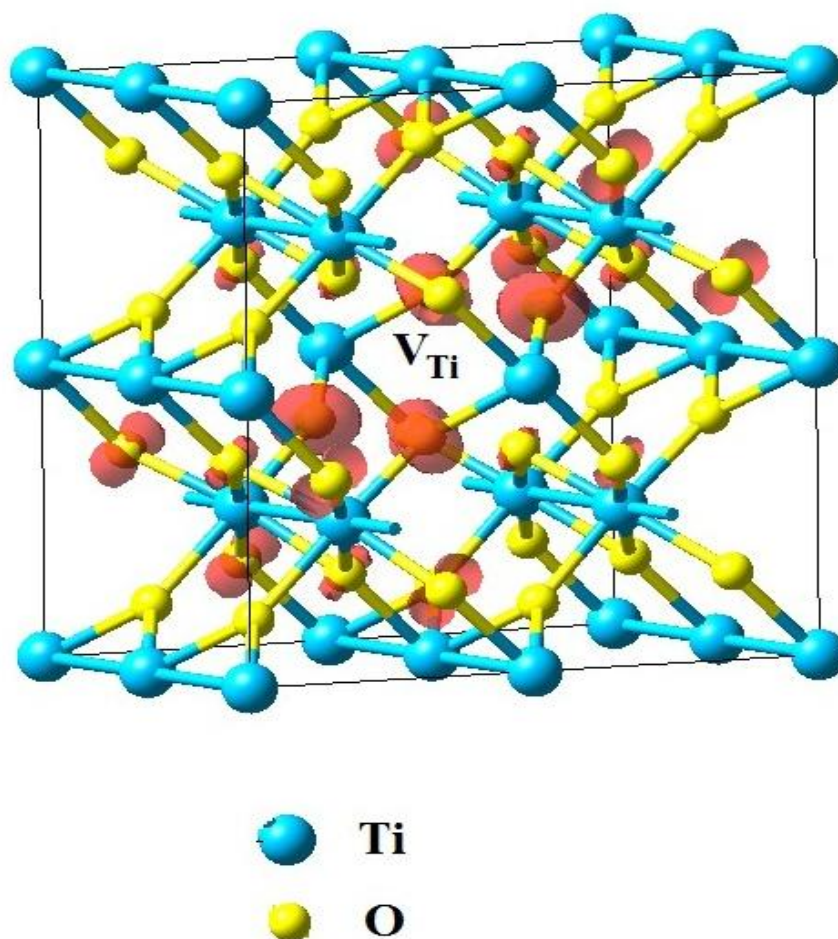


Figure 3.13 Magnetization density (spin polarized) of TiO_2 with V_{Ti} .

3.6 Room temperature ferromagnetism in carbon doped TiO₂

Ferromagnetic properties of carbon doped TiO₂ system have been explicitly studied by considering different atomic vacancies along with doping of carbon atom in the lattice. The doping of carbon atom at oxygen site generates a significant amount of magnetic moment in the system. Carbon atom ($1s^2 2s^2 2p^2$) when doped at O-site gets two electrons from nearby Ti-atoms and becomes $2s^2 2p^4$ in the valence shell. As a result, C-atom contributes $\sim 2\mu_B$ magnetic moment in the TiO₂ system. The oxygen atoms present in the neighboring site make a small contribution in net magnetization due to the effect of polarization. Presence of different vacancies inside the system greatly influences the generation of magnetic moment in TiO₂. The magnetic moment induced in TiO₂ system with different configurations is shown in **Figure 3.14**.

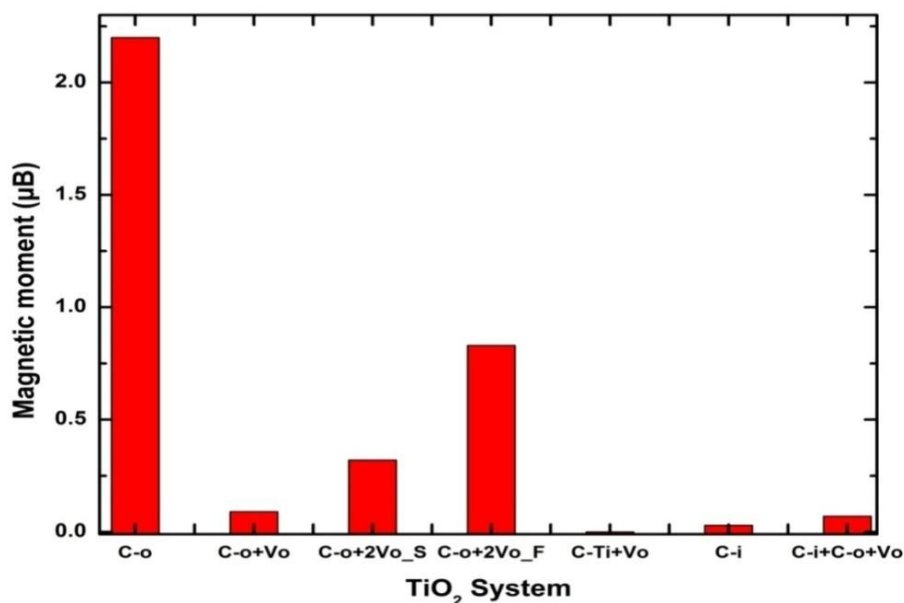


Figure 3.14 Induced magnetic moment for carbon doped TiO₂ system with different configuration.

Doping of one carbon atom at oxygen site generates about $2.2\mu_B$ magnetic moment. The magnetic moment generated in the carbon doped rutile TiO₂ system favors spin parallel alignment [81]. The 2p-orbital electrons of doped carbon atom are the primary

source of magnetism, a small contribution of magnetic moment comes from neighboring oxygen atoms. Presence of one oxygen vacancy attached to carbon atom reduces the moment significantly (as in case of $C_{O+} V_O$). In case of $C_{O+} 2V_{O_S}$, one more oxygen vacancy is created near the carbon atom slightly increases the total moment in the system. The increase comes from the contribution of 3d-orbital electrons of Ti atoms surrounding vacancies. Change in the position in 2nd oxygen vacancy in the TiO_2 matrix ($C_{O+} 2V_{O_F}$) further increases the moment in the system. This extra contribution comes from the effect of single oxygen vacancy in the system. The creation of oxygen vacancy induces a significant magnetism in TiO_2 [88]. The magnetic moment generated due to substitution of carbon at oxygen site is enhanced with the presence of oxygen vacancy, as magnetic moment generated from both the cases gets added up in the system. Doping of carbon atom at titanium site does not induce any magnetic moment in the system. Removal of oxygen atom attached to C-atom doped at Ti-site also does not contribute any moment in the system. The incorporation of nitrogen atom in the interstitial site generates a significant moment in TiO_2 [132] but C-doped at interstitial site do not show any change in magnetic moment. Also, no significant improvement has been observed for C doped at interstitial site together with other configuration ($C_i + C_{O+} V_O$) in the TiO_2 system.

The values of defect formation energy (E_{df}), Fermi energy and Fermi energy difference with pristine TiO_2 have been shown in Table 3.3. The formula represented by equations (13) [80,127] has been used to calculate the E_{df} in all the systems in rutile TiO_2 .

$$E_{df} = E(Ti_{24-m} C_{m+n} O_{48-n}) - E(Ti_{12} O_{24})_2 + nE(O) + mE(Ti) - (m+n)E(C) \dots (13)$$

Where $E(\text{Ti}_{24}\text{O}_{48})$ represents total energy of pristine system and $E(\text{Ti}_{24-m}\text{C}_{m+n}\text{O}_{48-n})$ is the total energy of defect bearing system. Similarly, $E(\text{O})$, $E(\text{Ti})$, and $E(\text{C})$ are the free energy value of single oxygen atom, titanium atom and carbon atom respectively. It can be noted from the Table 3.3 that defect formation energy for TiO_2 with carbon doped at O-site is only ~ 4 eV which makes the system feasible. The carbon atom can easily occupy in the already present oxygen vacancies.

Table 3.3 Defect formation energy, Induced magnetic moment, Fermi energy and Fermi energy shift for carbon doped at oxygen site with different configurations in TiO_2

TiO₂ System	Defect Formation Energy (eV)	Induced Magnetic Moment (μ_B)	Fermi Energy (eV)	Fermi Energy shift (eV)
$\text{C}_\text{O} (\text{Ti}_{24}\text{CO}_{47})$	4.04	2.27	5.78	2.35
$\text{C}_\text{O} + \text{V}_\text{O} (\text{Ti}_{23}\text{NO}_{46})$	11.14	0.09	5.41	1.98
$\text{C}_\text{Ti} + \text{V}_\text{O} (\text{Ti}_{23}\text{CO}_{47})$	14.47	0.00	5.19	1.76
$\text{C}_\text{i} (\text{Ti}_{24}\text{CO}_{48})$	-4.13	0.03	7.12	3.69
$\text{C}_\text{O} + 2\text{V}_\text{O_N} (\text{Ti}_{24}\text{CO}_{45})$	20.53	0.32	6.87	3.44
$\text{C}_\text{O} + 2\text{V}_\text{O_F} (\text{Ti}_{24}\text{CO}_{45})$	20.86	0.83	6.88	3.45
$\text{C}_\text{i} + \text{C}_\text{O} + \text{V}_\text{O} (\text{Ti}_{24}\text{C}_2\text{O}_{46})$	5.92	0.07	7.04	3.62

The spin polarized density of carbon doped TiO_2 at interstitial site and carbon doped TiO_2 at oxygen site has been shown in **Figure 3.15** and **Figure 3.16** respectively. The spin polarized density of states for pristine TiO_2 has symmetric behavior (as shown in **Figure 3.7** above) as a result it is perfectly diamagnetic in nature. But, the total density of states for carbon doped TiO_2 has asymmetric behavior. The asymmetry comes from 2p orbital of carbon, along with 3d-orbital of Ti-atom and

2p-orbital of O-atom. The asymmetry in density of states ensures the presence of unpaired electrons in the system. The unpaired electrons give rise to magnetic moment in the system. Similarly, in case of TiO_2 with carbon atom at interstitial site, 2p orbital of carbon has asymmetric density of states but it has very little effect in the total density of states and yields no net magnetism in the system.

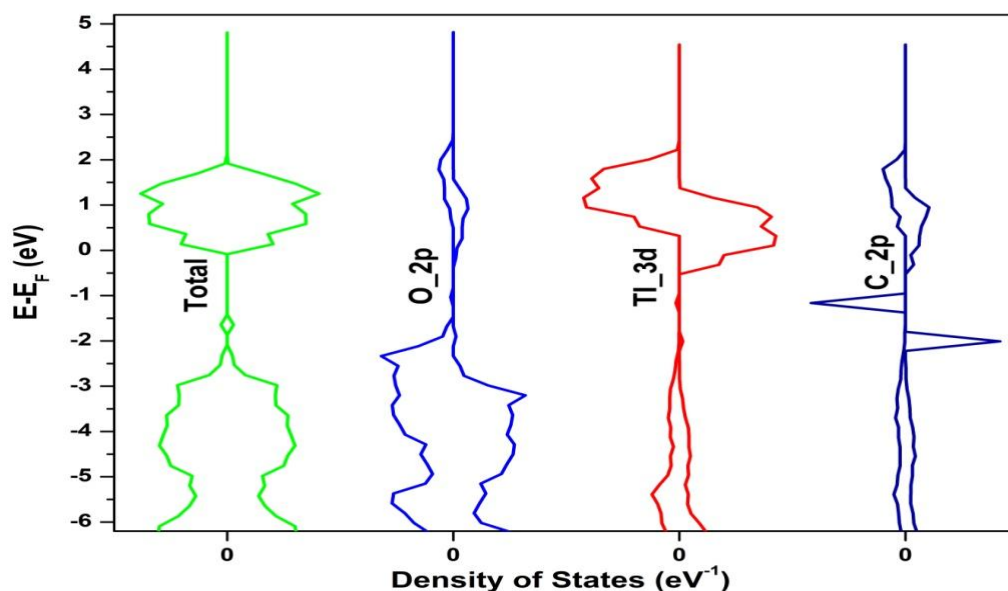


Figure 3.15 Spin polarized density of states for TiO_2 with C_i .

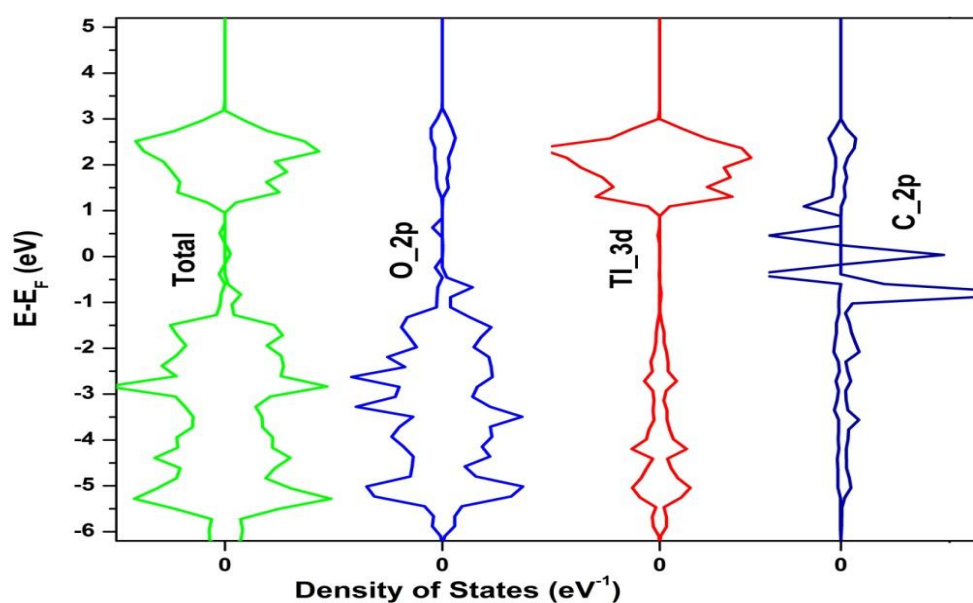


Figure 3.16 Spin polarized density of states for TiO_2 with C_o .

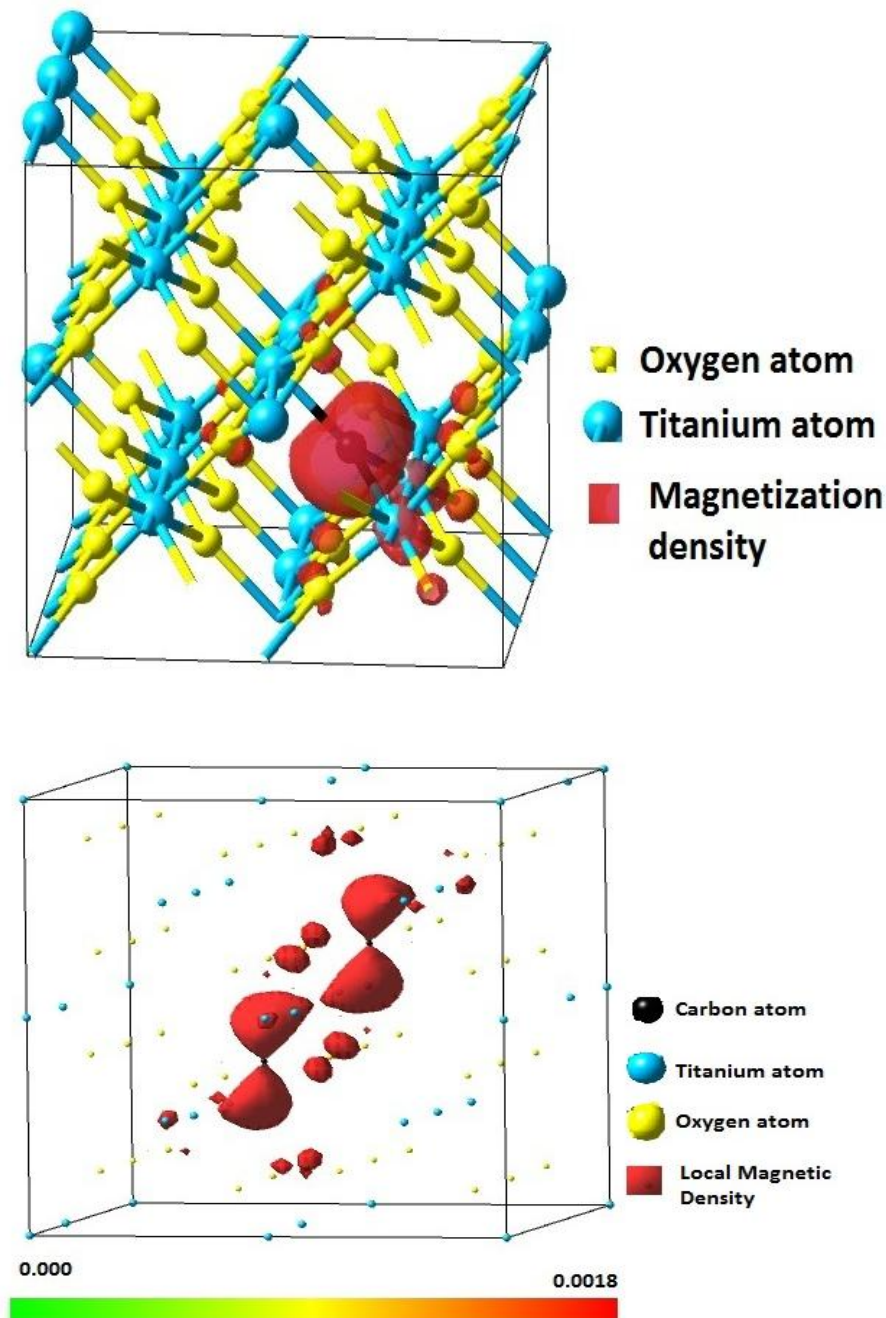


Figure 3.17 Magnetization density (spin polarized) distribution in TiO₂ with C_O. a) with one C-atom doped at o-site with atomic bonds present in **figure**, b) with two C atoms doped at O-sites and no atomic bonds in figure.

The magnetization density (spin polarized) distribution for C-doped TiO₂ has been shown in **Figure 3.17**. It can be observed that the magnetic density is mainly

localized around the dopant atom and a small fraction is present around the neighboring oxygen atoms. Thus, the result of local magnetic density distribution is in agreement with that obtained from density of states. Both calculations show the carbon atom as the source of magnetism in C-doped TiO₂ system. The doping of carbon in TiO₂ introduces some new states above valence band leading to the shift in the Fermi level in all system. This makes the carbon doped system n-type and enhances the conductivity.

Figure 3.18 (a) represents the simulated energy loss profile of carbon ions irradiated TiO₂ using SRIM. From the SRIM simulation it has been found that the nuclear energy loss is dominant up to 17 keV; whereas, the electronic energy loss (S_e) and the nuclear energy loss (S_n) at 1.2 MeV C⁴⁺ ions on TiO₂ have been found to be 131.0 eV/Å and 1.0 eV/Å respectively. Atomic vacancies in a system are generated by the nuclear energy loss mechanism of the irradiated ions [133]. As a result, fewer atomic vacancies are generated at the surface of the sample for 1.2 MeV C⁴⁺ ions and it increases with depth of the sample due to the decrease in energy of irradiated ions. This behavior was also verified utilizing TRIM and is shown in **Figure 3.18** (b). From the vacancy profile in **Figure 3.18** (b), it has been observed that both V_{Ti} and V_O have been created in TiO₂ when irradiated with 1.2 MeV C⁴⁺ ions, but the number of oxygen vacancies generated is more in comparison to titanium vacancies. **Figure 3.18** (c) depicts the distribution of carbon ions with the depth of the sample. From this figure it has been observed that the 1.2 MeV carbon ions can penetrate upto 1.78 μm and the maximum ion distribution occurs at a depth of 1.52 μm in polycrystalline TiO₂ sample. The variation of Magnetization (M) with Field (H) for the C⁴⁺ irradiated TiO₂ sample is shown in **Figure 3.19**.

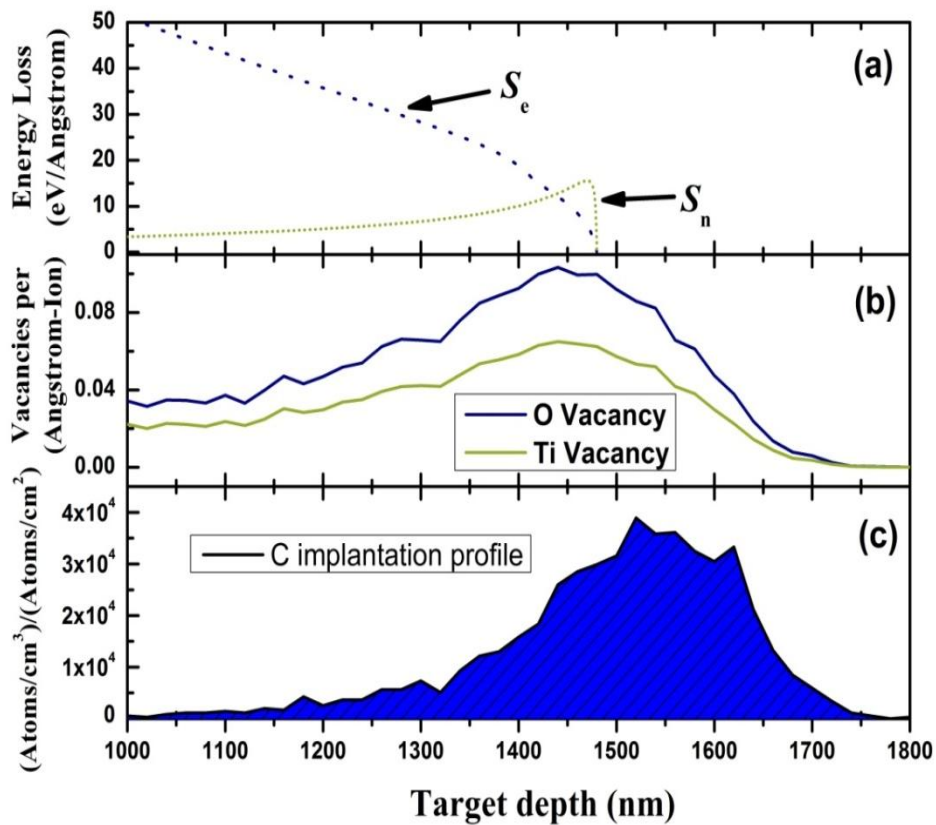


Figure 3.18 SRIM simulation for C^{4+} irradiated TiO_2 (a) energy loss profile, (b) vacancy formation profile and (c) distribution of carbon ions with target depth.

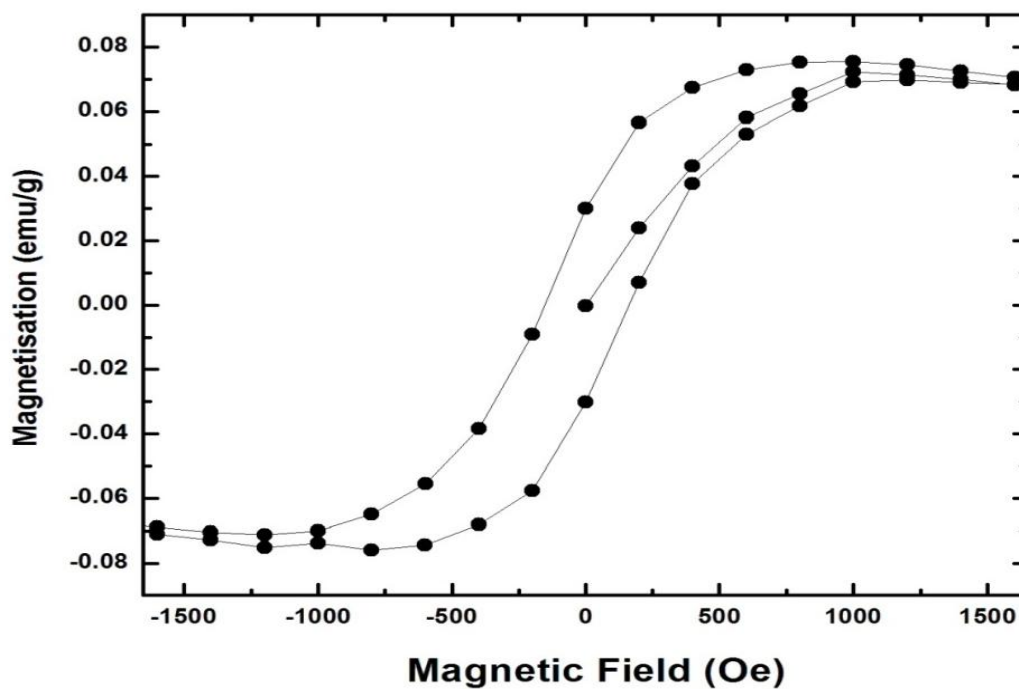


Figure 3.19 Magnetization vs field graph for 1.2 MeV carbon implanted rutile TiO_2 .

The behavior of the M vs H curve is a hysteresis loop at room temperature (~300 K). From the hysteresis curve the values of saturation magnetization (M_s) and coercive field (H_C) has been found to be 7.5×10^{-2} emu/g and 156 Oe respectively. The value of magnetization (M) is higher than the earlier reported experimental value [88] ($\sim 4 \times 10^{-4}$ emu/g), with oxygen vacancies. The higher value of saturation magnetization in C^{4+} ion irradiated rutile TiO_2 is possibly due to the contributions of magnetism from carbon atoms located at lattice site. The hysteresis curve as obtained from the present experimental data at room temperature (300 K) is a clear sign of the presence of room temperature ferromagnetism in 1.2 MeV carbon ions irradiated/implanted rutile TiO_2 .

3.7 Room temperature ferromagnetism in nitrogen doped rutile TiO_2

Ferromagnetic properties have been theoretically studied in N-doped rutile TiO_2 with the entire possible configuration. The induced magnetic moment for different nitrogen doped TiO_2 system is shown in **Figure 3.20**. Only the configuration with N_{Ti+V_O} ($N_{Ti_{23}O_{47}}$); N_O ($Ti_{24}NO_{47}$) and N_{inst} ($Ti_{24}O_{48}N$) give rise to non-zero magnetic moment in TiO_2 . All other configuration does not give rise to a net magnetic moment in the system. The nitrogen doped at oxygen site give rise to highest magnetic moment of $1.01\mu_B$ from 2p orbital electrons of N-atom along with a small contribution from 3d orbital electrons of nearest Ti atoms. The other two systems with $N_{Ti} + V_O$ ($N_{Ti_{23}O_{47}}$), and N_{inst} ($Ti_{24}O_{48}N$) give rise to $0.24\mu_B$ and $1.0\mu_B$ respectively. The primary source of magnetism in both case are 2p-orbital electrons of dopant along with 3d orbital electrons nearby Ti-atoms.

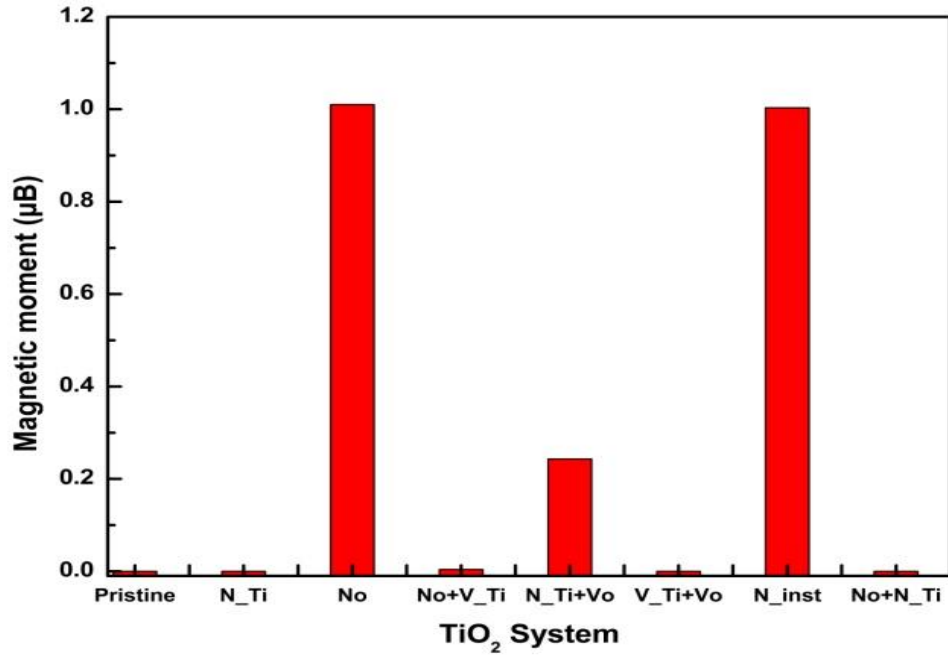


Figure 3.20 The induced magnetic moment for nitrogen doped TiO₂ system with various configurations.

The defect formation energy (E_{df}), the Fermi energy and Fermi energy difference with pristine TiO₂ in all the cases have been tabulated in Table 3.4. The E_{df} in all the systems in rutile TiO₂ has been calculated using the formula given by equations (14) [80, 127].

$$E_{df} = E(\text{Ti}_{24-m}\text{N}_{m+n}\text{O}_{48-n}) - E(\text{Ti}_{12}\text{O}_{24})_2 + nE(\text{O}) + mE(\text{Ti}) - (m+n)E(\text{N}) \quad \dots (14)$$

Where E_{df} is the defect formation energy corresponding to different TiO₂ system under study and m and n are integers which can take values 0 or 1. $\text{Ti}_{24-m}\text{N}_{m+n}\text{O}_{48-n}$, and $E(\text{Ti}_{12}\text{O}_{24})_2$ are the total energy for different TiO₂ system under investigation and pristine TiO₂ respectively. Also, $E(\text{N})$, $E(\text{Ti})$, and $E(\text{O})$ are the free energy corresponding to single nitrogen atom, titanium atom and oxygen atom respectively.

Table 3.4 Defect formation energy (E_{df}), Fermi energy and induced magnetic moment for different nitrogen-doped TiO_2 system.

Sl no.	TiO_2 System	Defect Formation energy (eV)	Fermi Energy (eV)	Difference of Fermi Energy with pristine (eV)	Remarks on Fermi energy shift.	Magnetic moment (μ_B)
1	Pristine ($Ti_{24}O_{48}$)	-	3.43	0	-	0.00
2	V_{Ti} and V_O ($Ti_{23}O_{47}$)	27.048	3.01	-0.42	p-type	0.00
3	N_{Ti} ($Ti_{23}NO_{48}$)	14.48	7.08	3.64	n-type	0.00
4	N_O ($Ti_{24}NO_{47}$)	1.8	3.44	0.02	n-type	1.01
5	N_{Ti} and N_O ($Ti_{23}N_2O_{47}$)	15.74	3.16	-0.26	p-type	0.00
6	N_{Ti} and V_O ($Ti_{23}N O_{47}$)	17.83172	5.32	1.89	n- type	0.24
7	$N_O + V_{Ti}$ ($Ti_{23}NO_{47}$)	22.5017	2.79	-0.64	p-type	0.00
8	N_{inst} ($Ti_{24}NO_{48}$)	-3.02447	4.39	0.97	n- type	1.00

It can be seen from Table 3.4 that the defect formation energy is lowest for N_{inst} system followed by N_O system. This clearly indicates that the substitution of nitrogen at oxygen site is energetically most suitable event to occur in rutile TiO_2 after interstitial site occupancy. In both the above cases, the Fermi level shifts towards the conduction band as compared to the pristine system that further enhances the n-type semiconducting behavior in TiO_2 . Similarly, in other cases (i.e. $N_O + V_{Ti}$, $V_O + V_{Ti}$ and $N_O + N_{Ti}$) the Fermi level shifts towards valence band but no induced magnetic moment is observed. Two nitrogen atoms are doped at nearby titanium and oxygen site. After the structure optimization, the distance between them is found to be 1.12 Å. This shows that the nitrogen molecule can also be trapped inside TiO_2 . The bond length of nitrogen molecule inside TiO_2 is comparable to the bond length of nitrogen

molecule as in case of Ge crystal [134]. The DFE for N_2 inside TiO_2 (i.e., $Ti_{23}N_2O_{47}$) is 15.74 eV. However, it does not induce any magnetic ordering in rutile TiO_2 . Moreover, it has been observed that the TiO_2 system doped with two nitrogen atoms at oxygen sites induces a significant magnetic moment ($\sim 2\mu_B$). Also, the spin-spin interactions study reveals a possibility of stable ferromagnetic coupling for two nitrogen atoms doped at O-site separated by a distance of $\sim 7\text{\AA}$. The local magnetization density distribution for nitrogen doped at O-site and nitrogen atom doped at interstitial site in TiO_2 structure is shown in **Figure 3.21** (a) and **Figure 3.21** (b) respectively.

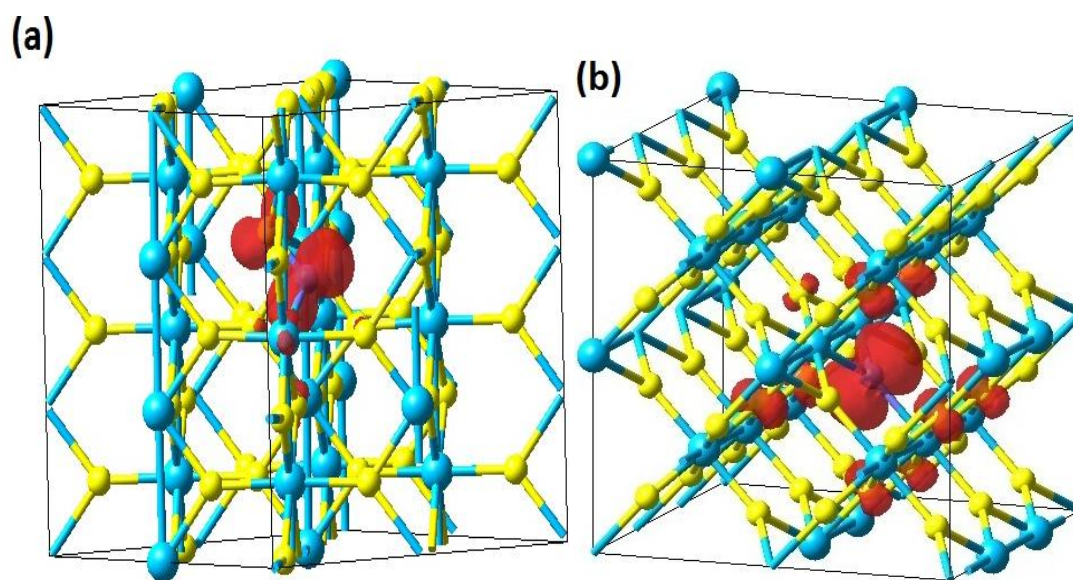


Figure 3.21 (a) Local magnetic density in TiO_2 with N_{inst} , (b) local magnetic density in TiO_2 with N_O . The blue color spherical balls represent Ti atoms and yellow color spherical balls represent O atoms, the red color patches represents the magnetic density distribution.

It can be clearly seen that the local magnetic density distribution is mostly around the dopant in both the cases and a small contribution is coming from

neighboring Ti and O atoms. The nitrogen atom ($1s^2 2s^2 2p^3$) when doped at oxygen site gets only two electrons from nearby Ti atoms and becomes $2s^2 2p^5$ in the valence shell. The one unpaired electron left in 2p states of N atom contributes to magnetic moment of $1.0 \mu_B$ in TiO_2 system. The spin polarized density of states for TiO_2 with N_O and TiO_2 with N_inst has been shown in **Figure 3.22** and **Figure 3.23** respectively.

The spin polarized density of states for nitrogen doped TiO_2 is asymmetric. The asymmetry comes from 2p orbital of nitrogen, thus give rise to magnetic moment in the system. Similarly, 2p orbital of the dopant cause asymmetry in total density of states for N_inst in TiO_2 . However, the density of states for pristine TiO_2 is perfectly symmetric as discussed in earlier sections. The local magnetic density obtained is also in good agreement with the result obtained from density of states (DOS) for all the cases.

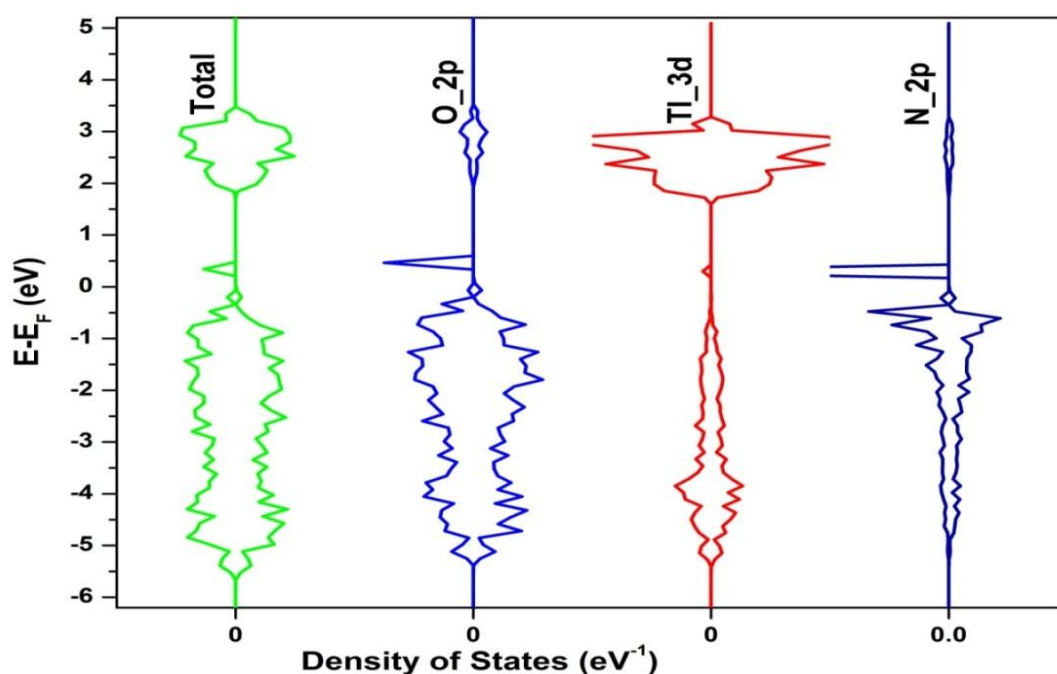


Figure 3. 22 Spin polarized density of states for TiO_2 with N_O .

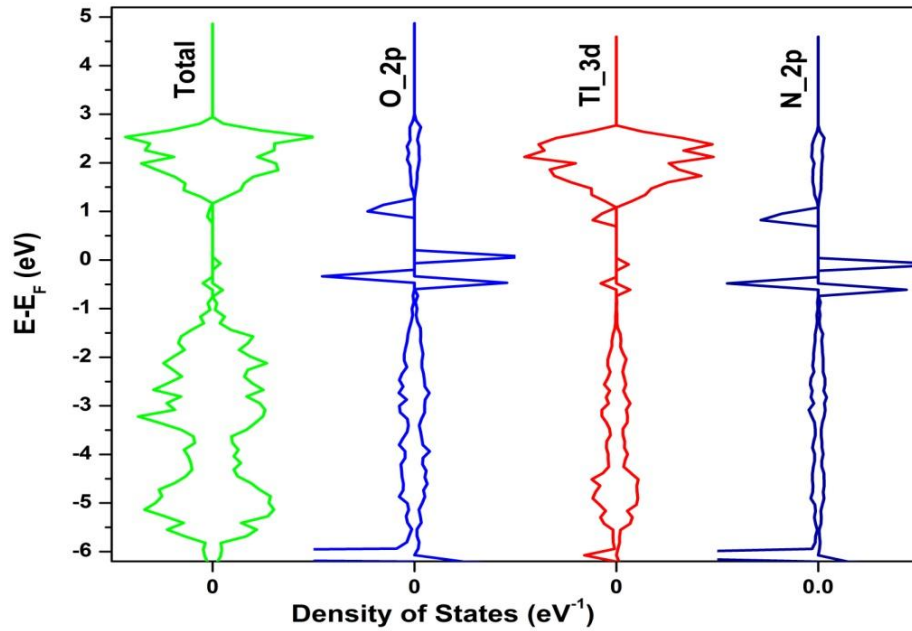


Figure 3.23 Spin polarized density of states for TiO_2 with N_{inst} .

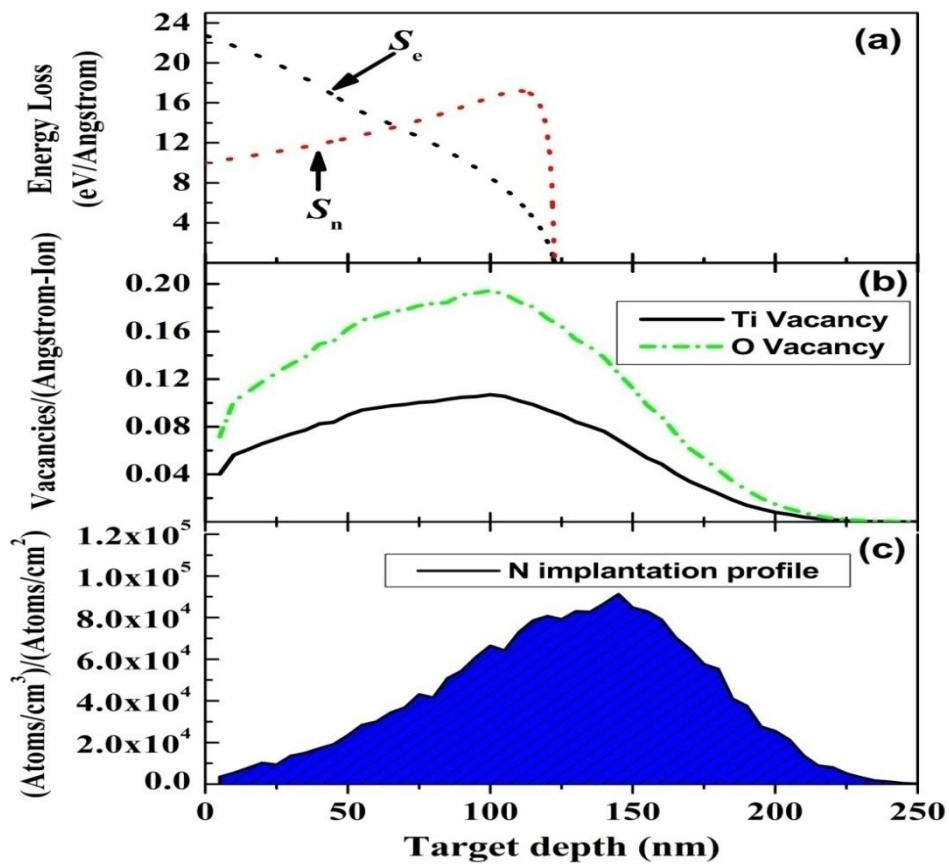


Figure 3.24 SRIM simulation for N^{4+} irradiated TiO_2 (a) The energy loss profile, (b) defect generation profile and (c) nitrogen ions distribution with target depth.

The energy loss profile of nitrogen ions when irradiated on TiO₂ has been presented in **Figure 3.24** (a). The nuclear energy loss is dominant up to 22 keV. The values of the electronic energy loss and the nuclear energy loss for 50 keV N⁴⁺ ions on TiO₂ are 29.2 eV/Å and 12.8 eV/Å respectively. TRIM simulations has been used to generate the vacancy profile in 50 keV N⁴⁺ ions irradiated TiO₂ and it is shown in **Figure 3.24** (b). From TRIM simulations it is clear that both V_{Ti} and V_O have been created in TiO₂ when irradiated with 50 keV N⁴⁺ ions. However, the numbers of V_O are greater in number than V_{Ti}. **Figure 3.24** (c) represents the distribution of Nitrogen ions with the target depth. The penetration by 50 keV N ions is upto 250 nm with maximum ion distribution at 145 nm. The Magnetization (M) V/s Field (H) curve obtained for N⁴⁺-irradiated TiO₂ is shown in **Figure 3.25**. The M-H curve is a hysteresis loop at room temperature (T~300K) with the values of saturation magnetization (M_s) and cursive field (H_C) are 9.6×10⁻³ emu/g and 338.86 Oe respectively. The ferromagnetic hysteresis loop obtained at room temperature (300 K) clearly indicates the presence of room temperature ferromagnetism in nitrogen doped rutile TiO₂.

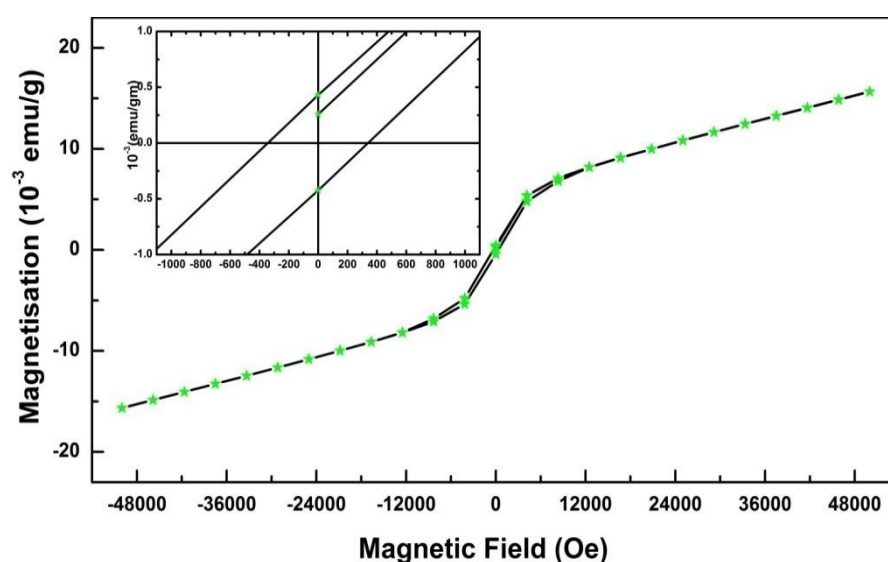


Figure 3.25 Room temperature magnetic hysteresis loop of N-irradiated TiO₂.

3.8 Room temperature ferromagnetism in boron doped TiO₂

Theoretical calculations under the framework of DFT suggest that there is a significant induced magnetic moment in boron doped oxide TiO₂. The magnetic moment generated for boron atom doped in various oxides is described in the earlier section 3.3.1. The primary source of magnetism in all the cases is the 2p orbital electrons of boron along with a small contribution from 2p orbital electrons of oxygen atom in the neighborhood of the dopant. Boron atom has the electronic configuration of $2s^2 2p^1$ in its valence shell. When oxygen gets substituted by boron atom, it pulls the electrons from the neighboring metal ion as the electronegativity of boron is 2.04 [135]. There is a transfer of two electrons towards boron atom from neighboring metal ion. Now the boron atom has the electronic configuration of $2s^2, 2p^3$ in its valence shell. Thus leaves three unpaired electrons in the boron atom inside the oxide system. These unpaired electrons in 2p orbital of boron generate $\sim 3\mu_B$ magnetic moment per boron atom doping for ZnO, details will be discussed in chapter 4, section 4.5. However, in case of TiO₂, there is an extra oxygen (with electro negativity 3.44 [135]) attached with the metal ion. The oxygen atom pulls more electron cloud towards itself and boron atom pulls fewer electrons as compared to the case of ZnO system. This leads to the generation of less magnetic moment in the TiO₂ system.

Free energy calculated for spin ordered system has been compared between ferromagnetic system and anti-ferromagnetic system. It has been found that the ground state energy of ferromagnetic state is lower as compared to anti-ferromagnetic state for B-doped TiO₂ system. It can be clearly observed from **Figure 3.26** that, in case of boron doped TiO₂, there is asymmetry both in total DOS and partial DOS around Fermi energy level. The asymmetry in DOS indicates there is uneven

distribution of spin polarized electrons. The partial DOS analysis reveals 2p orbital of boron atom doped inside the system produces a maximum asymmetry.

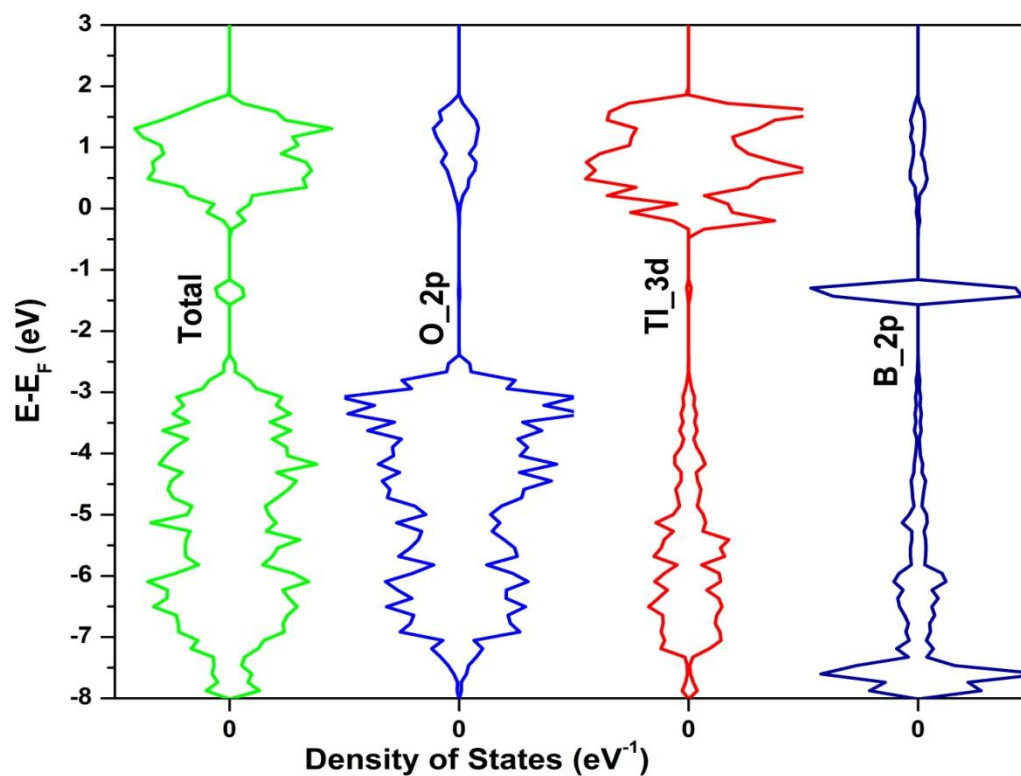


Figure 3.26 Partial and total density of states in boron doped system TiO₂.

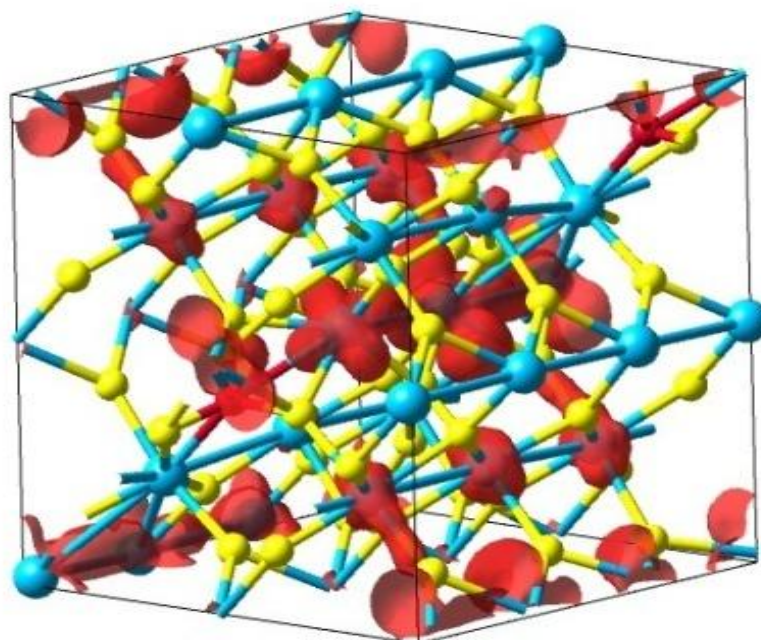


Figure 3.27 Local magnetic density (spin-polarized) distribution in boron doped TiO₂.

Spin polarized density of states calculations have been performed for boron doped at O-site in TiO₂ system. The spin polarized DOS for B doped TiO₂ system has been plotted in **Figure 3.26**. Also, 2p orbital electrons of boron atom contribute a significant moment in all the boron doped systems. It can be observed from the total DOS distribution in B-doped system that there has been generation of donor like states above valence band. Thus makes the boron doped system more n-type semiconductor as compared to the pristine system. Also, the Fermi level shifts towards conduction band in B-doped system as compared to that of pristine TiO₂. The local magnetic density distribution has also been simulated at spin-polarized condition and is represented in **Figure 3.27**. It can be seen from local magnetic density calculation that the major contribution of magnetism comes from boron atom; along with a small contribution from neighboring oxygen atoms and the titanium atoms. According to theoretical prediction under the framework of DFT, the boron doped TiO₂ samples have been prepared.

The energy loss profile of boron ions when irradiated on TiO₂ has been presented in **Figure 3.28** (a). The nuclear energy loss dominates over electronic loss leading to the generation of significant amount of atomic vacancies. TRIM simulations has been used to generate the vacancy profile in 10 keV B⁺ ions irradiated TiO₂ and it is shown in **Figure 3.28** (b). From TRIM simulations it is clear that both V_{Ti} and V_O have been created in TiO₂ when irradiated with 10 keV B⁺ ions. However, the numbers of V_O are greater in number than V_{Ti}. Similarly, distribution of boron ions with the target depth has been shown in **Figure 3.28** (c). The penetration by 10 keV B⁺ ions in polycrystalline TiO₂ sample is found to be ~ 80 nm and maximum ion distribution is found in the range of 20 - 50 nm.

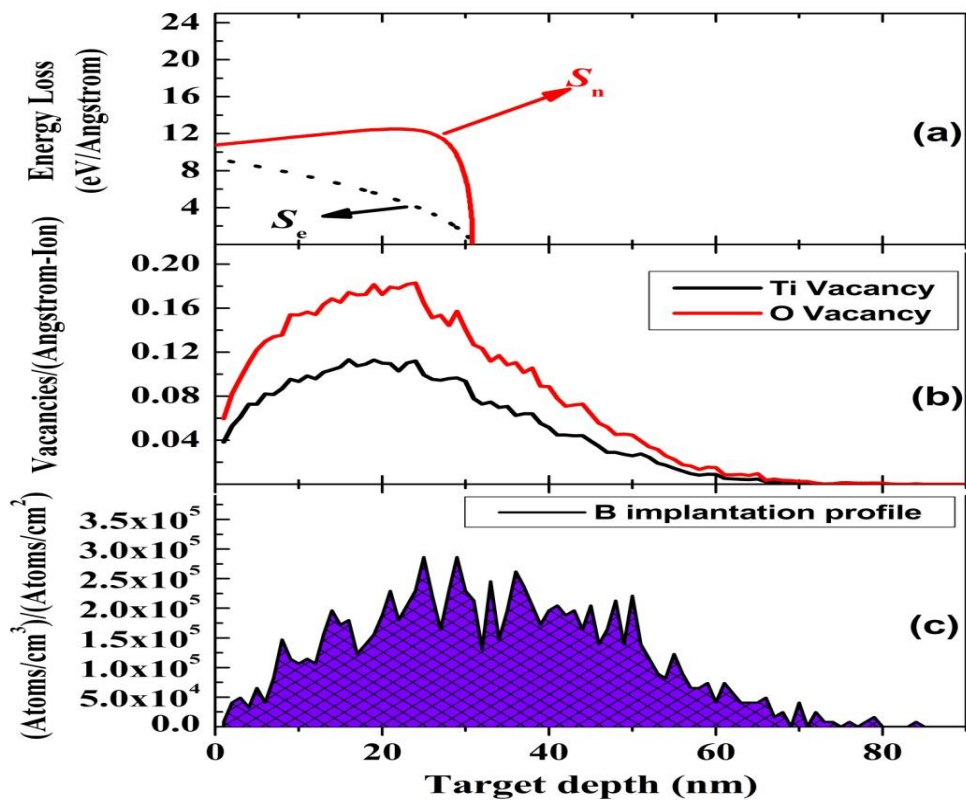


Figure 3.28 SRIM simulation for B^+ irradiated TiO_2 (a) The energy loss profile, (b) defect generation profile and (c) boron ions distribution with target depth.

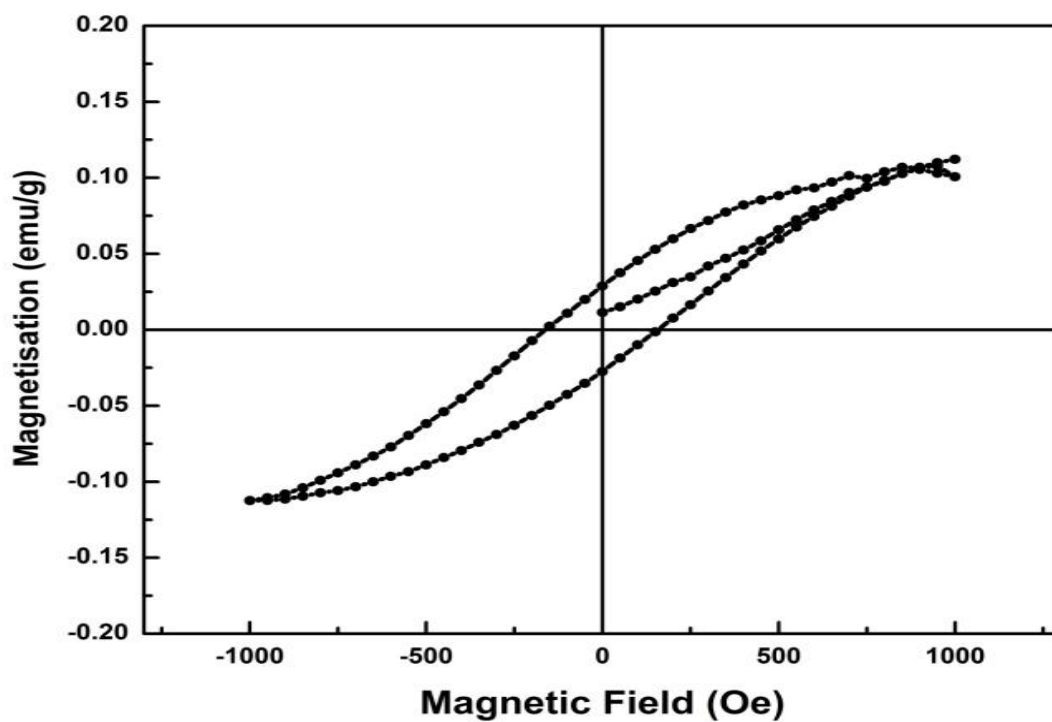


Figure 3.29 Magnetization vs magnetic field plot for boron implanted TiO_2 .

The magnetic measurements have been carried out for B⁺ implanted oxide samples. The magnetization versus field (M vs H) plot obtained by SQUID magnetometer for rutile TiO₂ systems is shown in **Figure 3.29**. The value of saturation magnetization, remanent magnetization and coercive field has been calculated and are found to be 0.109 emu/g, 0.0287 emu/g and 160.46 Oe respectively. Thus the hysteresis loop obtained confirms the presence of room temperature ferromagnetism in 10 keV B⁺ ion irradiated TiO₂ sample.

3.9 Conclusions

Possibility of room ferromagnetism in rutile-TiO₂ has been studied by employing both theoretical and experimental methods. The theoretical calculations under density functional theory predicts that a significant amount of magnetic moment gets generate into the TiO₂ by doping different p-block elements. The sources of magnetism are the p-orbital electrons of dopant atom when sits at the oxygen site. However, when doped at Ti-site, these elements do not produce any magnetic moment in the system. The spin-spin interactions study reveals that only B, C, N and P atom doped system gets ferromagnetic coupling between the net-spins of two dopant atoms present at O-site. The generation of Both V_{Ti} and V_O generates a significant amount of magnetic moment in the system. The magnetic moment generated by the creation of vacancies gets added up with that produced from the external dopant in the system. The theoretical predictions are verified with the experimental results. A strong ferromagnetism has been found experimentally for TiO₂ sample containing Ti-vacancy and also N-implanted, C-implanted and B-implanted rutile TiO₂ samples.

Chapter-4

Defect induced ferromagnetism in ZnO

4.1 Introduction

ZnO is a wide band gap semiconductor with a band gap of 3.3 eV and it is also diamagnetic material in pristine form. It is one of the first materials where ferromagnetic property has been predicted theoretically. But, in the recent decade researchers have discovered ferromagnetic property in undoped [77, 78] as well as non magnetic impurities doped ZnO system [80]. H. Pan *et al.*, theoretically calculated the values of induced magnetic moment of $2.02 \mu_B$ per carbon atom when it is doped at oxygen site in ZnO [84]. They also reported experimental value of $1.5 - 3.0 \mu_B$ magnetic moments in carbon atom doped ZnO thin films by pulsed laser deposition technique [84]. Shen *et al.*, theoretically predicted ferromagnetism in nitrogen doped ZnO [136]. Later, it has been shown that there is an enhancement of room temperature ferromagnetism by co-doping of nitrogen in carbon doped ZnO samples [137]. Despite of these studies, the origin of magnetic property in p-block elements doped ZnO system is not clearly understood and needs further investigations. Also, the investigations on origin of room temperature ferromagnetism in ZnO highlight the importance of atomic vacancies (mainly Zn vacancies) in generating vacancies. So, there is an urge to understand the generation of atomic vacancies in ZnO as the vacancies plays vital role in the origin of ferromagnetism in undoped ZnO system.

In the present chapter, the magnetic property of various p-block elements doped ZnO along with the spin - spin interaction study to find the possibility of

ferromagnetism in these systems have been discussed. Both the oxygen and Zinc sites have been chosen for doping. Formation of vacancies in ZnO has been studied explicitly as they have a key role in generating ferromagnetic behavior in ZnO system. Both in-situ and ex-situ PAS measurements along with low temperature photoluminescence studies have been carried out for complete understanding of the process. Energetic ion beam has been irradiated for creating defects (vacancy and implantation/doping) in the sample. The magnetic measurements have been carried out using SQUID magnetometer.

4.2 Computational Methodology

Vienna *ab-initio* simulation (VASP) code [120-123], along with the MedeA software package have been employed for the theoretical calculation based on the density functional theory (DFT). A Wurtzite unit cell of ZnO having space group $P6_3mc$ with optimized lattice constants of $a = b = 3.25 \text{ \AA}$ and $c = 5.2 \text{ \AA}$ has been used for calculations. The super cell size for all the calculations has been taken to be $3 \times 3 \times 3$ unit cells (i.e., with 108 atoms in a super cell ZnO). The generalized gradient approximation (GGA) with Perdew-Burke-Ernzerhof (PBE) exchange and correlation [124] method has been followed throughout the calculations to study all the system. Periodic boundary conditions have been introduced along all the basis vectors. In the pristine ZnO super-cell, two Zn atoms and two O atoms have been substituted systematically with various p-block elements (i.e., $Zn_{54}X_2O_{52}$; X = B, C, N, Al, Si, P, Ga, Ge, As) and also, one atomic vacancy has been created (V_{Zn} or V_O). Each structure has been geometrically relaxed until the maximum value of the unbalanced inter-atomic force component (Hellman-Feynman force) is less than $0.02\text{eV}/\text{\AA}$. The

spin polarized density of states has been calculated for each optimized structure in the frame work of density functional theory. The induced magnetic moment for each system has been calculated. The Brillouin zone (BZ) of the super cells has been divided by $3 \times 3 \times 3$ Monkhorst-Pack (MP) k-points [125]. In all calculations, 400 eV mesh cut-off energy has been taken into account to expand the plane wave basis set, and 10^{-5} eV tolerance has been fixed as stopping criteria of the self-consistent loop to reach the electronic ground state. The spin-spin interactions study has been done by doping two dopants at two different positions, one in the same unit cell and other at the adjacent unit cell. The ground state free energy of both ferromagnetic state and anti-ferromagnetic state has been calculated and compared to know the stability of ordered state in all the $Zn_{24}X_2O_{52}$ cases. The ferromagnetic ordering has been achieved by aligning all the spins in one direction and G-type anti-ferromagnetic ground states have been considered to study the anti-parallel ordering. Local magnetic density (LMD) distribution has been calculated for spin polarized configuration. The simulations of energy loss and penetration depth for different ions irradiation has been carried out using SRIM software [126].

4.3 Experimental details

Wurtzite structured (Sigma-Aldrich, Germany) polycrystalline powder 99.99% pure ZnO has been pelletized in the form of thick pellets (~0.5 mm - 0.7 mm) with high palletizing pressure (~220 MPa). The pallets were then annealed at high temperature (450 °C - 700 °C at different sittings) for 5 hours before irradiation. Irradiation experiment with 10 keV B^+ ion beam produced from electron cyclotron resonance (ECR- 6.4 GHz) ion source of the radioactive ion beam (RIB) facility,

VECC, Kolkata has been irradiated uniformly over the surface of polycrystalline pellet at a fluence of 1×10^{16} ions/cm². During the irradiation process, the beam current for the ions has been kept in the order of $\sim 1 \mu\text{A}$. The magnetic measurements have been carried out using Quantum Design make SQUIDs magnetometer.

The Doppler broadened lineshape of the electron-positron annihilation 511 keV γ - ray has been measured using HPGe detector as described in Section 3.3. The source sample sandwich has been placed inside an oven type furnace (30–600 °C with ± 2 °C at the sample site) for the in-situ temperature dependent DB spectrum measurement. The experimental set-up is schematically depicted in **Figure 4.1**. The DB spectra have been analyzed by evaluating the *S*-parameter defined by the ratio of the counts in the central area of the 511 keV photo peak ($|511 \text{ keV} - E_{\gamma}| \leq 0.85 \text{ keV}$) and the total area of the photo peak ($|511 \text{ keV} - E_{\gamma}| \leq 4.25 \text{ keV}$). For this particular time sequential in-situ measurement the counts have been recorded for 10 minutes interval, optimized between the requirement of statistics and observable changes in *S*-parameter due to defect migration time, if any. The total counts (recorded in a dual ADC based multiparameter data acquisition system, MPA-3 of FAST ComTec., Germany) under the 511 keV peak during this time period is 1×10^6 .

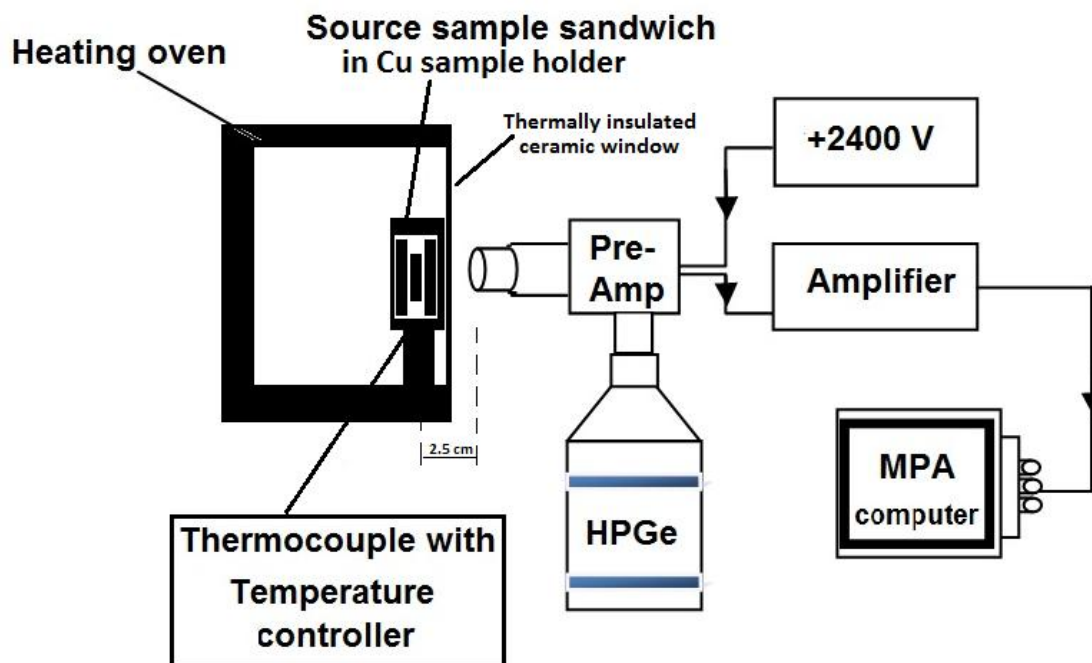


Figure 4.1 Schematic diagram of the set up for *in-situ* temperature (above 300 K) dependent Doppler broadening spectroscopy.

For the off line CDB spectrum measurement at room temperature (RT), samples have annealed at 182 °C and 286 °C, exactly in the same sequence followed in case of *in-situ* measurement. The only difference is that both the samples have been furnace cooled down to RT. Similarly for another set up, the pallets have been annealed at two different temperatures 325 °C and 450 °C for four hours and then furnace cooled to room temperature. The source sample sandwich has been placed in between two identical HPGe detectors. The Ratio curve from the measured spectrum has been constructed with respect to the same of a ZnO single crystal (hydrothermally grown, MTI Corporation, USA). Other details of the experimental set-up along with the data analysis have been reported in ref. [138].

Photoluminescence (PL) spectrum at 10 K have been recorded using 325 nm He-Cd laser as excitation source (output power 45 mW) and a TRIAX 320 monochromator fitted with cooled Hamamatsu R928 photomultiplier detector.

4.4 Ferromagnetism in p-block elements doped ZnO

Different p-block elements e.g., B, C, N, Al, Si, N, P, Ge, Ga and As have been substituted in ZnO both in O-site and Ti-site respectively. The elements have been doped at two different positions of oxygen in ZnO, maintaining the distance between the two substitutional atoms (X_O) different, one short and the other at long position. Substitution of any one of the p-block elements in the Zn site of ZnO results zero magnetic moment. The induced magnetic moment of $Zn_{54}X_2O_{52}$ system (with $X = B, C, N, Al, Si, N, P, Ge, Ga, As$) and ZnO with V_{Zn} and V_O has been plotted in **Figure 4.2**.

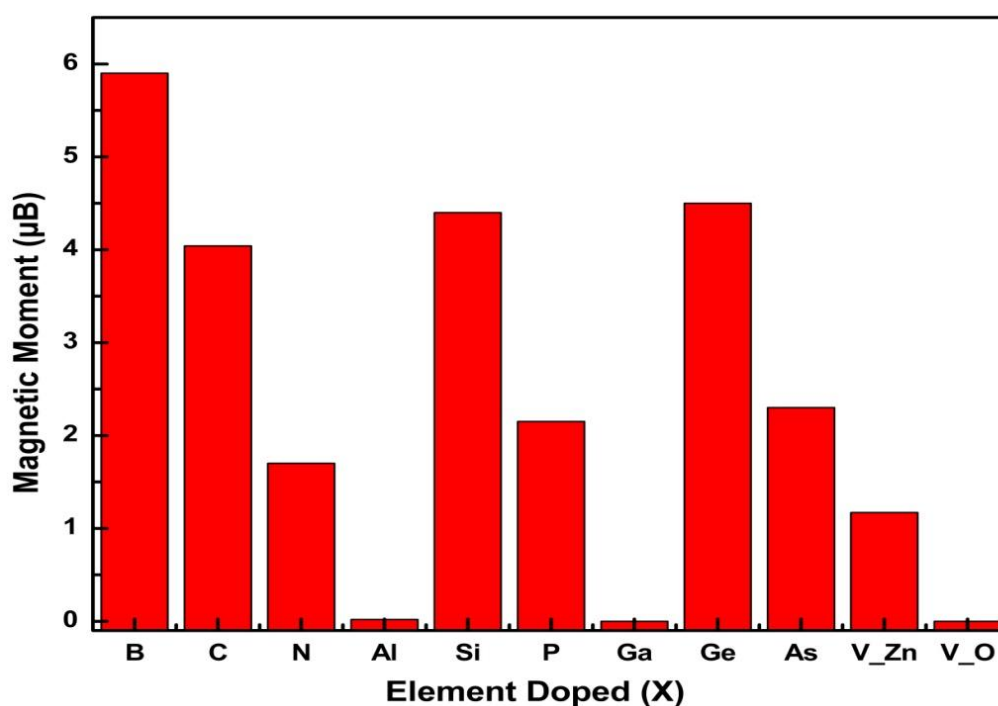


Figure 4.2 Induced magnetic moment for $Zn_{54} X_2 O_{52}$ ($X = B, C, N, Al, Si, N, P, Ge, Ga$ and As) system and ZnO system with single V_{Zn} and V_O .

Table 4.1 Total energy, optimized doping distance, defect formation energy (E_{df}) and induced magnetic moment for different elements doped at oxygen site (X_O) of ZnO.

Name of the Element Doped	Distance between two doped atoms (in Å)	Induced magnetic moment (μ_B)	Defect Formation Energy (E_{df}) (eV) *FM # AFM.	$\Delta E = (E_{FM} - E_{AFM})$ (meV)
B	5.14	5.91	11.36422	31.5
			11.33276	
	8.00	2.01	11.44201	-0.4
			11.44245	
C	5.20	4.04	6.19424	0.0
			6.19424	
	8.04	4.04	5.9326	-5.8
			5.9385	
N	5.17	1.58	2.34261	-107
			2.34707	
	7.94	1.72	2.36187	-4.5
			2.469644	
Al	4.68	0.019	14.78046	0.0
			14.78046	
Si	9.85	4.30	13.62607	-31.5
			13.65758	
	11.47	4.59	13.88773	-16.18
			13.90391	
P	6.11	1.88	9.63777	-1.4
			9.63917	
	7.94	2.15	9.60347	-0.2
			9.60367	
Ge	4.89	4.11	15.1015871	-33.09
			15.13468	
	7.94	4.54	15.341693	-10.09
			15.35178	
As	7.94	2.34	12.10406	-21.65
			12.125714	

Table 4.1 represents the structure optimized parameters of viz., optimized distance between the two doping site, induced magnetic moment and the defect

formation energy E_{df} . The defect formation energy for doping of different 'X' (X= p block elements) in ZnO has been calculated by the following formula given in equation (15) [80, 127].

$$E_{df}(X) = E(\text{Zn}_{54}\text{O}_{52}\text{X}_2) - E(\text{ZnO})_{54} - 2E(X) + 2E(O) \dots\dots\dots (15)$$

where, $E_{df}(X)$ is the defect formation energy corresponding to doping of X (X= B, C, N, Al, Si, N, P, Ge, Ga and As), $E(\text{Zn}_{54}\text{O}_{52}\text{X}_2)$ and $E(\text{ZnO})_{54}$ are the total energy for X_O doped ZnO system and pristine ZnO respectively; also $E(X)$ and $E(O)$ are the total energy corresponding to single doped atom and oxygen atom respectively.

From Table 4.1, it is clear that due to doping of different p-block element in the same oxygen site of ZnO the distance between the two doping site does not remain constant rather there is significant amount of structural deformation which is due to the size of the doped element. In case of boron at oxygen site (B_O) and aluminum at oxygen site (Al_O) magnetic moment arises due to the dopant and a small contribution comes from the unpaired electrons (3d electron) of Zinc atom. In the periodic table, Al (valence electronic configurations of $3s^23p^1$) is just below B (valence electronic configurations of $2s^22p^1$), but the magnetic moment induced for B_O is $5.9 \mu_B$ while for Al_O is $0.019\mu_B$. Similar result has been observed [80] in case of ZnO with B_O and Al_O , which has been explained with the help of electronegativity of the dopants. In case of C_O (doping of carbon at oxygen site) the induced magnetic moment is $\sim 4 \mu_B$. Here the 2p electrons of carbon atoms are responsible for inducing magnetic moment in ZnO. Doping of silicon and Ge atoms at oxygen sites induce magnetic moment of $\sim 4.5 \mu_B$, which is again due to the dopant and a small contribution comes from 3d orbital electron of Zn atom. The slightly higher value of magnetic moment in case of Si_O may be due to quite large atomic sizes of the Si, similar to ZnO case [80]. The doping of group 15

elements of periodic elements e.g., N, P, As, also induces a significant magnetic moment in ZnO. Here the magnetic moment comes from the p -orbital electron of the doped element. In all the three cases the magnetic moment is $\sim 2 \mu_B$. To investigate the interaction between the magnetic moments, the calculations with the two magnetization configurations, i.e., ferromagnetic (FM) and anti-ferromagnetic (AFM) states for all p-block element substituted ZnO system have been carried out. Two different distances between the defect sites ($X_O - X_O$) have been chosen for the spin-spin interaction study. The atomic positions in both FM and AFM cases have been fully optimized and the total free energy has been computed. The optimized long and short distances along with other parameter has been listed in Table 4.1. It is interesting that the induced magnetic moments depend also on the distances between the two defect sites in the ZnO.

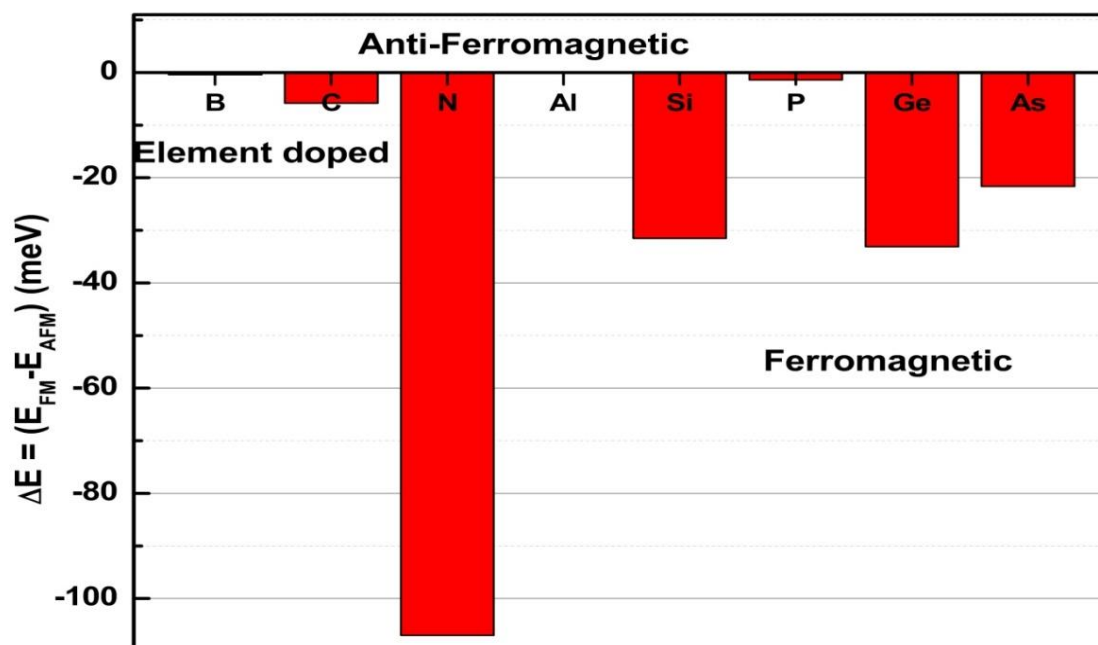


Figure 4.3 Energy difference between ferromagnetic and anti-ferromagnetic states for various p-block elements doped ZnO system.

The present *ab-initio* calculation reveals that doping of carbon atom at oxygen site gives a stable ferromagnetic state, which is in agreement with the results obtained by earlier theoretical result [84]. **Figure 4.3** shows the energy difference between ferromagnetic state and anti-ferromagnetic state for all p-block element doped ZnO. It can be easily observed from **Figure 4.3** that the free energy for parallel spin alignment is less for all the cases except Al and Ga doped ZnO system. The spin polarized density of states of pristine ZnO and ZnO doped with various p-block elements (viz., B, C, N, Al, Si, P, Ga, Ge and As) have been shown in **Figure 4.4**.

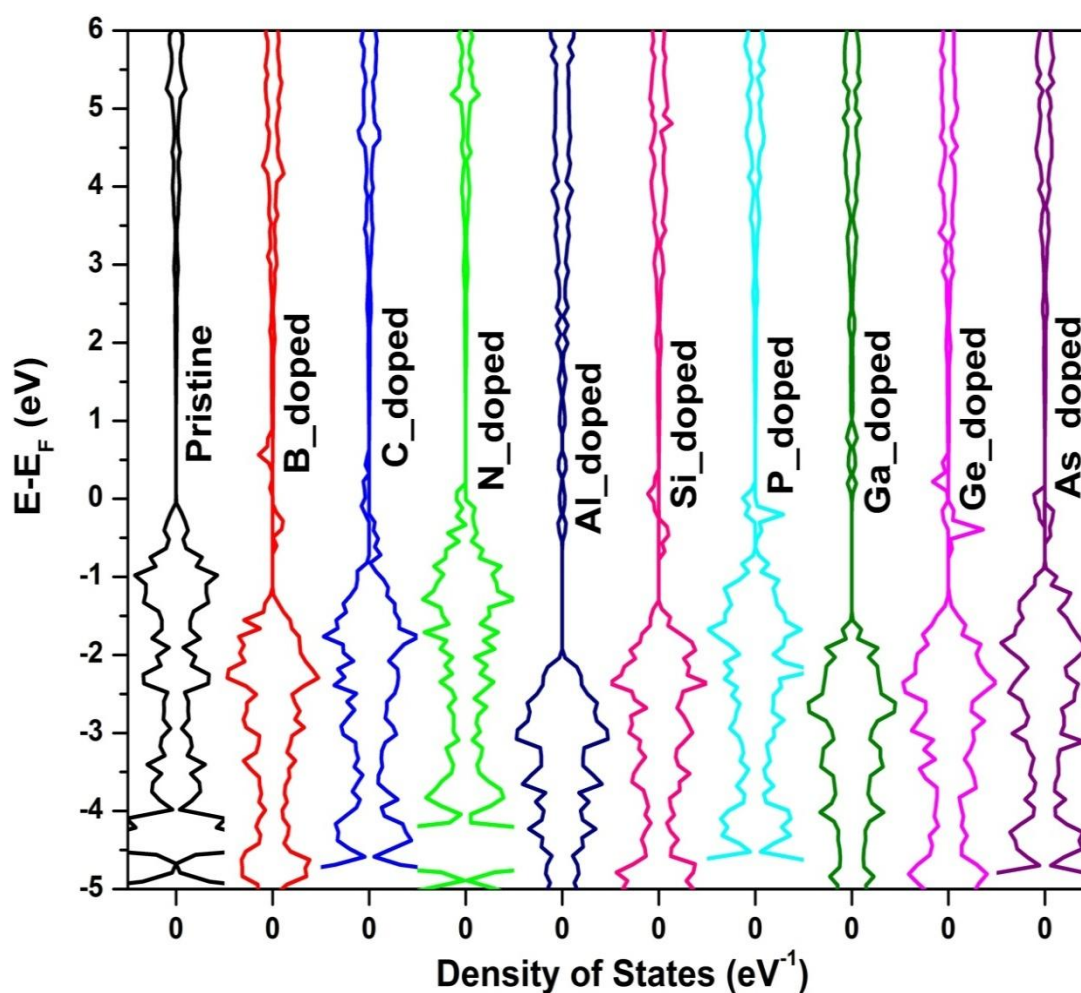


Figure 4.4 Spin polarized total density of states for various p-block elements doped ZnO.

The density of states for pristine ZnO is symmetric which corresponds to an equal number of up spin electrons and down spin electrons in the system and thus yields zero magnetic moment. But, the spin polarized density of states of ZnO with B, C, N, Si, P, Ge and As have asymmetric nature in DOS yielding a non zero magnetic moment in the system. The creation of one cationic vacancy (V_{Zn}) generates a moment of $1.1 \mu_B$ but no significant moment is found for anionic vacancy (V_O).

4.5 Room temperature ferromagnetism in boron doped ZnO

As discussed in section 4.4, theoretical calculations under the framework of DFT suggest that there is a significant induced magnetic moment in boron doped ZnO. The primary source of magnetism in all the cases is the 2p orbital electrons of boron along with a small contribution from 2p orbital electrons of oxygen atom in the neighborhood of the dopant. Boron atom has the electronic configuration of $2s^2 2p^1$ in its valence shell. When oxygen gets substituted by boron atom, it pulls the electrons from the neighboring metal ion as the electro negativity of boron is 2.04 [135]. There is a transfer of two electrons towards boron atom from neighboring metal ion (unlike the case of TiO_2 where the metal ion is attached to one more O-atom and it does not get two electrons from the metal ion). After this, the boron atom has the electronic configuration of $2s^2, 2p^3$ in its valence shell. Thus it leaves three unpaired electrons in the boron atom inside the oxide system. These unpaired electrons in 2p orbital of boron generate $\sim 3\mu_B$ magnetic moment per boron atom doping for ZnO. Spin polarized density of states calculations have been performed for pristine system and boron doped at O-site in ZnO system. The DOS distributions in pristine ZnO system and B-doped ZnO system have been compared as shown in **Figure 4.5** (a) and **Figure**

4.5 (b) respectively. Both the partial DOS and total DOS distribution are symmetric for the pristine system. The symmetry in DOS distribution indicates the presence of equal number of up spin electrons and down spin electrons in the system. Hence, there are no unpaired electrons in the system; as a result, there is no significant magnetic moment in the pristine system. But in case of boron doped system, there is asymmetry both in total DOS and partial DOS around Fermi energy level. The asymmetry in DOS indicates there is uneven distribution of spin polarized electrons.

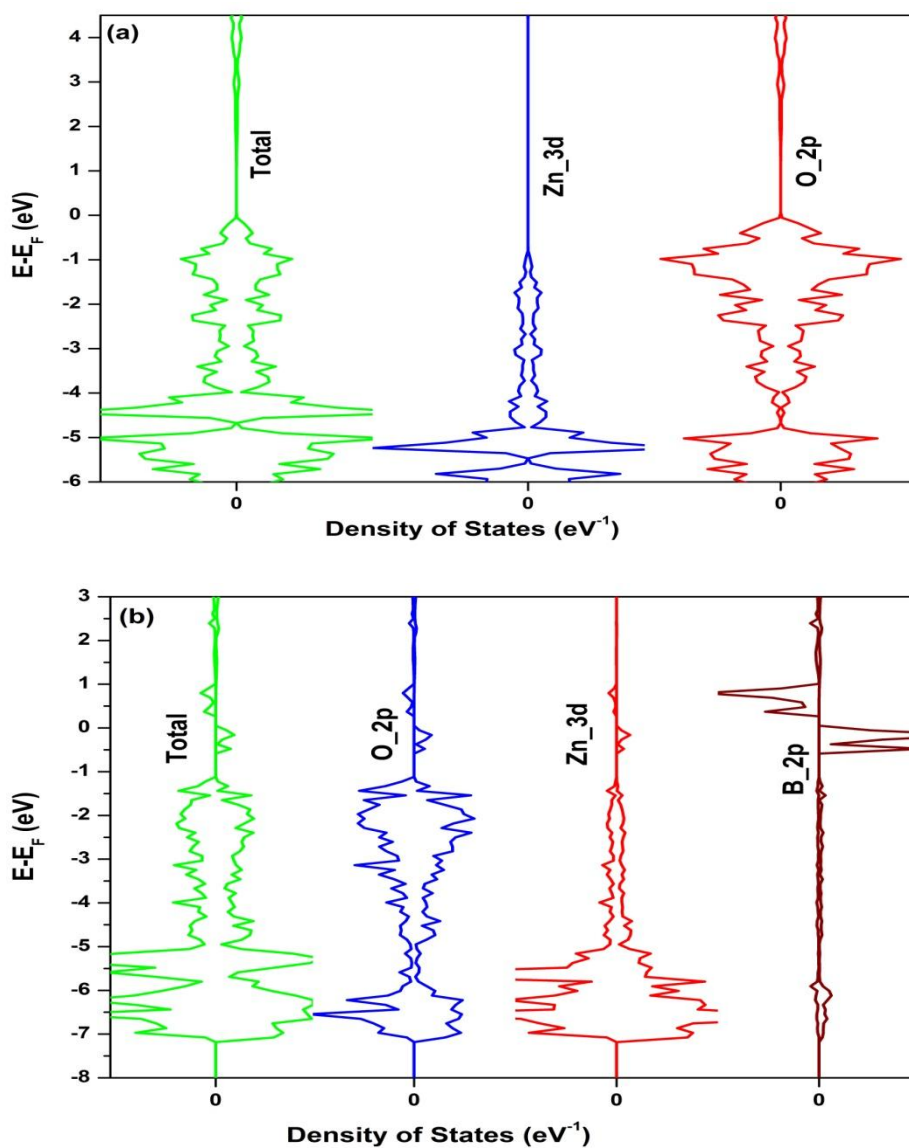


Figure 4.5 Partial and total density of states distribution a) pristine ZnO and b) boron doped ZnO system.

The partial DOS analysis reveals 2p orbital of boron atom doped inside the system produces a maximum asymmetry. Also, 2p orbital electrons of boron atom contribute a significant moment in all the boron doped systems. Comparing the total DOS in the B-doped system, it can be observed that there has been generation of donor like states above valence band. This makes the boron doped system more n-type semiconductor as compared to the pristine system. Also, the Fermi level shifts towards conduction band; this indicates n-type behavior. The local magnetic density distribution has also been simulated at spin-polarized condition and is shown in **Figure 4.6**. It can be observed from local magnetic density calculation that the major contribution of magnetism comes from boron atom; along with a small contribution from neighboring oxygen atoms and the metal atoms.

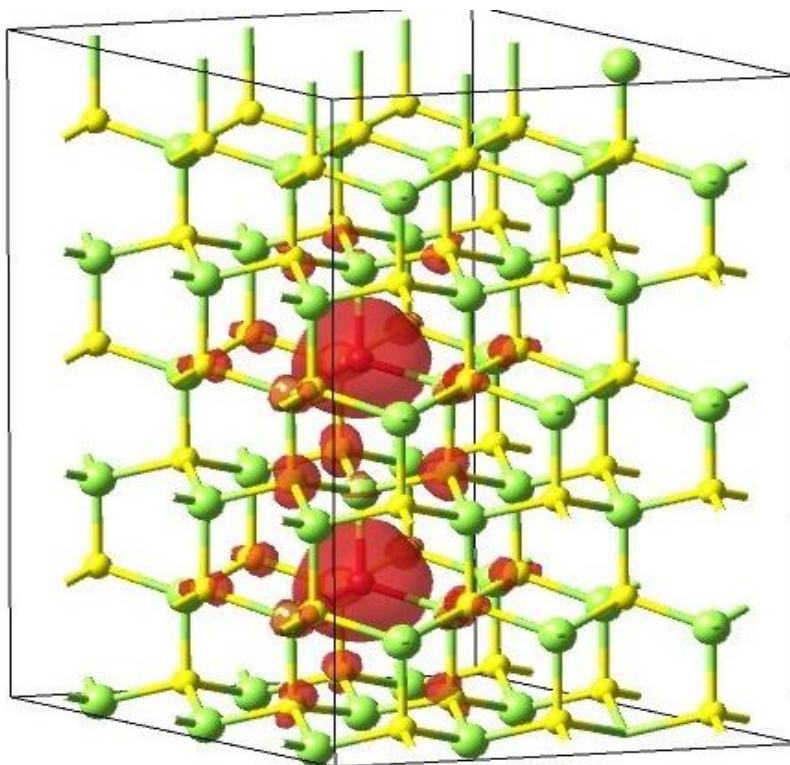


Figure 4.6 Local magnetic density distributions for boron doped ZnO, the magnetization is localized around the dopant.

The energy loss profile of boron ions when irradiated on ZnO has been presented in **Figure 4.7 (a)**. The nuclear energy loss dominates over electronic loss leading to the generation of significant amount of atomic vacancies. TRIM simulations has been used to generate the vacancy profile in 10 keV B⁺ ions irradiated ZnO and it is shown in **Figure 4.7 (b)**. From TRIM simulations it is clear that both V_{Zn} and V_O are created in ZnO when irradiated with 10 keV B⁺ ions. However, the numbers of V_{Zn} are greater in number than V_O, unlike the case of TiO₂ where the numbers of V_O were greater than V_{Ti}. Similarly, distribution of boron ions with the target depth has been shown in **Figure 4.7 (c)**. The penetration by 10 keV B⁺ ions in polycrystalline ZnO sample is found to be ~ 90 nm and maximum ion distribution is found in the range of 20 - 40 nm.

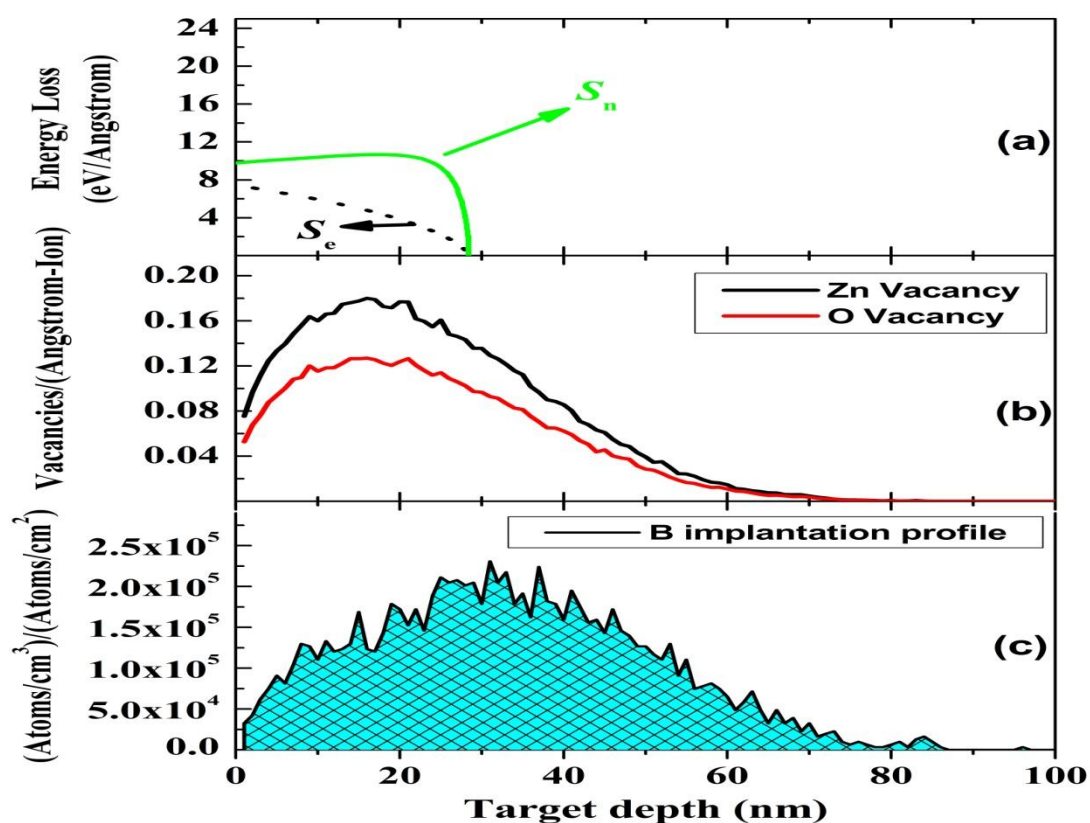


Figure 4.7 SRIM simulations for B⁺ irradiated ZnO (a) The energy loss profile, (b) defect generation profile and (c) boron ions distribution with target depth.

Magnetic characterization for 10 keV B⁺ ions irradiated ZnO has been carried out at room temperature and is depicted in **Figure 4.8**. The behavior of the M vs H curve is a hysteresis loop at room temperature (~300 K). From the hysteresis curve the values of saturation magnetization (M_s) and coercive field (H_C) has been found to be 1.3×10^{-3} emu/g and 387 Oe respectively. The hysteresis curve as obtained from the present experimental data at room temperature confirmed the presence of room temperature ferromagnetism in 10 keV B⁺ ions irradiated/implanted rutile ZnO. This result agrees with the report by X.G. Xu *et al.*, on intrinsic RTFM in B-doped ZnO thin films prepared by pulsed laser deposition technique [79].

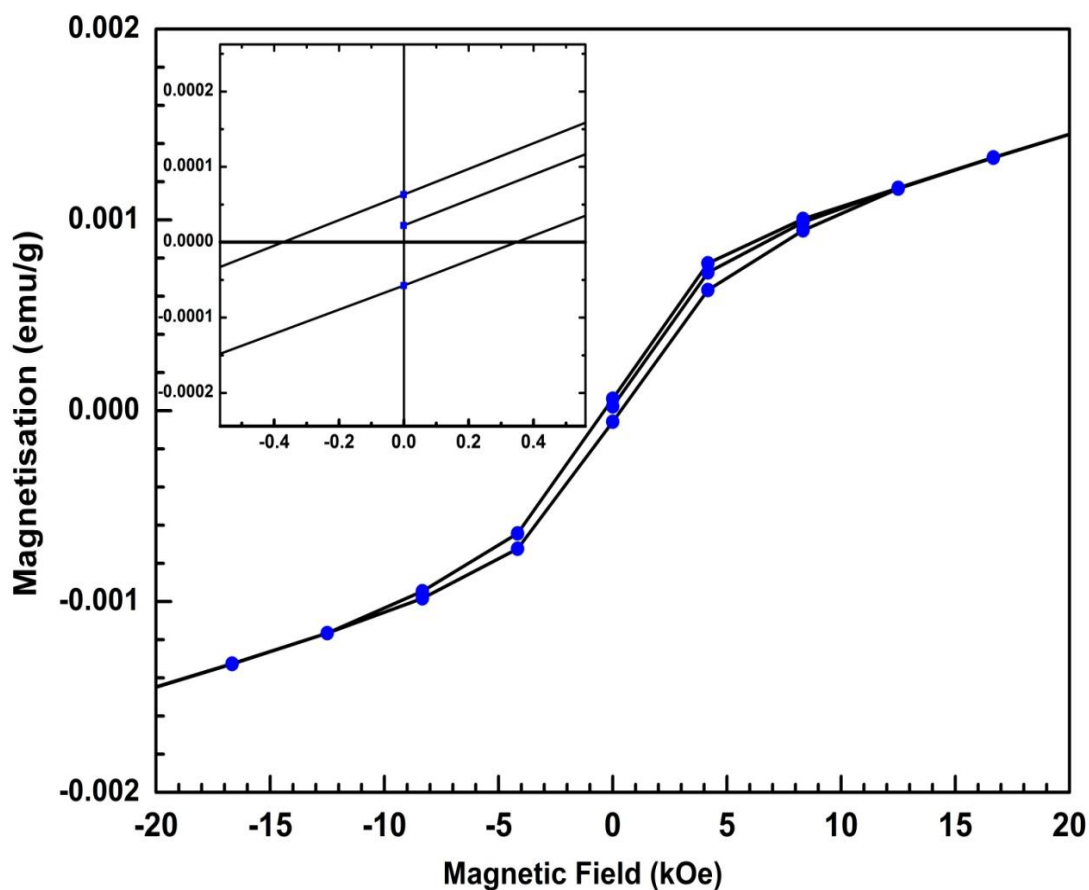


Figure 4.8 Magnetization vs magnetic field plot for 10 keV B⁺ ion implanted ZnO.

4.6 Defect generation study in granular ZnO

4.6.1 Defects generation and recovery in polycrystalline ZnO

Figure 4.9 represents the results of in-situ S -parameter measurement during the increase of temperature in three steps from room temperature to 286 °C. Measurements at 100 °C for 180 minutes do not induce noticeable change. Increasing the temperature to 182 °C causes an increment of S -parameter which eventually saturates after 90 minutes. Further, increasing the temperature at 286 °C induces another notable increase of the S -parameter. The corresponding increase stops more or less in a similar time scale compared to the earlier one.

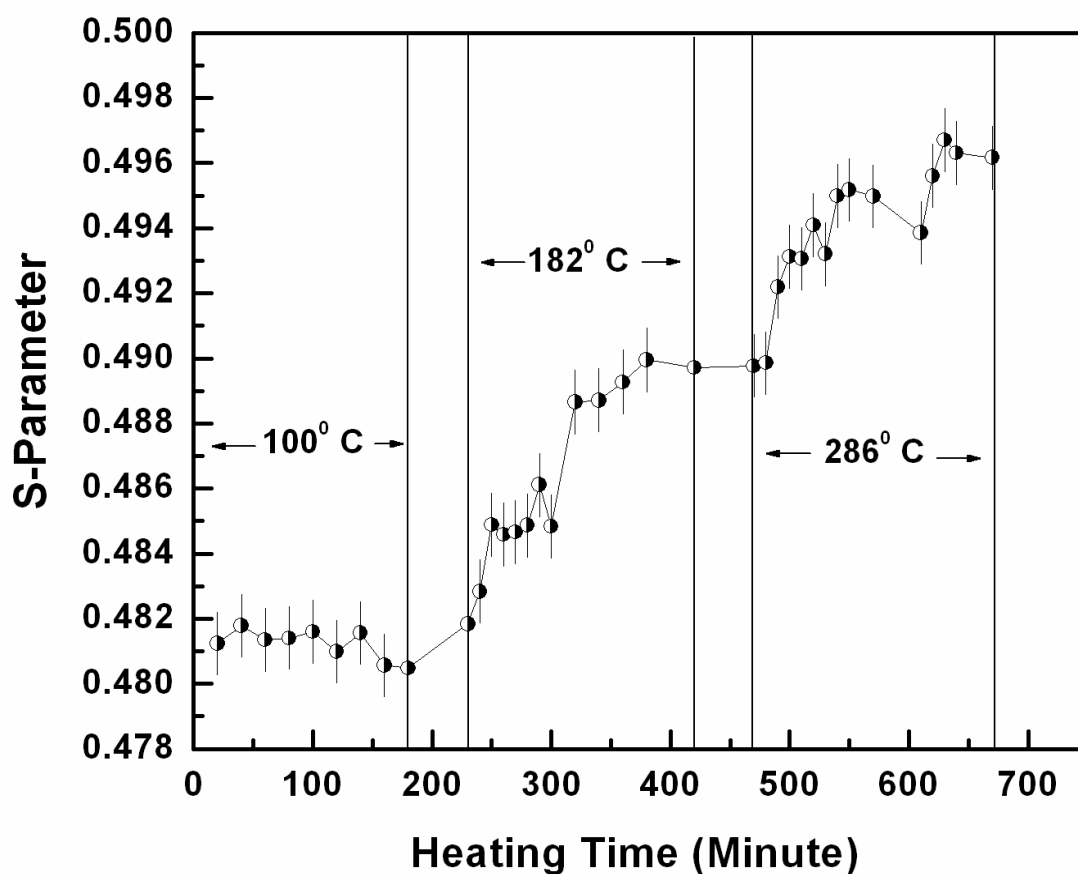


Figure 4.9 Variation of S -parameter with heating time during in-situ DB spectrum measurement of polycrystalline ZnO.

The enhancement of S -parameter with time at 182 °C is due to removal [139] of loosely bound hydroxyl (-OH) and carbon related species from the system and thereby increasing the open volume defects in the system. After certain time, the removal is complete and the increase of S -parameter stops. For annealing at 286 °C several competing processes start. The dominating process is the migration and agglomeration of defects in the form clusters and pairs [94]. The most probable defects are V_{Zn} - V_O , $2V_{Zn}$ - V_O and V_{Zn} - V_O types depending on the local free energy minimization subject to the availability of particular defect types. At the same time, recovery of defects can take place, particularly for 286 °C annealing of ZnO. The recovery of isolated V_{Zn} defects [104] is predicted to be around 266 °C. Several techniques, other than PAS have also detected recovery of defects for annealing above 250 °C [107]. Finally, both recovery and generation of V_O has been noted [99] during an in-situ EPR and PL investigation of ZnO nanostructure. The present PAS results, however, indicates net increase of open volume defects in the system due to annealing at 286 °C. In materials with nanoscale grain size, positrons mostly diffuse and annihilate near the grain surface regions [96-98]. As the average grain sizes of the present samples (~ 70 nm) are of the order of diffusion length of positrons in ZnO (~ 52 nm) [140], it is expected that majority of the positrons annihilate near the grain boundary region. However, careful measurement of positron lifetimes in similar ZnO systems [141] indicates that a fraction of positrons annihilate at small size vacancies in the bulk also. The present experiment indicates that a vacancy migration takes place due to annealing at 286 °C from the bulk towards the grain boundary region. So increase of S -parameter indicates increase of open volume defects in the vicinity of grain surfaces.

To identify the chemical nature of defects near the grain surface, CDBS spectrum has been measured with high statistical accuracy (peak to background ratio $\sim 10^5:1$). The respective ratio curves with respect to ZnO single crystal has been shown in **Figure 4.10**. One can identify two prominent dip like features at $p_L \sim 17.6 \times 10^{-3} m_0c$ and $p_L \sim 26.6 \times 10^{-3} m_0c$. Ratio much lower than 1 in the region above $p_L = 12 \times 10^{-3} m_0c$ indicates significant fraction of positron annihilation in the open volume defects. So dip above $p_L = 12 \times 10^{-3} m_0c$ represents more open volume defects in the sample. Assuming positrons are thermalized before annihilation and using Virial theorem approximation (in the atom the expectation value of the kinetic energy of an electron, E_{kin} , is equal to the binding energy of the electron), one can calculate [142] the E_{kin} using $p_L = (2 m_0 E_{kin})^{1/2}$. In this situation, the two dips correspond to $E_{kin} = 79.2$ eV and 135.4 eV respectively. These two values E_{kin} are very close to the binding energies of zinc 3p and 3s electrons respectively [143]. The published electron binding energy data for Zn 3p_{3/2}, Zn 3p_{1/2} and Zn 3s levels are 88.6 eV and 91.4 eV and 139.8 eV respectively [143]. Another identifiable feature is noticed for $p_L \sim 14.1 \times 10^{-3} m_0c$ which corresponds to $E_{kin} = 50.8$ eV. This is due to annihilation of positrons with the electrons of O-2s atoms with electron binding energy 41.6 eV [143]. This is interesting because isolated V_Os bear generally positive charge in ZnO and are invisible to positrons [96]. Possibility of sensing V_O defects arises when they are part of some neutral or negatively charged defect complexes [144] such as V_{Zn}-V_O, 2V_{Zn}-V_O or V_{Zn}-2V_O types. Clustering of V_{Zn} and V_O defects in the temperature range 182-286 °C is clearly manifested in **Figure 4.10**. This observation is in conformity with the second stage increment of S-parameter as shown in **Figure 4.9**. It can be understood that migration and simultaneous agglomeration [145] of V_{Zn} and V_Os near the grain

boundaries. The lifetime of the defect trapped positrons (as reported earlier [96, 97]) of granular ZnO does not represent annihilation from isolated V_{Zn} s only, rather indicate larger open volumes combining V_{Zn} and V_{O} s. Most recent experiments reveal that when a V_{Zn} is formed in ZnO, appearance of V_{O} in the vicinity is very much likely [144].

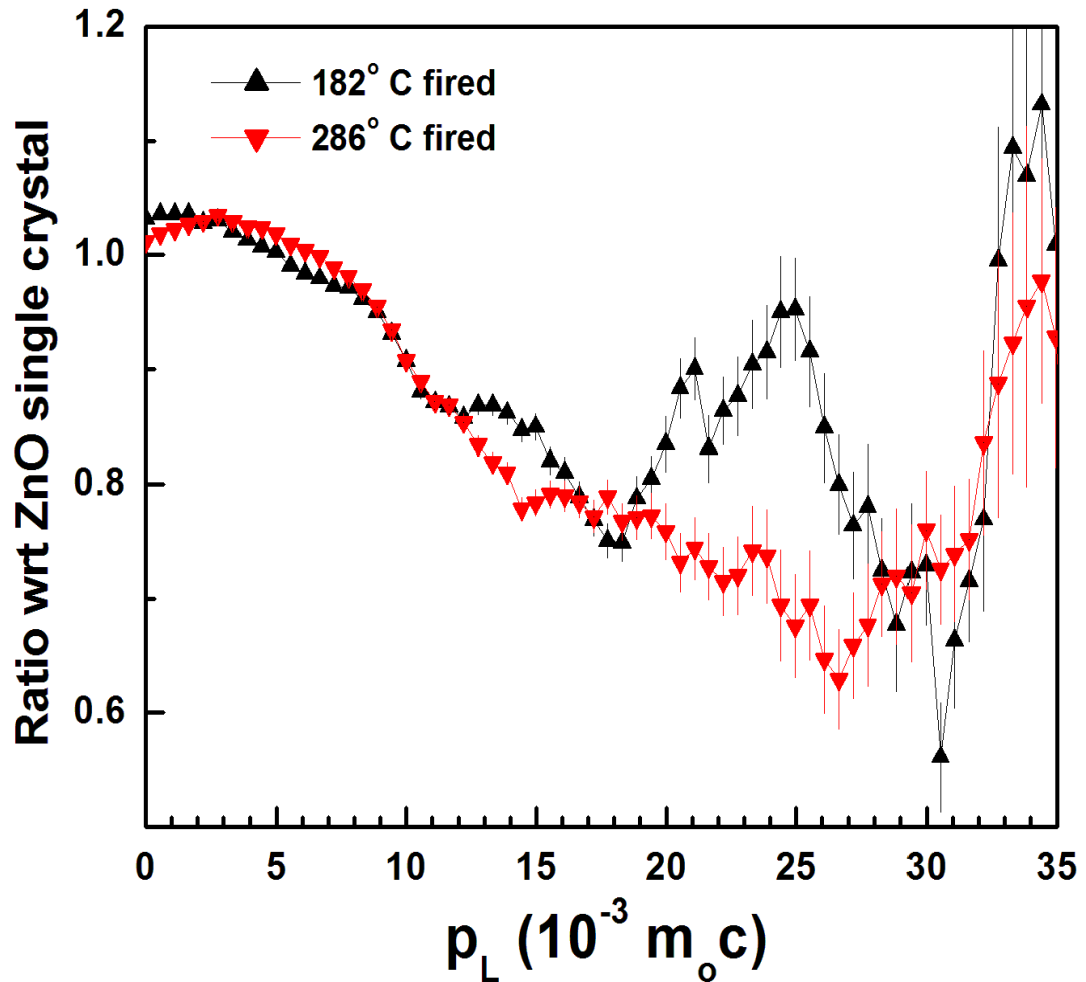


Figure 4.10 Area normalized ratio-curves (constructed from CDB spectrum) for differently annealed ZnO with respect to the ZnO single crystal.

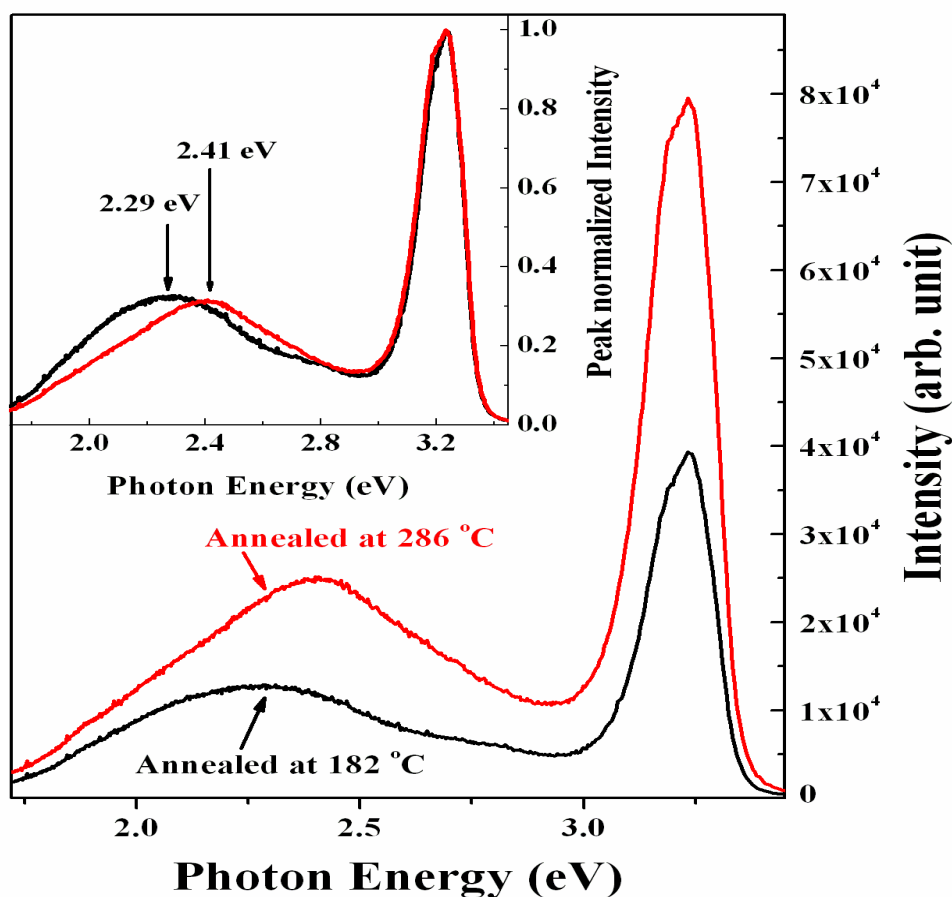


Figure 4.11 PL spectra of the 182 °C and 286 °C annealed ZnO. Inset shows same spectra with NBE peak normalized to 1.

Figure 4.11 represents room temperature (RT) PL spectra of the two samples. Both the samples exhibit near band edge (NBE) at ~ 3.24 eV and broad deep level emissions (DLE). The NBE peak at RT is asymmetric in nature and it is due to an overlapping of free exciton (FX) along with its phonon assisted transitions and defect related emissions which persist up to RT. After annealing at 286 °C, the NBE as well as DLE PL has increased significantly. It can be understood that non-radiative defect sites are partly recovered due to annealing at 286 °C [147]. However, the S -parameter shows an increase (**Figure 4.9**) due to annealing at 286 °C. It is possible that point defects in the grain interior migrate to disordered grain boundary regions and the bulk of the

material become relatively less defective and thereby increasing the overall PL emission. Also the broad DLE peak shifts to higher energy due to annealing at 286 °C (Figure 4.11 inset).

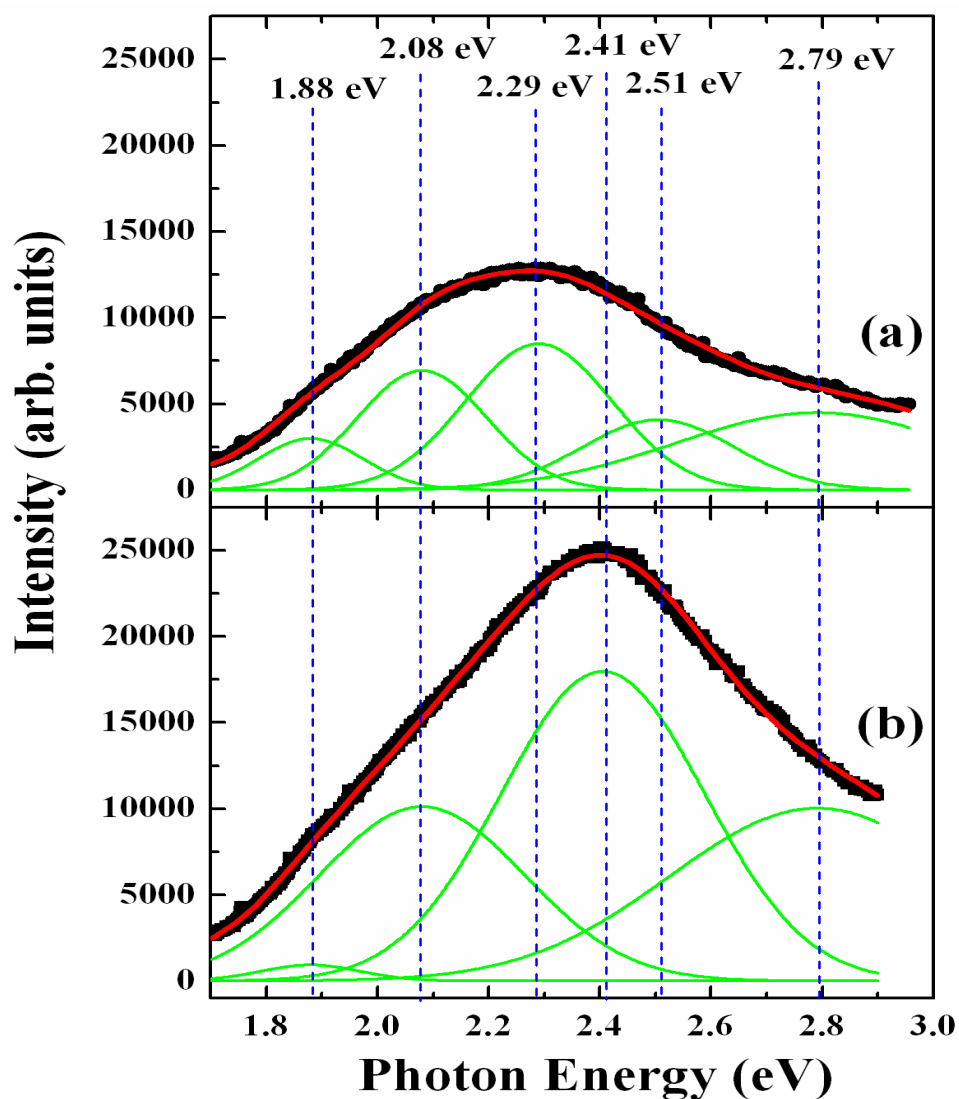


Figure 4.12 Sub-band gap PL emissions from the defect energy levels for (a) 182 °C and (b) 286 °C annealed ZnO samples. Both the spectra have been fitted with several Gaussian peaks.

The deconvolution of possible PL emissions (assuming Gaussian peak shapes) comprising DLE in both the samples has been shown in **Figure 4.12**. The 1.88 eV,

2.08 eV and 2.79 eV peaks can be found in both the samples. PL peak at 1.88 eV exists with very low intensity in the 286 °C annealed sample. The PL emissions at ~ 2.29 eV and 2.51 eV are less probable in the 286 °C annealed sample the spectrum of which bear highest emission weight ~ 2.41 eV. Exactly opposite feature is observed for the 182 °C annealed sample. The PL emission around 2.41 eV in ZnO is generally attributed to the signature of singly ionized oxygen vacancies [98, 148]. The same ~ 2.8 eV is related with zinc interstitial (I_{Zn}) type defects [149]. Thus the increase of PL emissions at 2.41 eV and 2.79 eV for 286 °C annealed sample is consistent with the theoretical prediction [17] and recent experimental results [150] of co-existing I_{Zn} and V_O defects in ZnO. It can also be concluded that V_O generation already takes place below the annealing temperature 286 °C. An in-situ PL monitoring in ZnO nanoparticles has also reported similar result [99]. The 2.51 eV PL emission, which is proposed to be due to V_{Zn} type defects [151], is quenched for the 286 °C annealed sample. The situation is similar for the PL peak ~ 2.29 eV for polycrystalline ZnO [152]. So, three emissions, 1.88 eV, 2.29 eV and 2.51 eV have their origin from V_{Zn} defects or their clusters. Annealing at 286 °C breaks such V_{Zn} defects and opens threefold possibility. The first one is the recovery of a fraction (unknown) of such defects [104]. A part of V_{Zn} defects can club with another V_O to form $V_{Zn}-V_O$ in the bulk [145] which is energetically favorable too [153]. Some of the di-vacancies will migrate to the near surface (grain) defect sink. The probabilities of any of the three processes depend on the requirements of local free energy minimization. The PL emission ~ 2.08 eV has emerged with increased weight in the 286 °C annealed sample spectrum. Earlier, this particular PL peak has been attributed to either I_O or zinc deficient state in ZnO [154, 155]. Without ruling out such possibilities, 2.08 eV PL

emission has been assigned in granular ZnO, observed here, with bulk $V_{Zn}-V_O$ defects to keep track with theoretical prediction and experimental results [153, 156]. This emission can also originate through a radiative emission pathway from doubly positive V_O s which reside in the depletion region of the grain boundaries [146].

Figure 4.13 represents 10 K PL spectra of the 182 °C and 286 °C two samples. In contrast to samples annealed at relatively higher temperatures [157], the PL peak for I_{Zn} related donor bound emission (DBX) at 3.365 eV is very weak in these samples. The most intense peak at 3.311 eV is due to free to bound transition (free electron from conduction band to shallow acceptor states, FA transition) due to some typical V_{Zn} defects [157, 158]. Dominant FA transition is representative of abundant acceptors in ZnO sample. This particular peak shows a significant increase due to 286 °C annealing. The difference of PL intensity (286 °C annealed sample and 182 °C annealed sample) at particular photon energy is shown in the right inset of **Figure 4.13**. The main difference is noticed ~ 3.311 eV. This is interesting as the ratio curve of the 286 °C annealed sample shows much lower ratio above $p_L = 20 \times 10^{-3} m_0c$. It is a clear indication of lower positron annihilation with core electrons of zinc atoms and presence of more V_{Zn} related defects. The exact nature of the acceptor (indeed shallow but localized [158]) contributing to FA transition cannot be identified by PAS or PL data, however, it is clear that certain complex of V_{Zn} s containing V_O as well is involved. The single crystalline ZnO does not show FA PL peak even when artificially V_{Zn} and V_O defects are incorporated [138]. So defects in the vicinity of grain surface are responsible for FA transition. As FA intensity is seen to increase with more V_{Zn} related signal in the ratio curve, one can speculate that $2V_{Zn}-V_O$ defects or $V_{Zn}-V_O$

with a negative charge state is required for FA transition to occur. More investigation on this issue is necessary.

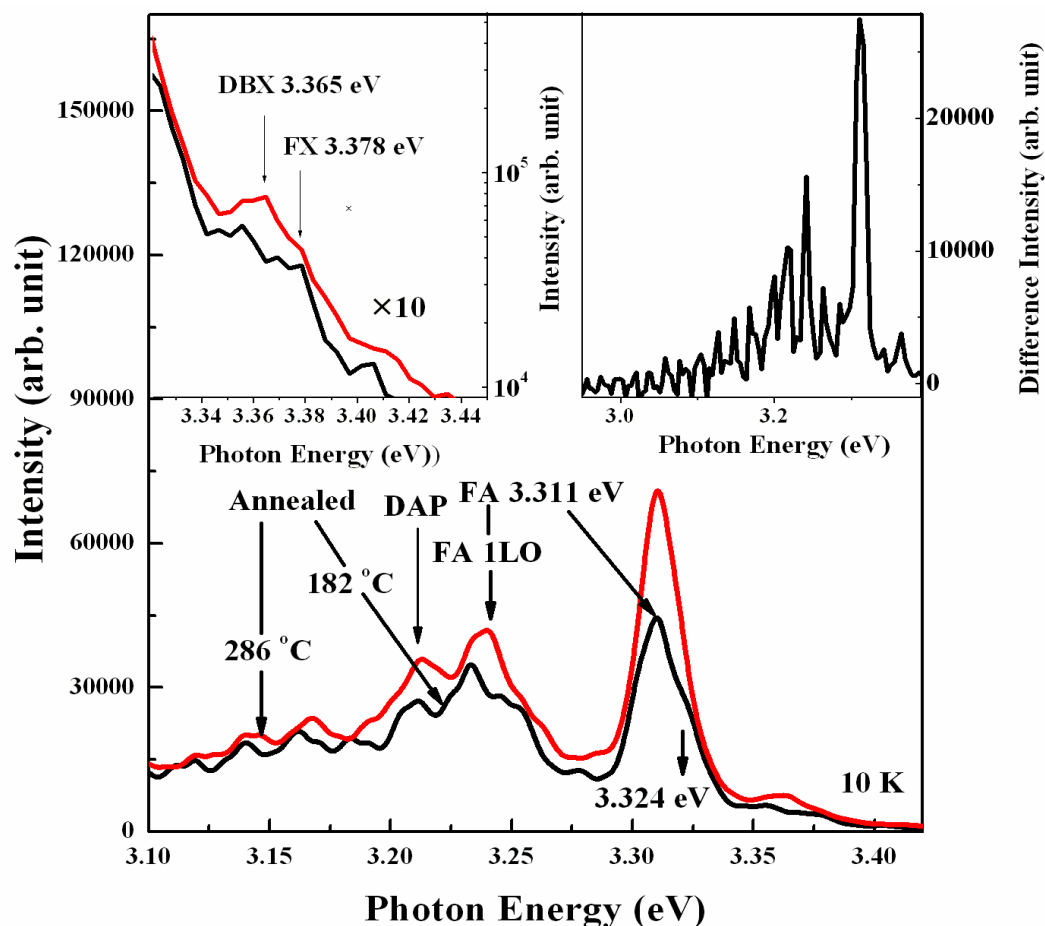


Figure 4.13 10 K PL spectra of both the ZnO samples. Left inset shows the expanded region of 3.32 eV to 3.45 eV. The right inset shows the difference of NBE PL intensities between 286 °C and 182 °C annealed samples. The difference is highest around 3.311 eV.

The other V_{Zn} related emissions such as 2.51 eV and 1.88 eV can be solely due to V_{Zns} or their clusters [151, 159]. As V_{Os} starts to appear in the system, formation of bulk $V_{Zn}-V_{O}$ becomes energetically more favourable and 2.51 eV and 1.88 eV emissions become relatively weak (**Figure 4.13**). Also two other prominent PL peaks are noticeable in the NBE region. Peak at 3.212 eV can be associated with donor

acceptor pair (DAP) luminescence [160]. This is expected to be shallow donor (I_{Zn}) to shallow acceptor transition. Simple calculations [160] of acceptor activation energy (E_A) using the FA and DAP peak energy positions yield 126 ± 10 meV and 209 ± 10 meV, respectively. Both the E_A values are in the range of V_{Zn} related acceptors [104, 160]. Annealing at 286 °C induce more favorable FA and DAP transitions. The other PL peak at 3.324 eV is due to some other type of defects and this emission, along with 3.311 eV PL contributes to the RT NBE spectrum [157]. Altogether, changes of PL properties with annealing of granular ZnO are in conformity with PAS results.

4.6.2 Defect characterization in ZnO annealed at higher temperature

Investigation have been carried out on two granular ZnO samples annealed at 325 °C and 450 °C. Annealing temperatures have been so chosen to unearth annealing of open volume defects containing V_{Zn} and V_{Os} . **Figure 4.14** shows the ratio curve of the two ZnO samples with respect to ZnO single crystal. As mentioned earlier, ratio much lower than 1 in the region above $p_L = 12 \times 10^{-3} m_0c$ indicates significant fraction of positron annihilation in the open volume defects, mostly V_{Zns} . It is also clearly visible that a fraction of vacancy defects present in 325 °C annealed ZnO have recovered due to 450 °C annealing. The concomitant changes in PL have been investigated at low temperature. **Figure 4.15** represents 15 K PL spectra of the two samples. Usual features [138, 157] of ZnO PL at low temperatures have not been discussed here, only the differences of the spectra are highlighted. The PL peaks for donor bound emission (DBX) at 3.365 eV, free exciton (FX) at 3.378 eV and two common donor acceptor pair emissions (DAP) at 3.216 eV and 3.237 eV have been observed for both the samples.

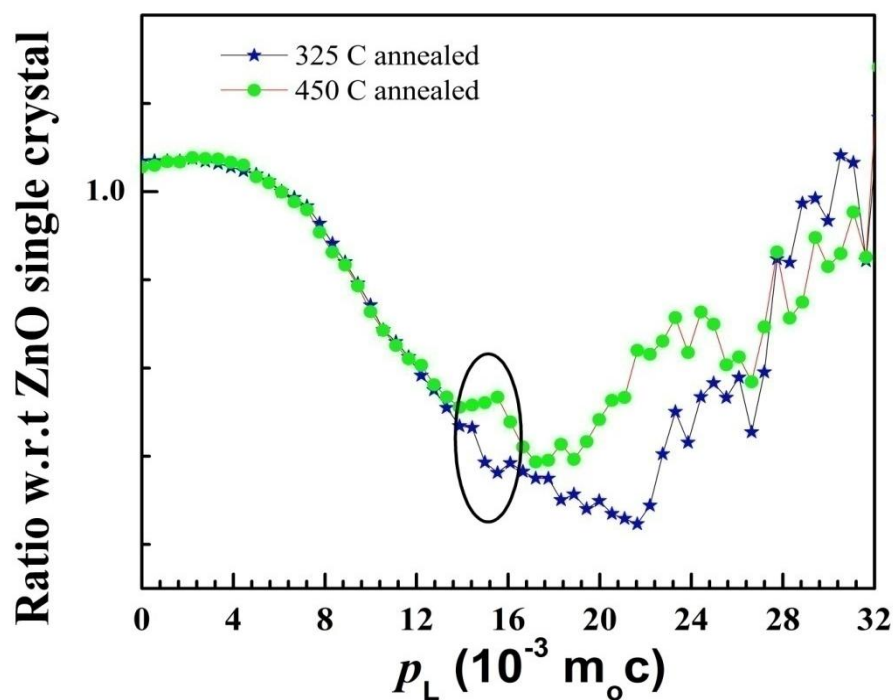


Figure 4.14 Ratio curves of the annealed ZnO with respect to that of the single crystalline ZnO.

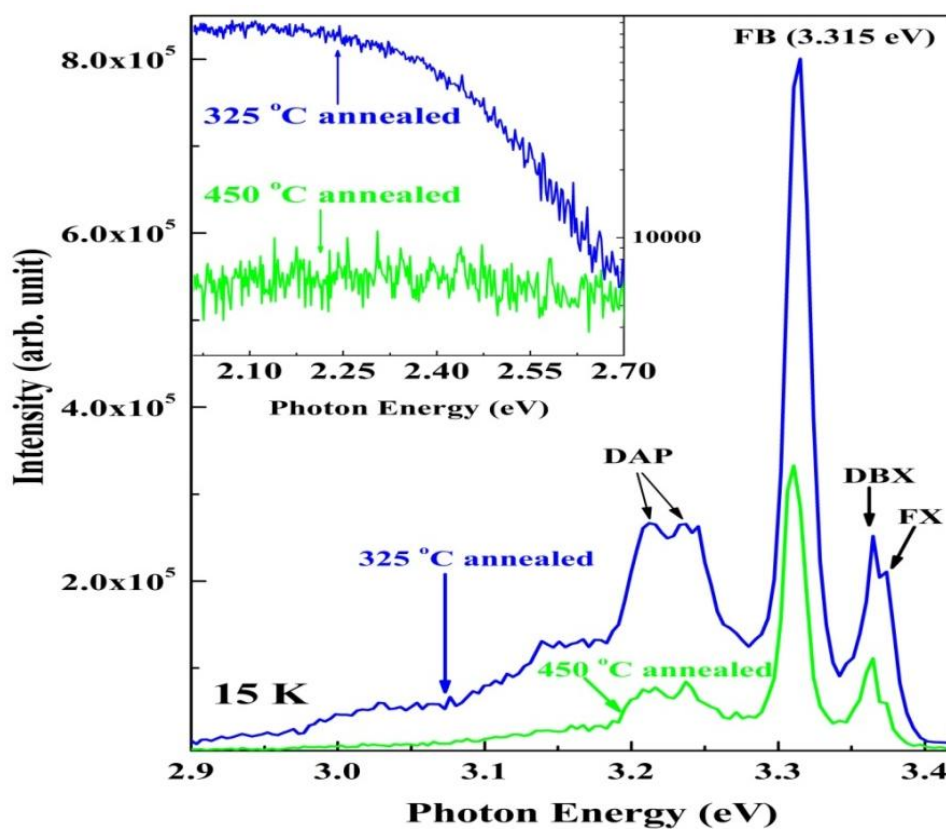


Figure 4.15 Near band edge PL spectrum at 15 K for the 325 °C and 450 °C annealed ZnO. The inset shows the corresponding deep level emissions.

It is interesting that the 325 °C annealed sample with higher defective sites (as probed by PAS) shows overall higher PL emission. It is possible only when scattered defects such as V_{O} s appear in the bulk of the grain for 450 °C annealed sample. Such defects generate fluctuating potentials in the grain interior and there by quenching the overall luminescence. On the contrary, most of the defects in 325 °C annealed samples are segregated near the grain boundaries and grain interiors are relatively defect free yielding more emission. The free electron transition to localized acceptor states (FB transition) is common in poly or nanocrystalline ZnO. It has been reported earlier that such localized acceptors are V_{Zn} s. Here, the FB transition is found at 3.315 eV. Huge reduction of the intensity of FB transition has been found for 450 °C annealing (in fact, if one plots the difference of intensities of PL spectra of the two samples, the main difference between the two spectra comes out to be at 3.315 eV). It can be clearly stated that the origin of FB transition in ZnO is related to V_{Zn} defect clusters as also envisaged earlier [161, 162]. However, it has been found that such clusters contain oxygen vacancies as highlighted in **Figure 4.14** (region inside the ellipse). The recovery of a fraction of defects for 450 °C annealing is clearly observed both by PAS and from the defect level (or deep) PL emission (inset of **Figure 4.15**) of the samples. In our opinion, the outermost layer of the grain surface is highly defective and should be non-luminescent. The inner side of this non-luminescent layer is formed due to vacancy migration from the grain interior and a vacancy decoration, which is energetically favorable from local free energy consideration, appears in the crystal. One of such defects has been claimed as basal plane stacking faults [161, 162]. It can only be inferred that both V_{Zn} and V_{O} exist in the core of such defects and the defective zone is luminescent in nature. Any perturbation by irradiation [157] or annealing [163] which

can recover the V_{Zn} part of such vacancy decoration reduces 3.315 eV PL of ZnO. More investigation on this agenda is necessary.

4.7 Conclusion

Ab-initio calculations under density functional theory predict that a significant amount of magnetic moment gets generated into the ZnO just by doping various p-block elements. The primary sources of magnetism are the p-orbital electrons of dopant atom and a small contribution comes from the neighboring O-atoms present around the dopant. The spin-spin interactions study reveals that B, C, N, Si, P, Ge and As atom doped system has lower ground state free energy for ferromagnetic ordered system over anti-ferromagnetic ordered system. The theoretical predictions are found in harmony with experimental observations for boron ions irradiated/implanted ZnO system. The formation of defects has been studied explicitly in ZnO samples at various temperature by employing both in-situ and ex-situ positron annihilation technique. The PAS studies reveals that the carbon and loosely bounds hydroxyl bound species get removed around from the sample when heated ~90 minutes at 180 °C. Further annealing the sample at 286 °C leads to the formation of vacancies in the form of clusters and pairs (such as $V_{Zn}-V_O$, $2V_{Zn}-V_O$ or $V_{Zn}-2V_O$ types) and also the vacancy migration and agglomeration. The PL measurements also indicate the formation of vacancy in the granular ZnO sample. It has also been observed that due to annealing temperature difference of 125 °C (from 325 °C to 450 °C), huge change occurs in low temperature photoluminescence (PL) of ZnO. Significant reduction of free to bound (FB) transition ~ 3.315 eV is observed for increasing the annealing temperature. It has been conjectured that ~ 3.315 eV PL in ZnO is related to particular decoration (unknown) of both Zn and O vacancies.

Chapter-5

Defect induced ferromagnetism in SnO₂

5.1 Introduction

SnO₂ is a wide band-gap semiconductor with band gap of 3.6 eV [164]. Punnoose *et al.*, reported room temperature ferromagnetism in SnO₂ and paramagnetism in SnO after doping iron at different concentrations [76]. They further reported room temperature ferromagnetism in chemically synthesized Co-doped SnO₂ nanoparticles [165]. Hong *et al.*, observed ferromagnetism in laser ablated undoped SnO₂ thin films grown on the LaAlO₃ substrate at room temperature [92]. The reason behind the ferromagnetic ordering is conjectured either by oxygen vacancy or by Sn vacancy [92]. However, it has been shown both theoretically as well as experimentally that very high order of room temperature ferromagnetism can be induced by creating Sn vacancies into the pristine SnO₂ sample [93]. Albanese *et al.*, [166] detected a strong electron paramagnetic resonance (EPR) signal in nitrogen doped SnO₂. The paramagnetic property observed by nitrogen doping was found to be consistent with the first principle calculation [166]. Despite of all these studies in SnO₂, there is no clear understanding of magnetic property in p-block elements doped SnO₂ system.

In the present work, ab-initio calculations under the framework of density functional theory have been performed to understand the magnetic properties of SnO₂. Possibilities of ferromagnetism in SnO₂ have been studied after subsequently doping different p-block elements (B, C, N, Al, Si, P, S, Ga, Ge, As) at oxygen site and also

for atomic vacancies (V_{Sn} and V_{O}). Two different doping distances have been considered to dope the p-block elements for complete understanding of the process.

5.2 Computational Methodology

Vienna *ab-initio* simulation (VASP) code [120-123], along with the MedeA software package has been used for the theoretical calculation based on density functional theory (DFT). The generalized gradient approximation (GGA) with Perdew-Burke-Ernzerhof (PBE) exchange and correlation [124] method has been followed to study all the systems. A super cell with a size of $2 \times 2 \times 3$ tetragonal structured unit cells, i.e., with 72 atoms has been taken for all the calculations as shown in **Figure 5.1**. The optimized lattice parameters for SnO_2 unit cell are $a = b = 4.736 \text{ \AA}$ and $c = 3.186 \text{ \AA}$ (close to the experimental values [167] $a = b = 4.738 \text{ \AA}$; $c = 3.186 \text{ \AA}$) and $\alpha = \beta = \gamma = 90^\circ$. Periodic boundary conditions have been introduced along all the basis vectors. Two oxygen atoms in the pristine SnO_2 super-cell have been substituted systematically by $X = \text{B, C, N, Al, Si, P, S, Ga, Ge}$ and As atom (i.e., $\text{Sn}_{24}\text{X}_2\text{O}_{46}$). Each structure has been geometrically relaxed until the maximum value of the unbalanced inter-atomic force component (Hellman-Feynman force) converged to values below 0.02 eV/\AA . The spin polarized density of states has been calculated for each optimized structure using density functional theory and hence the induced magnetic moment, free energy and Fermi energy for the system have been calculated. In all calculations, 400 eV mesh cut-off energy has been taken into account to expand the plane wave basis set, and 10^{-5} eV tolerance has been fixed as stopping criteria of the self-consistent loop to reach the electronic ground state. The Brillouin zone (BZ) of the super cells has been divided by $3 \times 3 \times 3$ Monkhorst-Pack (MP) k-points [125].

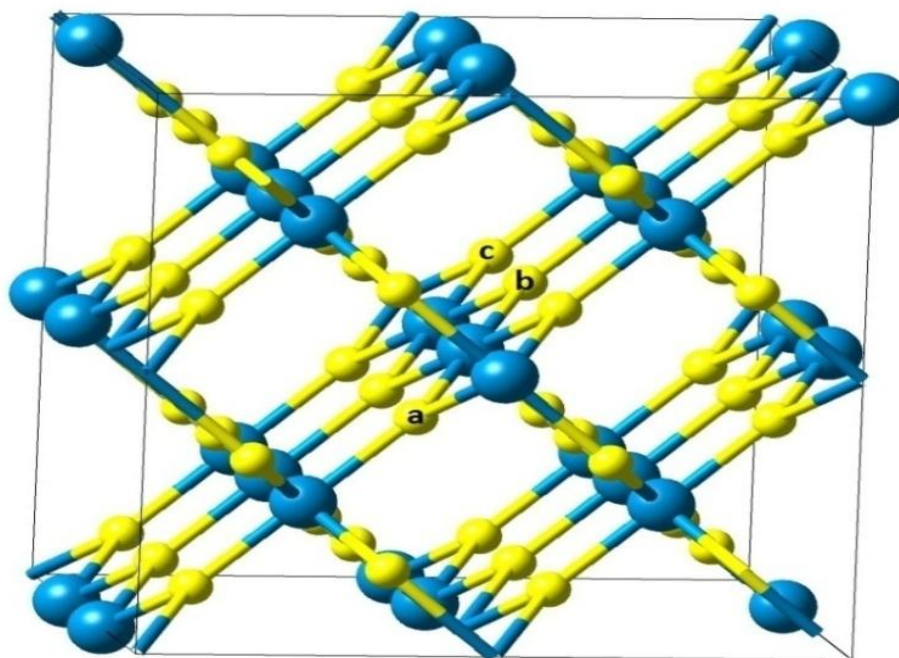


Figure 5.1 Super-cell of pristine SnO_2 with $2 \times 2 \times 3$ unit cell, the blue color spheres are the Sn atoms and yellow color spheres are O atoms. The (a, b) and (a, c) positions are chosen for short distance doping and long distance doping respectively.

In the super-cell, two atoms of same p-block element have been doped at two oxygen sites present in adjacent unit cells. Distance between two dopants is $\sim 4\text{\AA}$, marked as position (a, b) in **Figure 5.1**. Similarly for long distance doping, two oxygen atoms in the super-cell separated by a distance $\sim 7\text{\AA}$, labelled as (a, c) have been chosen. Spin-spin interaction calculations have been carried out to study the magnetic coupling (ferromagnetic or anti-ferromagnetic). The ferromagnetic ordering has been achieved by aligning all the spins (dopant as well as the nearby oxygen atoms) in same direction. The spin contribution of the Sn atom and the remaining oxygen atoms are either negligibly small or zero. On the other hand, G-type anti-ferromagnetic ground state has been attained by aligning the spins of two dopants as well as the nearby oxygen atoms in anti-parallel direction. The ground state free

energy of both ferromagnetic state and anti-ferromagnetic state has been compared to know the favored state in all $\text{Sn}_{24}\text{X}_2\text{O}_{46}$ cases. Local magnetic density distribution has been calculated for spin polarized configuration.

5.3 Ferromagnetism in p-block elements doped SnO_2

Theoretical calculations under the framework of density functional theory have been carried out to study magnetic properties in different SnO_2 systems. Pristine SnO_2 when doped with some p-block elements at oxygen site generate a significant amount of magnetic moment. The amount of magnetic moment induced in various p-block elements doped SnO_2 system and SnO_2 with V_{Sn} or V_{O} is shown in **Figure 5.2**. B, N, P and As when doped at two different oxygen sites in pristine SnO_2 system produce a magnetic moment of $2 \mu_{\text{B}}$, $1.9 \mu_{\text{B}}$, $2 \mu_{\text{B}}$ and $2 \mu_{\text{B}}$ respectively. The p-orbital electrons of dopants along with neighboring oxygen and tin atoms are the main source of magnetization in the system. However, the other p-block elements (C, Al, Si, S, Ga, Ge) do not produce any significant magnetic moment in $\text{Sn}_{24}\text{X}_2\text{O}_{46}$ system. Two different doping distances have been chosen to study the spin-spin interactions in the system. The optimized doping distance, defect formation energy and change in Fermi energy after doping are tabulated in Table 1. The creation of one cationic vacancy (V_{Sn}) generates a moment of $\sim 3.7 \mu_{\text{B}}$ but no significant moment is found for anionic vacancy (V_{O}). Spin-spin interactions study shows that stable ferromagnetism is obtained only for short distance P and As doped systems. The optimized distance between two P and As atoms doped at short position are calculated to be 4.4 \AA and 4.6 \AA respectively. The difference of ground state energy between parallel and anti-parallel spin ordered systems for B, N, P and As doped at long as well as short position are calculated and plotted in **Figure 5.3**. The difference in ground state free

energy between ferromagnetic spin ordered system and anti-ferromagnetic system is found to be - 404.4 meV and - 277.5 meV for phosphorus and arsenic doped SnO₂.

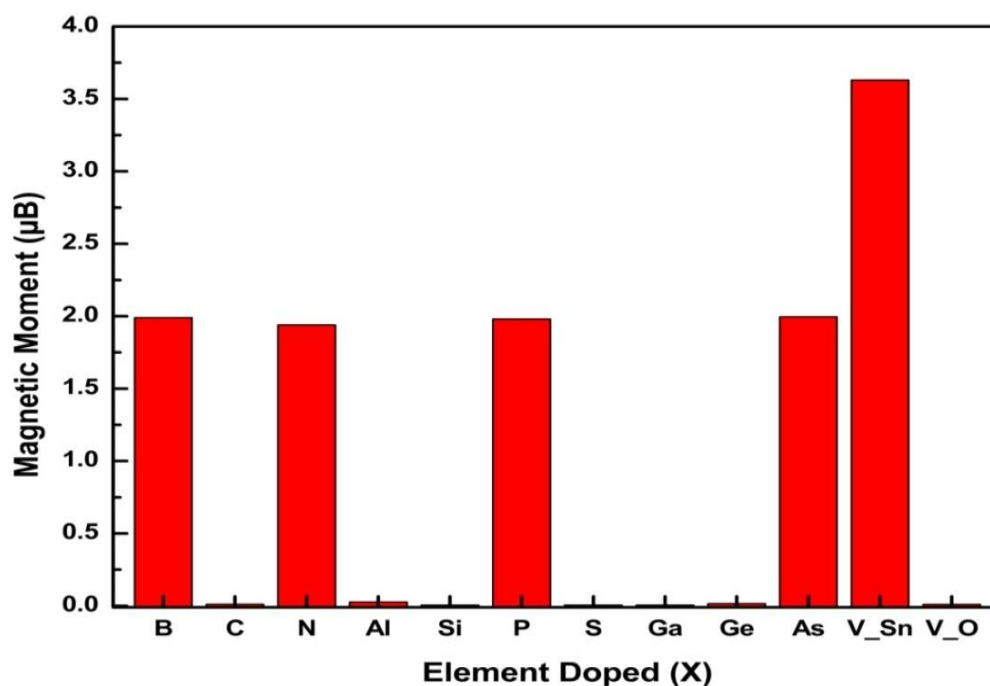


Figure 5.2 Induced magnetic moment in p-block elements doped Sn₂₄X₂O₄₆ (X = B, C, N, Al, Si, P, S, Ga, Ge, As) system & SnO₂ system with single V_{Sn} and V_O.

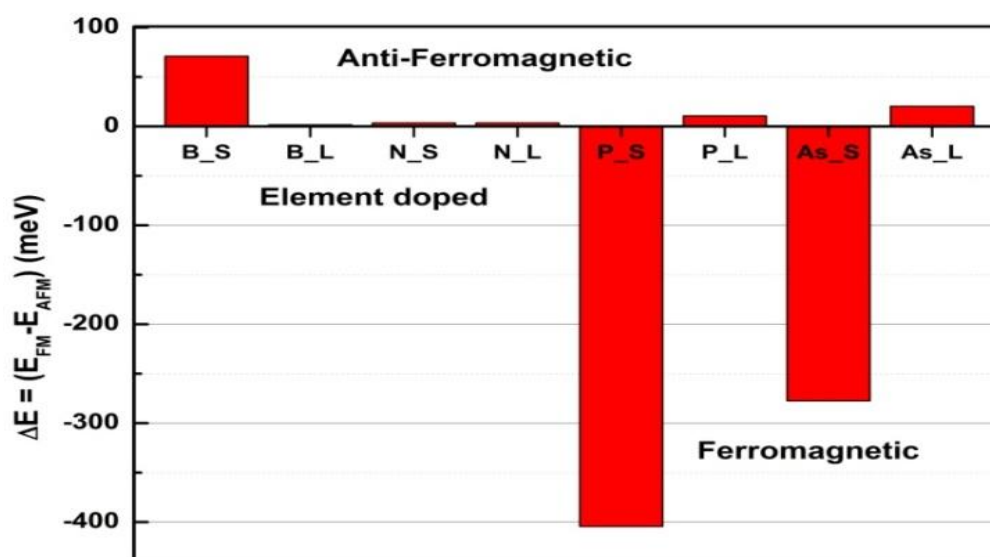


Figure 5.3 Difference of ground state energy between ferromagnetic and anti-ferromagnetic system for B, N, P and As doped SnO₂. 'S' denotes short position and 'L' denotes long position doping.

Table 5.1 Optimized doping distance, induced magnetic moment, Fermi energy shift and defect formation energy for two B, N, P and As doped at short and long position in SnO₂.

Doped element	Optimized distance (Å)	Induced Magnetic Moment (μ_B)	Fermi Energy shift (eV)	Defect Formation Energy (eV)
B	4.52	1.99	0.70	17.019
	7.01	1.8		17.019
N	4.13	1.94	-0.18	2.606
	6.19	1.94		2.606
P	4.55	1.98	1.15	14.471
	6.64	1.98		14.470
As	4.68	1.99	1.68	17.903
	6.49	1.99		17.882

The spin polarized total density of states (DOS) for all p-block element doped system has been plotted and a comparison is made as shown in **Figure 5.4**. From **Figure 5.4** it can be seen that the total density of states is perfectly symmetric for pristine SnO₂, C, Al, Si, S, Ga and Ge doped SnO₂ system. This symmetry indicates the presence of equal number of up-spin electrons and down spin electrons in the system; as a result, no net magnetic moment is found in these systems. But in case of B, N, P and As doped system, the total density of states plot has asymmetrical nature. This clearly indicates there is discrepancy in number of up-spin electrons and down-spin electrons in these systems which confirm the existence of some unpaired electrons in the system. The presence of unpaired electrons gives rise to magnetic moment in the system. However, from spin-spin interaction study, it has been known that only P and As doped SnO₂ system favors ferromagnetic coupling.

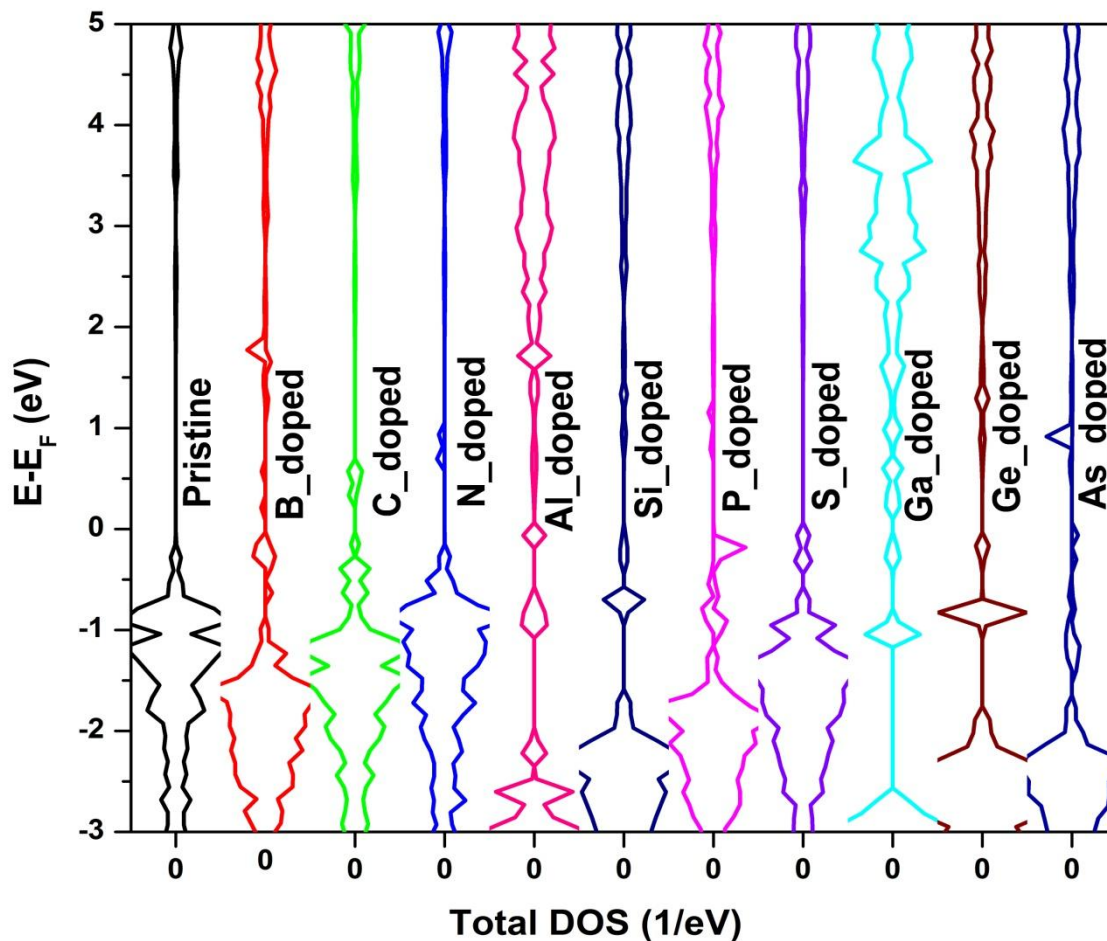


Figure 5.4 Comparison of total density of states for p-block elements doped SnO₂.

The partial DOS and total DOS for P atom doped SnO₂ and As doped SnO₂ system have been plotted in **Figure 5.5** (a) and **Figure 5.5** (b) respectively. It can be observed that both the system have asymmetrical partial DOS. The primary source of magnetic moment in these systems is the valence orbital electrons of the dopant atom and a small contribution comes from neighboring Sn and O atoms. The strong coupling of p-orbital electrons of dopant atom and oxygen atom can be observed from the asymmetry of states around the Fermi level. The doping of both phosphorus atom as well as arsenic atom at oxygen site makes the SnO₂ system n-type as the Fermi level shifts towards conduction band by an amount 1.15eV and 1.68eV respectively.

The local magnetic density distribution in P doped and As doped SnO₂ system is shown in **Figure 5.6** (a) and **Figure 5.6** (b) respectively.

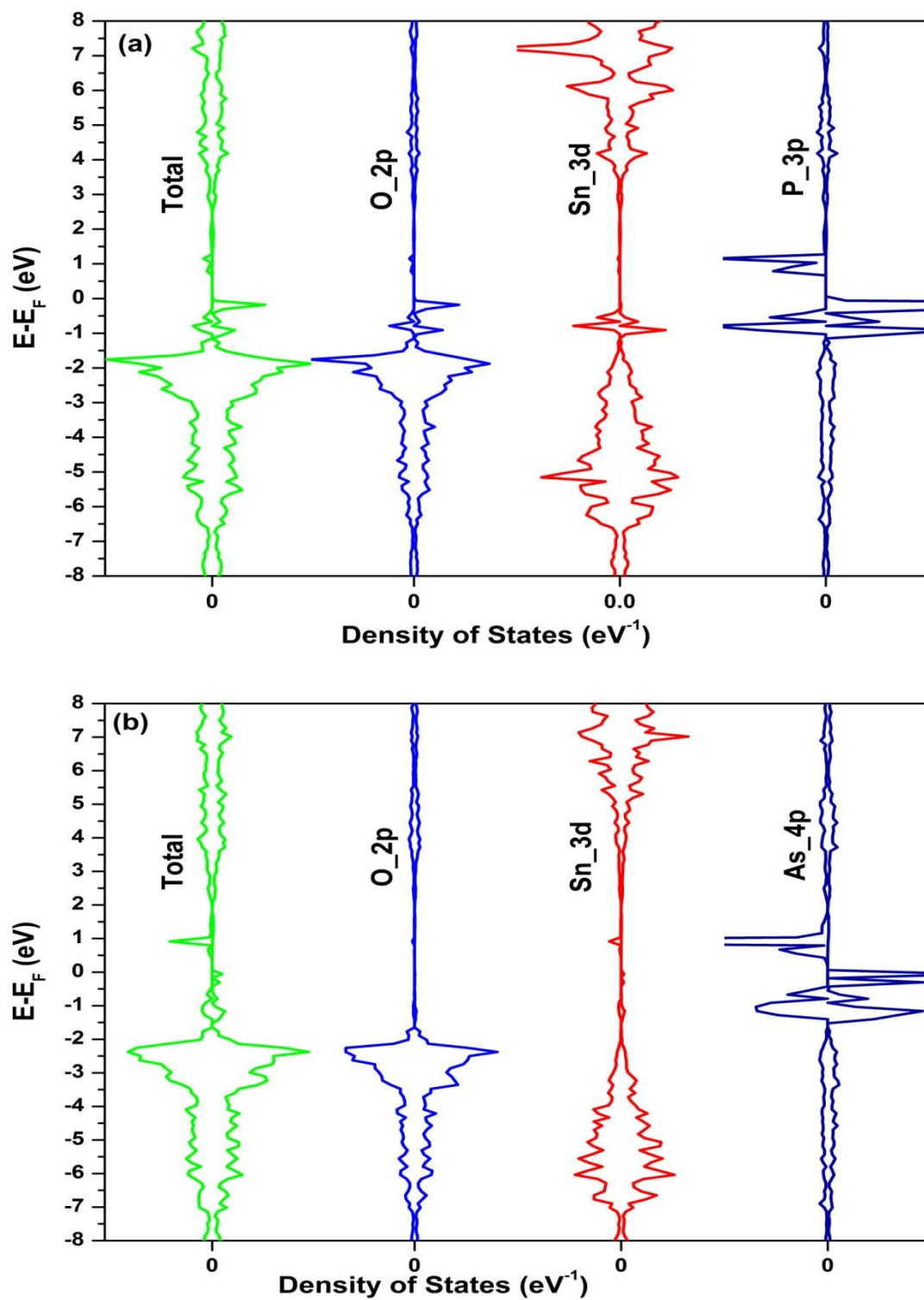


Figure 5.5 Spin polarized density of states for a) P doped SnO₂; b) As doped SnO₂.

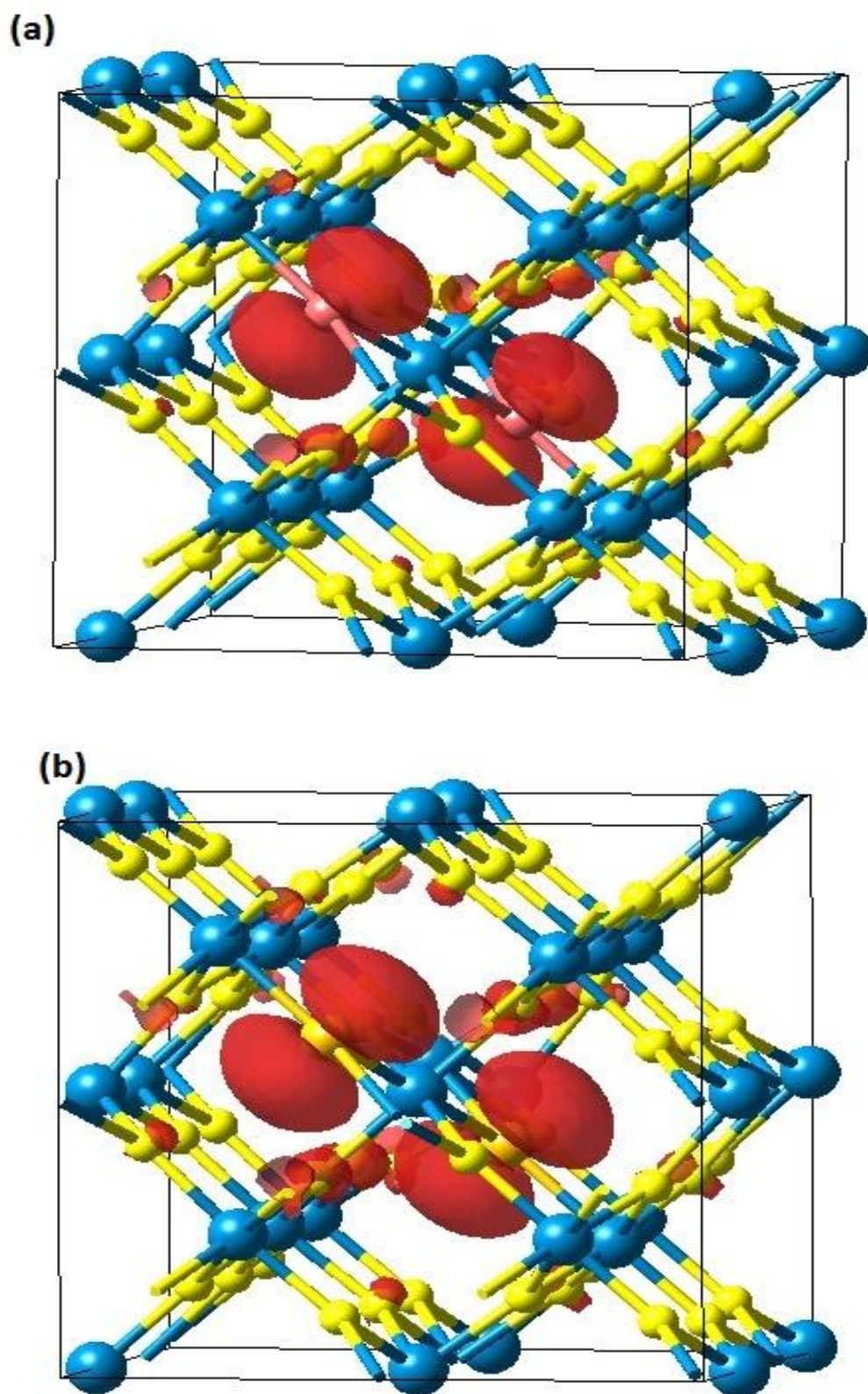


Figure 5.6 Local magnetic density distributions in SnO_2 system with a) two P atoms doped at short position and b) two As atoms doped at short position.

It is clear from the local magnetic density distribution (the red color cloud around the dopant) that the magnetic moment is primarily localized around the dopants and a small amount of distribution is present around the neighboring oxygen atoms. The results of local magnetic distribution calculation support the outcome from density of states calculation. Both the calculation depicts the dopants as the main source of induced magnetic moment in SnO₂ system. The defect formation energy for all the p-block elements doped system has been calculated using equation (16) [80, 127].

$$E_{df}(X) = E(\text{Sn}_{24}\text{X}_2\text{O}_{46}) - E(\text{SnO}_2)_{24} + 2E(\text{O}) - 2E(\text{X}) \dots\dots\dots (16)$$

Where, $E_{df}(X)$ is the defect formation energy, $E(\text{Sn}_{24}\text{X}_2\text{O}_{46})$ is the free energy of system under consideration, $E(\text{SnO}_2)_{24}$ is the free energy of pristine SnO₂, $E(\text{O})$ is the free energy of isolated oxygen atom and $E(\text{X})$ is the free energy of isolated atom of the dopant. The defect formation energy of two P doped SnO₂ and two As doped SnO₂ systems has been found to be 14.5 eV and 17.9 eV respectively. It is interesting to note that two nitrogen atom doping in SnO₂ has only 2.6 eV defect formation energy. Also, nitrogen doped at oxygen site makes the SnO₂ system a p-type semiconductor as the Fermi level shifts towards the valance band by an amount of 0.18 eV which is also in agreement with earlier studies [168, 169].

5.4 Conclusion

Magnetic properties of SnO₂ has been theoretically studied by systematically doping of various p-block elements (viz., B, C, N, Al, Si, P, S, Ga, Ge, As) at oxygen site. Density functional theory has been applied to calculate the spin polarized density of states, magnetic moment in all the systems. A significant amount of magnetic moment has been found in B, N, P and As doped SnO₂ systems. However, spin-spin interactions study reveals that only P and As doped SnO₂ system produced stable ferromagnetic spin ordering at ground state. In all other cases (i.e., B, C, N, Al, Si, S, Ga, Ge), either the spin-spin coupling is very weak or anti-ferromagnetic coupling dominates in Sn₂₄X₂O₄₆ system. The primary source of magnetism in all the cases is the p-orbital electrons of the dopant atom along with nearby oxygen atoms. The ferromagnetic property in phosphorus and arsenic doping in SnO₂ has been found for the first time. The value of induced magnetic moment for both phosphorus as well as arsenic doped at oxygen site in SnO₂ system is found to be $\sim 1\mu_B$ per dopant. This property of ferromagnetic ordering in SnO₂ system can be used for spintronics applications in future.

Chapter-6

Conclusion and future outlook

6.1 Conclusion

Room temperature ferromagnetism has been studied in different semiconducting oxides both theoretically and experimentally. Theoretical calculations have been carried out under the framework of density functional theory to study magnetic properties in different oxide systems (viz. TiO_2 , ZnO and SnO_2). The outcome of DFT based calculations have been analyzed to predict the magnetic property by creating defects (both atomic vacancies and doping) into the oxide systems. Different samples were prepared using ion beam irradiation techniques. The vacancies generated in the samples have been characterized using Positron annihilation spectroscopy (both lifetime measurement technique and coincidence Doppler broadening technique have been employed) and photoluminescence spectroscopy. The magnetic behaviors in the sample have been characterized using SQUID magnetometer.

Various p-block elements which are nonmagnetic in nature have been doped at oxygen site in above mentioned three oxides. A significant amount of magnetic moment is found in these systems for most of the cases. The source of magnetism has been found to be the valence orbital electrons of the dopants (i.e. p-orbital electrons). A small amount of magnetic contribution comes from the oxygen atoms in the neighborhood of the dopant. It is interesting to note that in these systems, neither there are partially filled d-orbital electrons nor the magnetic contribution comes from d-

orbital electrons; rather the magnetism is observed without having any unpaired electrons in the d-orbital in any of the atoms present in these systems. This kind of unique magnetic behavior is known as d^0 magnetism (as discussed in chapter 1). Here, it has found that the oxide systems under study (TiO_2 , ZnO and SnO_2) shows d^0 magnetism on doping with most of the p-block elements.

In TiO_2 , a stable magnetic moment can be generated by doping B, C, N, Al, Si, P and As at oxygen site. However, after spin-spin interaction studies, it has been found that only B, C, N, Si, P and As doped system favors ferromagnetic coupling. Doping of p-block element at Ti-site does not produce any magnetic effect in TiO_2 system. Similarly, in ZnO , doping of B, C, N, Si, P, Ge and As doped at O-site produced stable magnetic moment and also the ferromagnetic ground state is more stable in all cases. However, in case of SnO_2 only B, P and As doped system produced magnetic moment. Among them, only P and As doped system have lower ground state free energy for ferromagnetic system over that of anti-ferromagnetic one. It has also been found that generation at both atomic vacancies (i.e. V_{Ti} and V_{O}) can produce magnetism in TiO_2 . In the case of Ti vacancy, the nearest O-atoms become O^- from O^{2-} which leaves one unpaired electron in the atom. Thus, p-electrons of neighboring oxygen atoms are mainly responsible for magnetization in the system. Similarly, in the case of O vacancy a single oxygen vacancy in TiO_2 supplies two extra electrons to the nearest Ti ions, which has been shared by the two nearest Ti ions and hence the Ti^{4+} (empty 3d state) becomes Ti^{3+} (one 3d electron). This single 3d electron of the Ti^{3+} plays a major role in introducing ferromagnetic ordering of the system.

Experimentally, stable room temperature ferromagnetic behavior has been observed in TiO_2 with atomic vacancies. 96 MeV O^{8+} ion beam has been irradiated on

TiO₂ sample to create enough atomic vacancies. The PAS characterization reveals the creation of large number of Ti vacancies in the irradiated sample. The magnetic measurement shows ferromagnetism in the irradiated sample at room temperature. Similarly, experimental evidence of room temperature ferromagnetism has been found for 1.2 MeV C⁴⁺ and 50 k eV N⁴⁺ ions irradiated TiO₂ sample. The observed values saturation magnetizations are greater than the earlier reported values, where the source of magnetism is oxygen vacancies. The increase in magnetization can be associated with the dopant atoms sitting at the O-site in both the samples.

Room temperature ferromagnetism has been also observed in 10 k eV B⁺ ions beam irradiated TiO₂ and ZnO samples. DFT based calculations predicts ferromagnetism in both the samples on doping of B-atoms at O-site. The primary source of magnetism in both the cases is found to be the 2p orbital electrons of boron along with a small contribution from 2p orbital electrons of oxygen atom in the neighborhood of the dopant. However, the induced magnetic moment in TiO₂ and SnO₂ is $\sim 1 \mu_B$ per dopant, whereas for ZnO it is about $3\mu_B$. This discrepancy can be understood from the fact that boron atom has the electronic configuration of $2s^2, 2p^1$ in its valence shell. When oxygen gets substituted by boron atom, it pulls the electrons from the neighboring metal ion as the electro negativity of boron is 2.04. There is a transfer of two electrons towards boron atom from neighboring metal ion which makes the electronic configuration of the boron atom $2s^2, 2p^3$ in its valence shell. Thus leaves three unpaired electrons in the boron atom inside the oxide system. These unpaired electrons in 2p orbital of boron generate $\sim 3\mu_B$ magnetic moment per boron atom doping for ZnO. However, in case of SnO₂ and TiO₂, extra oxygen (with electro negativity 3.44) attached with the metal ion. The oxygen atom pulls more electron

cloud towards itself and boron atom pulls fewer electrons as compared to the case of ZnO system. This leads to the generation of less magnetic moment in the TiO₂ and SnO₂ systems.

The generation of atomic vacancies has been crucial in ZnO system. Unambiguous identification of defects present in semiconducting oxides is extremely important to explain defect induced modification of photoluminescence, conductivity, magnetism, catalytic efficiency and several others. In-situ Doppler broadening of electron positron annihilated γ -ray line shape measurement for granular ZnO material shows interesting changes in the *S*-parameter when temperature is increased above room temperature. Annealing at steady temperatures, 182 °C and 286 °C, *S*-parameter increases with time but tends to saturate in a time scale ~ 90 minutes. The first phase of *S*-parameter increase has been understood as removal of carbon and loosely bound hydroxyl groups. Vacancy migration and agglomeration related increase of *S*-parameter has been observed during 286 °C annealing. Off-line PL measurements of samples annealed at 182 °C and 286 °C (similar time scale as in in-situ experiment) show drastic changes of defect level emissions at room temperature. Clear evolution of 2.41 eV PL emission in 286 °C annealed sample is observed which indicates the presence of stable oxygen vacancies. Agglomeration of a fraction of zinc and oxygen vacancies can be responsible for the increase of open volume defects and the *S*-parameter. Most probable origin of 2.08 eV PL emission in granular ZnO is from zinc-oxygen divacancies. 10 K PL spectra of the samples show huge increase of 3.311 eV PL emission in 286 °C annealed sample. In the light of the previous reports on this topic, it is clear that 3.311 eV PL emission in ZnO arise from defects. The particular defect center is a typical decoration of vacancies (with a core of both zinc and oxygen

vacancy) near the grain boundary region. The defects generation in granular ZnO has been further studied by annealing the samples at two different temperatures (325 °C and 450 °C). Ratio curve analysis shows that granular ZnO samples contain both Zn and O vacancies. Such defects exist as agglomerates of several vacancies and start to recover above 400 °C annealing. It has also been observed that due to annealing temperature difference of 125 °C (from 325 °C to 450 °C), huge change occurs in low temperature photoluminescence (PL) of ZnO. The widely discussed free to bound transition in ZnO (~ 3.315 eV at 15 K) has been correlated with presence of open volume defects in the system.

6.2 Future prospect

Both theoretical calculations and experimental observations show room temperature ferromagnetism in various semiconducting materials. However, it has been observed that most of dopants give rise to n-type conductivity in addition to ferromagnetic property in these semiconductors. RTFM along with p-type semiconducting property is vital for spintronics application in these oxide materials. Further studies in the search of RTFM in p-type direct band gap semiconductors may lead to the realization of new class of devices in future.

Bibliography

1. M. Venkatesan, C. B. Fitzgerald and J. M. D. Coey, *Nature Commun.* **430** (2004) 630.
2. T. Dietl, *Nature Mater.* **9** (2010) 965.
3. S. Bhatti, R. Sbiaa, A. Hirohata, H. Ohno, S. Fukami, S. N. Piramanyagam, *Mat. Today*, **20** (2017) 530-548.
4. K. Ando, *Science*. **312** (2006) 1883-1885.
5. I. Zutic, J. Fabian and S. D. Sarma, *Rev. Mod. Phys.*, **76** (2004) 323.
6. G. A. Medvedkin, T. Ishibashi, T. Nishi and K Hayata, *Jpn. J. Appl. Phys.*, **39** (2000) L949.
7. S. D. Sarma, *American Scientist*, **89** (2001) 516.
8. S. Das. Sarma, J. Fabian, X.Hu and I. Zutic, *Solid State Comm*, **119**(2001) 207.
9. T. Dietl, H. Ohno, F. Matsukura, J. Cibert and D. Ferrand, *Science* **287** 1019 (2000).
10. A. Haury, A. Wasiela, A. Arnoult, J. Cibert, S. Tatarenko, T. Dietl and Y. Merled'Aubigne, *Phys. Rev. Lett.* **79** (1997) 511.
11. P. Sharma, A. Gupta, K. V. Rao, J. O. Frank, R. Sharma, R. Ahuja, J. M. O. Guillen, B. Johansson and G. A. Gehring, *Nature Mater.* **2** (2003) 673-677.
12. K. Ueda, H. Tabata and T. Kawai, *Appl Phys. Lett.* **79** (2001) 988-990.
13. J. Blasco, F. Bartolome, L. M. Garcia and J. Garcia, *J. Mater. Chem.* **16** (2006) 2282-2288.
14. S. Hu, S. Yan, M. Zhao and L. Mei, *Phys. Rev. B* **73** (2006) 245205.
15. D. Iusan, B. Sanyal and O. Eriksson, *Phys. Rev. B* **74** (2006) 235208.

16. A. M. Nazmul, S. Sugahara and M. Tanaka, *Phys. Rev. B* **67** (2003) 241308(R).
17. A. Punnoose, J. Hays, A. Thurber, M. H. Engelhard, R. K. Kukkadapu, C. Wang, V. Shutthanandan and S. Thevuthasan, *Phys. Rev B* **72** (2005) 054402.
18. S. Ramachandran, A. Tiwari, J. Narayan and J.T. Prater, *Appl. Phys. Lett.* **87** (2005) 172502.
19. S. X. Zhang, S. B. Ogale, L. F. Fu, S. Dhar, D. C. Kundaliya, W. Ramagan, N. D. Browning, T. Venkatesan, *Appl. Phys. Lett.* **88** (2006) 012513.
20. G. T. Thaler, M. E. Overberg, B. Gila, R. Frazier, C. R. Abernathy, S. J. Pearton, J. S. Lee, S. Y. Lee, Y. D. Park, Z. G. Khim, J. Kim and F. Ren, *Appl. Phys. Lett.*, **80** (2002) 3964.
21. S. J. Pearton, C. R. Abernathy, M. E. Overberg, G. T. Thaler, and D. P. Norton, *J. Appl. Phys.*, **93** (2003) 1.
22. R. J. Green, D. W. Boukhvalov, E. Z. Kurmaev, L. D. Finkelstein, H. W. Ho, K. B. Ruan, L. Wang and A. Moewes, *Phys. Rev. B*, **86** (2012) 115212.
23. K. Yang, Y. Dai, and B. Huang, *Appl. Phys. Lett.*, **100** (2012) 062409.
24. E. Albanese, M. Leccese, C. D. Valentin and G. Pacchioni, *Scientific Reports*, **6** (2016) 31435.
25. D. J. Singh, M. Gupta and R. Gupta, *J. Appl. Phys.*, **91** (2002) 7370.
26. D. J. Sing and I.I. Mazin, *Phys. Rev. B* **63** (2001) 165101.
27. A. E. Taylor, R. Morrow, D. J. Sing, S. Calder, M. D. Lumsden, P. M. Woodward and A. D. Christianson, *Phys. Rev. B* **91** (2015) 100406(R).
28. J. K. Furdyna, *J. Appl. Phys.*, **64** (1988) R29.
29. P. Dutta, M. S. Seehra, Y. Zhang and I. Wender, *J. Appl. Phys.*, **103** (2008) 07D104.

30. A. Sundaresan and C. N. R. Rao, *Nano Today*, **4** (2009) 96-106.
31. W. Prellier, A. Fouchet and B. Mercey, *J. phys.: Condens Matter*, **15** (2003) R1583-R1601.
32. N. H. Hong, J. Sakai and F. Gervais, *J. Magnetism and Magnetic Materials*, **316** (2007) 214-217.
33. X. Jiang, R. Wang, R. M. Shelby, R. M. Macfarlane, S. R. Bank, J. s. Harris and S. S. P. Parkin, *Phys. Rev. Lett.*, **94** (2005) 056601.
34. Z. Mao, Z. He, D. Chen, W. Y. Cheung, and S. P. Wong, *Solid State Commun.*, **142** (2007) 329-332.
35. L. J. Shi, *Phys. Lett. A*, **374** (2010) 1292-1296.
36. P. Wu, G. Cao, F. Tang, and M. Huang, *Compu. Mat. Sci.*, **86** (2014) 180-185.
37. S. Nagar, O. D. Jayakumar, L. Belova and K. V. Rao, *Mat. Exp.*, **2** (2012) 233.
38. D. D. Wang, Z. Q. Chen, C. Y. Li, X. F. Li, C. Y. Cao and Z. Tang, *Physica B*, **407** (2012) 2665-2669.
39. L. Balcells, J. I. Beltran, C. M. Boubeta, Z. Konstantinovic, J. Arbiol and B. Martinez, *Appl. Phys. Lett.*, **97** (2010) 252503.
40. M. Kapilashrami, J. Xu, K. V. Rao, L. Belova, E. Carlegrim, and M. Fahlman, *J. Phys.: Condens Matter*, **22** (2010) 345004.
41. B. Gu, N. Bulut, T. Ziman, and S. Maekawa, *Phys. Rev. B*, **79** (2009) 024407.
42. M. Pesci, F. Gallino, C. Di Valentin, and G. Pacchioni, *J. Phys. Chem. C* **114** (2010) 1350-1356.
43. V. Sharma, G. Pilania and J. E. Lowther, *AIP Advances*, **1** (2011) 032129.
44. F. Kuang, S. Kang, Y. Xu, Z. Xiong, J. Liao, H. Yu, X. Zhang, T. Sun and J. Cao, *J. All. Com.*, **712** (2007) 526-534.

45. D. Mishra, B. P. Mandal, R. Mukherjee, R. Naik, G. Lawes, and B. Nadgorny, *J. Appl. Phys.*, **102** (2013) 182404.
46. C. M. Araujo, M. Kapilashrami, X. Jun, O. D. Jayakumar, S. Nagar, Y. Wu, C. Arhammar, B. Johansson, L. Belova, R. Ahuja, G. A. Gehring and K. V. Rao, *Appl. Phys. Lett.* **96** (2010) 232505.
47. M. Seike, K. Sato and H. K. Yoshida, *J. J. Appl. Phys.*, **50** (2011) 090204.
48. F. Gao, Jifan Hu, C. Yang, Y. Zheng, H. Qin, L. Sun, X. Kong and M. Jiang, *Solid State Commun.* **149** (2009) 855-858.
49. F. Kuang, S. Kaung and Q. Chen, *RSC Advances*, **4** (2014) 51366.
50. J. I. Beltrán, C. Monty, L. Balcells, and C. Martínez-boubeta, *Solid State Commun.* **149** (2009) 1654-1657.
51. F. Wang, Z. Pang, L. Lin, S. Fang, Y. Dai, and S. Han, *Phys. Rev. B* **80** (2009) 144424.
52. J. Li, Y. Jiang, Y. Li, D. Yang, Y. Xu, and M. Yan, *Appl. Phys. Lett.* **102** (2013) 072406.
53. C. Martínez-boubeta, J. I. Beltran, L. Balcells, Z. Konstaninovic, D. Schmitz, J. Arbiol, S. Estrade, J. Cornil and B. Martinez, *Phys. Rev. B* **82** (2010) 024405.
54. S. G. Yang, T. Li, B. X. Gu, Y. W. Du, H. Y. Sung, S. T. Hung, C. Y. Wong and A. B. Pakhomov, *Appl. Phys. Lett.*, **83** (2003) 3746.
55. A. Punnoose, H. Magnone, and M. S. Seehra, *Phys. Rev. B*, **64** (2001) 174420.
56. A. Filippetti and V. Fiorentini, *Phys. Rev. B*, **74** (2006) 220401 (R).
57. K. H. Gao, Z. Q. Li, T. Du, and E. Y. Jiang, *Phys. Rev. B*, **75** (2007) 174444.

58. F. Zhao, H. M. Qiu, L. Q. Pan, H. Zhu, Y. P. Zhang, Z. G. Guo, J. H. Yin, X. D. Zhao and J. Q. Xiao, *J. Phys.: Condense Matter* **20** (2008) 425208.
59. R. N. Mariammal, K. Ramachandran, G. Kalaiselvan, and S. Arumugam, *Appl. Surf. Sci.*, **270** (2013) 545–552.
60. S. Manna and S. K. De, *J. Magnetism and Magnetic Mat.* **322** (2010) 2749-2753.
61. H. Qin, Z. Zhang, X. Liu, Y. Zhang, and J. Hu, *J. Magnetism and Magnetic Mat.* **322** (2010) 1994-1998.
62. M. Vila, C. Diaz-Guerra and J. Piqueras, *J. Phys. D: Appl. Phys.* **43** (2010) 135403.
63. J. G. Zhao, S. J. Liu, S. H. Yang, and S. G. Yang, *Appl. Surf. Sci.*, **257** (2011) 6978-9681.
64. N. Rajkumar, V. M. Susila and K. Ramachandran, *J. of Expt. Nanoscience*, **6** (2011) 389-398.
65. C. W. Zhang, P. J Wang and Y Su, *Phys. Lett. A*, **374** (2010) 1889-1892.
66. S. B. Ogale, R. J. Choudhary, J. P. Buban, S. E. Lofland, S. R. Shinde, S. N. Kale, V. N. Kulkarni, J. Higgins, C. Lanci, J. R. Simpson, N. D. Browning, S. D. Sarma, H. D. Drew, R. L. Greene and T. Venkatesan, *Phys. Rev. Lett.*, **91** (2003) 077205.
67. A. Espinosa, N. Menéndez, C. Prieto, and A. De Andrés, *Phys. Rev. B*, **81** (2010) 064419.
68. J. Zhang, Q. Yun and Q. Wang, *Mod. Appl. Sci.* **11** (2010) 124-130.

69. Y. Matsumoto, M. Murakami, and T. Shono, T. Hasegawa, T. Fukumura, M. Kawasaki, P. Ahmet, T. Chikyow, S. Koshihara, H. Koinuma, *Science*, **291** (2001) 854.
70. S. A. Chambers, S. Thevut5hasan, R. F. C. Farrow, R. F. Marks, J. U. Thiele, L. Folks, M. G. Samant, A. J. K. Ruzycki, D. L. Ederer, and U. Diebold, *Appl. Phys. Lett.* **79** (2001) 3467.
71. J. D. Bryan, S. M. Heald, S. A. Chambers and D. R. Gamelin, *J. Am. Chem. Soc.* **126** (2004) 11640-11647.
72. S. Duhalde, M. F. Vignolo, F. Golmar, C. Chilotte, C. E. R. Torres, L. A. Errico, A. F. Cabrere, M. Renteria, F. H. Sanchez and M. Weissmann, *Phys. Rev. B*, **72** (2005) 161313(R).
73. N. H. Hong, J. Sakai and A. Hassini, *Appl. Phys. Lett.* **84** (2004) 2602.
74. N. H. Hong, J. Sakai, W. Prellier, A. Hassini, A. Ruyter and F. Gervais, *Phys. Rev. B* **70** (2004) 195204.
75. J. M. D. Coey, *Solid State Sciences* **7** (2005) 660-667.
76. N. H. Hong, J. Sakai, N. T. Huong, N. Poirot, A. Ruyter, *Phys. Rev. B* **72** (2005) 045336.
77. A. Sundaresan, R. Bhargavi, N. Rangarajan, U. Siddesh and C. N. R. Rao, *Phys. Rev. B* **74** (2006) 16106(R).
78. D. Sanyal, M. Chakrabarti, T. K. Roy and A. Chakrabarti, *Phys. Lett. A* **371** (2007) 482-485.
79. V. M. Zainullina, V. P. Zhukov, M. A. Korotin and E. V. Polyakov, *Phys. Solid State* **53** (2011) 1353-1361; X. G. Xu, H. L. Yang, Y. Wu, D. L. Zhang,

- S. Z. Wu, J. Miao, X. B. Qin, X. Z. Cao, B. Y. Wang, *Appl. Phys. Lett.* **97** (2010) 232502.
80. P. Nath, A. Chakraborty and D. Sanyal, *RSC Adv.* **4** (2014) 45598; H. Luitel and D. Sanyal, *Computational Condensed Matter*, **19** (2019) e00376.
81. H. Luitel and D. Sanyal, *Int. J. Mod. Phys. B*, **31** (2017) 1750227; H. Luitel, P. Chettri, A. Tiwari and D. Sanyal, *Mat. Res. Bulletin*, **110** (2019) 13-17.
82. H. Luitel, S Roy, D Sanyal, *Computational Condensed Matter*, **14** (2017) 36-39.
83. P. Biswas, P. Nath, D. Sanyal and P. Banerji, *Current Appl. Phys.*, **15** (2015) 1256.
84. H. Pan, J. B. Yi, L. Shen, R.Q. Wu, J. H. Yang, J. P. Feng, J. Ding, L. H. Van and J. H. Yin, *Phys. Rev. Lett.*, **99** (2007) 127201.
85. X. J. Ye, W. Zhong, M. H. Xu, X. S. Qi, C. T. Au and Y.W. Du, *Phys. Lett. A*, **373** (2009) 3684.
86. K. Yang, Y. Dai, B. Huang and M.H. Whangbo, *Appl. Phys. Lett.* **93** (2008) 132507.
87. C. W. Zhang, P. J. Wang and Y. Su, *Phys. Lett. A*, **374** (2010) 1889-1892.
88. D. Sanyal, M. Chakrabarti, P. Nath, A. Sarkar, D. Bhowmick and A. Chakrabarti, *J. Phys. D: Appl. Phys* **47** (2014) 025001.
89. J. Nisar, X. Peng and R. Ahuja, *Phys. Rev. B* **81** (2010) 012402.
90. H. Luitel, A. Sarkar, M. Chakrabarti, S. Chattopadhyay, K. Asokan and D. Sanyal, *Nuclear Inst. & Method. B* **379** (2016) 215.
91. N. Kumar, D. Sanyal and A. Sundaresan, *Chem. Phys. Lett.*, **477** (2009) 360.
92. N. H. Hong, N. Poirot and J. Sakai, *Phys. Rev. B* **77** (2008) 033205.

93. A. Sarkar, D. Sanyal, P. Nath, M. Chakrabarti, S. Pal, S. Chattopadhyay, D. Jana and K. Asokan, *RSC Adv.* **5** (2015) 1148-1152.
94. J. Bang, Y. S. Kim, C. H. Park, S. Gao and S. B. Zhang, *Appl. Phys. Lett.* **104** (2014) 252101.
95. Z. Wang, S. C. Su, M. Younas, F. C. C. Ling, W. Anwand and A. Wagner, *RSC Adv.* **5** (2015) 12530-12535.
96. S. Dutta, S. Chattopadhyay, A. Sarkar, M. Chakrabarti, D. Sanyal and D. Jana, *Prog. Mater. Sci.* **54** (2009) 89-136.
97. S. K. Sharma, P. K. Pujari, K. Sudarshan, D. Dutta, M. Mahapatra, S. V. Godbole, O. D. Jayakumar and A. K. Tyagi, *Solid State Commun.* **149** (2009) 550.
98. K. J. Chen, F. Y. Hung, S. J. Chang, S. P. Chang, Y. C. Mai, Z. S. Hu, *J. Alloys Comp.* **509** (2011) 3667-3671.
99. C. Drouilly, J. M. Krafft, F. Averseng, S. Casale, D. B. Bachi, C. Chizallet, V. Lecocq, H. Vezin, H. L. Pernot and G. Costentin, *J. Phys. Chem. C* **116** (2012) 21297-21307.
100. A. Valour, F. Chevire, F. Tessier, F. Grasset, B. Dierre, T. Jiang, E. Faulques, L. Cario and S. Jobic, *Solid State Science* **54** (2016) 30-36.
101. T. Chen, S. Y. Liu, Q. Xie, C. Detavernier, R. L. V. Meirhaeghe and X. P. Qu, *J. Mater. Sci.: Mater. Electron* **21** (2010) 88-95.
102. T. T. Ali, K. Narasimharao, I. P. Parkin, C. J. Carmalt, S. Sathasivam, S. N. Basahel, S. M. Bawaked and S. A. A. Thabaiti, *New J. Chem.* **39** (2015) 321-332.
103. J. Gupta, K. C. Barick and D. Bahadur, *J. Alloys Comp.* **509** (2011) 6725-6730.

104. A. Janotti and C. G. Van de Walle, *Phys. Rev. B* **76** (2007) 165202.
105. D. H. Kim, G. W. Lee and Y. C. Kim, *Solid State Commun.* **152** (2012) 1711.
106. L. Liu, J. Xu, D. Wang, M. Jiang, S. Wang, B. Li, Z. Zhang, D. Zhao, C. X. Shan, B. Yao and D. Z. Shen, *Phys. Rev. Lett.* **108** (2012) 215501.
107. M. S. Holston, E. M. Golden, B. E. Kananen, J. W. McClory, N. C. Giles and L. E. Halliburton, *J. Appl. Phys.* **119** (2016) 145701.
108. P. Hohenberg and W. Kohn, *Phys. Rev. B*, **136** (1964) 864.
109. W. Kohn and L. J. Sham, *Phys. Rev. B*, **140** (1965) 1133.
110. A. Chakrabarti, A. Bandyopadhyay, V. Naik, S. Dechoudhury, M. mondal, P.Y. Nabhiraj, *Nuclear Inst. & Method.* 317 (2013) 253-256.
111. A. Chakrabarti, *Paramana* 59 (2002) 923-932.
112. J. Pascual, J. Camassel and H. Mathieu, *Phys. Rev. B* **18** (1978) 5606-5614.
113. B. Choudhury, M. Dey, and A. Choudhury, *International Nano Lett.* **3** (2013) 25.
114. J. Navas, A. S. Coronilla, T. Aguilar, C.N. Hernandez, D. M. de los Santos, J.S. Marquez, D. Zorrilla, C. F. Lorenzo, R. Alcantara and J. M. Calleja, *Phys. Chem. Chem. Phys.* **16** (2014) 3835-3845.
115. M. K. Nowotny, L. R. Sheppard, T. Bak and J. Nowotny, *J. Phys. Chem. C* **112** (2008) 5275-5300.
116. H. Peng, J. Li, S. S. Li and J. B. Xia, *Phys Rev B* **79** (2009) 092411.
117. K. Yang, Y. Dai, B. Huang and M. H. Whangbo, *Chem Phys Lett.*, **481** (2009) 99.
118. Y. Bai and Q. Chen, *Solide State Commun.* **147** (2008) 169.

119. M. K. Nowotny, L. R. Sheppard, T. Bak and J. Nowotny, *J. Phys. Chem. C* **112** (2008) 5275-5300.
120. G. Kresse and J. Hafner, *Phys. Rev. B*, **47** (1993) 558.
121. G. Kresse and J. Hafner, *Phys. Rev. B* **49** (1994) 14251.
122. G. Kresse and J. Furthmüller, *Comput. Mater. Sci.* **6** (1996) 15.
123. G. Kresse, and J. Furthmüller, *Phys. Rev. B* **54** (1996) 11169.
124. J. P. Perdew, K. Burke and M. Ernzerhof, *Phys. Rev. Lett.* **77** (1996) 3865-3868.
125. H. J. Monkhorst and J. D. Pack, *Phys. Rev. B*, **13** (1976) 5188.
126. J. Ziegler, J. Biersack and U. Littmark, The Stopping and range of ions in matter; Pergamon, New York (1985). SRIM 2008 code, www.srim.org.
127. N. Seriani, C. Pinilla and Y. Crespo, *J. Phys. Chem. C* **119** (2015) 6696-6702.
128. P. Kirkegaard, N. J. Pedersen and M. Eldrup, *Report of Riso National Lab* (Riso-M-2740) (1989).
129. S. Tanigawa, K. Hinode, N. Owada, M. Doyama, E. Iguchi, A. Inoue, in: K.K. Hasiguti and K. Fujiwara (Eds.), Proceedings of 5th International Conference on Positron Annihilation, The Japan Institute of Metals, Sendai (1979) p. 475.
130. L. Li, J. Yan, T. Wang, Z. Zhao, J. Zhang, J. Gong and N. Guan, *Nature* **6** (2015) 5881.
131. T. H. Lang, C. V. Tao, K. T. Dung and L. H. Chien, *World J. Nucl. Sci. Tech.* **4** (2014) 33.
132. H. Luitel, M. Chakrabarti, A. Sarkar, S. Dechoudhury, D. Bhowmick, V. Naik and D. Sanyal, *Mat. Res. Exp.* **5** (2018) 026104.
133. A. V. Krasheninnikov, K. Nordlund, *J. Appl. Phys.* **107** (2010) 071301.

134. Y. M. Lee, W. S. Yun, S. C. Hong, M. C. Jung, *J. Appl. Phys.* **109** (2011) 124316.
135. www.webelements.com/periodicity/electronegativity_pauling/, extracted on 21/11/2017.
136. L. Shen, R. Q. Wu, H. Pan, G. W. Peng, M. Yang, Z. D. Sha, Y. P. Feng, *Phys. Rev. B* **78** (2008) 073306.
137. J. B. Yi, L. Shen, H. Pan, L. H. Van, S. Thongmee, J. F. Hu, Y. W. Ma, J. Ding and Y. P. Feng, *J. Appl. Phys.* **105** (2009) 07C513.
138. A. Sarkar, M. Chakrabarti, D. Sanyal, D. Bhowmick, S. DeChoudhury, A. Chakrabarti, T. Rakshit and S. K. Ray, *J. Phys.: Condens. Matter* **24** (2012) 325503; H. Luitel, D. Sanyal, N. Gogurla, A. Sarkar, *J. Mat. Sci.*, **52** (2017) 7615-7623; *Mat. Res. Exp.* **4** (2017) 035909.
139. D. C. Iza, D. M. Rojas, Q. Jia, B. Swartzentruber and J. L. M. Driscoll, *Nanoscale Res. Lett.* **7** (2012) 655.
140. T. Koida, S. F. Chichibu, A. Uedono, A. Tsukazaki, M. Kawasaki, T. Sota, Y. Segawa and H. Koinuma, *Appl. Phys. Lett.* **82** (2003) 532-534.
141. S. Dutta, M. Chakrabarti, S. Chattopadhyay, D. Jana, D. Sanyal and A. Sarkar, *J. of Appl. Phys.* **98** (2005) 053513.
142. U. Myler and P. J. Simpson, *Phys. Rev. B* **56** (1997) 14303-14309.
143. www.webelements.com
144. I. Makkonen, E. Korhonen, V. Prozheeva and F. Tuomisto, *J. Phys.: Condens. Matter* **28** (2016) 224002-7.
145. J. J. Richardson, G. K. L. Goh, H. Q. Le, L. L. Liew, F. F. Lange, S. P. DenBaars, *Cryst. Growth Des.* **11** (2011) 3558-3563.

146. Y. Zeng, K. Schouteden, M. N. Amini, S. C. Ruan, Y. Lu, Z. Z. Ye, B. Partoens, D. Lamoen and C. V. Haesendonck, *ACS Appl. Mater. Interfaces* **7** (2015) 10617.
147. T. Bora, K. K. Lakshman, S. Sarkar, A. Makhal, S. Sardar, S. K. Pal and J. Dutta, *J. Nanotechnol.* **4** (2013) 714-725.
148. S. Chattopadhyay, S. Dutta, D. Jana, S. Chattopadhyay, A. Sarkar, P. Kumar, D. Kanjilal, D. K. Mishra and S. K. Ray, *J. Appl. Phys.* **107** (2010) 113516.
149. E. G. Barbagiovanni, R. Reitano, G. Franzò, V. Strano, A. Terrasi and S. Mirabella, *Nanoscale* **8** (2016) 995-1006.
150. K. Bandopadhyay and J. Mitra, *RSC Adv.* **5** (2015) 23540-235.
151. F. Fabbri, M. Villani, A. Catellani, A. Calzolari, G. Cicero, D. Calestani, A. Zappettini, B. Dierre, T. Sekiguchi and G. Salviati, *Scientific Reports* **4** (2014) 5158.
152. C. Ton-That, L. Weston and M. R. Phillips, *Phys. Rev. B* **86** (2012) 115205.
153. R. Vidya, P. Ravindran, E. Fjellvåg, B. G. Svensson, E. Monakhov, M. Ganchenkova and R. M. Nieminen, *Phys. Rev. B* **83** (2011) 045206.
154. C. H. Ahn, Y. Y. Kim, D. C. Kim, S. K. Mohanta and H. K. Cho, *J. Appl. Phys.* **105** (2009) 013502.
155. F. Stavale, N. Nilius and H. J. Freund, *J. Phys. Chem. Lett.* **4** (2013) 3972-3976.
156. J. Ji, L. A. Boatner and F. A. Selim, *Appl. Phys. Lett.* **105** (2014) 041102.
157. S. Pal, A. Sarkar, P. Kumar, D. Kanjilal, T. Rakshit, S. K. Ray and D. Jana, *J. Lumin.* **169** (2016) 326-333.

158. M. Schirra, R. Schneider, A. Reiser, G. M. Prinz, M. Feneberg, J. Biskupek, U. Kaiser, C. E. Krill, K. Thonke and R. Sauer, *Phys. Rev. B* **77** (2008) 125215.
159. Y. Dong, F. Tuomisto, B. G. Svensson, A. Y. Kuznetsov and L. J. Brillson, *Phys. Rev. B* **81** (2010) 081201 (R).
160. Q. Wang, Y. Yan, Y. Zeng, Y. Lu, L. Chen and Y. Jiang, *Sci. Rep.* **6** (2016) 27341.
161. D. Tainoff, B. Masenelli, P. Mélinon, A. Belsky, G. Ledoux, D. Amans, C. Dujardin, N. Fedorov and P. Martin, *Phys. Rev. B* **81** (2010) 115304.
162. M. Schirra, R. Schneider, A. Reiser, G. M. Prinz, M. Feneberg, J. Biskupek, U. Kaiser, C. E. Krill, K. Thonke and R. Sauer, *Phys. Rev. B* **77** (2008) 125215.
163. S. Pal, T. Rakshit, S. S. Singha, K. Asokan, S. Dutta, D. Jana and A. Sarkar, *J. Alloys Compd.* **703** (2017) 26-33.
164. M. Batzill, U. Diebold, *Progress in Surface Science* **79** (2005) 47–154.
165. J. Hays, A. Punnoose, R. Baldner, M.H. Engelhard, J. Peloquin and K.M. Reddy, *Phys. Rev. B* **72** (2005) 075203.
166. E. Albanese, C. D. Valentin, G. Pacchioni, F. Sauvage, S. Livraghi and E. Giamello, *J. Phys. Chem. C* **119** (2015) 26895-26903.
167. E. Chang and E.K. Graham, *J. Geophys. Res.* **80** (1975) 2595-2599.
168. S. S. Pan, S. Wang, Y. X. Zhang, Y. Y. Luo, F. Y. Kong, S. C. Xu, J. M. Xu and G. H. Li, *Appl. Phys. A* **109** (2012) 267-271.
169. S. S. Pan, G. H. Li, L. B. Wang, Y. D. Shen, Y. Wang, T. Mei and H. Hu, *Appl. Phys. Lett.* **95** (2009) 222112.